Evaluation of the Planar Germanium SmartPET system for use in Positron Emission Imaging.

Thesis submitted in accordance with the requirements of
the University of Liverpool for the degree of Doctor in Philosophy

by

Andrew Raymond Mather

Oliver Lodge Laboratory

25 December 2006

Abstract

The work presented in this thesis details the positron imaging performance of the SmartPET planar germanium system. Sets of two dimensional slice images are reconstructed from the first PET data sets collected with the system. Results from both the analytical image reconstruction algorithm, filtered backprojection (FBP) and statistical maximum likelihood algorithm (ML-EM) are presented. Pulse Shape Analysis methods were developed to improve detector spatial resolution based on consideration of the nearest neighbour image charge areas.

The experiments involved the imaging of three ^{22}Na point sources at various locations within the system's field of view. Data was collected at 36 equally spaced projections for 7.5 hours per projection. The FWHM of the point sources was found to be $\sim$6mm (FBP) and approaching 1mm (ML-EM) from the detector segmentation alone. PSA was employed to improve the detector spatial resolution from 5mm^2 to 1mm^2 and produced a subsequent improvement in the FWHM for FBP images to $\sim$3mm. Attempts to apply the same methodology with the iterative algorithms led to problems due to the system matrix implementation with further refinement still required in this area. Utilising the excellent energy resolution of germanium by means of photopeak gating produced impressive sinograms with superb scatter rejection. However the resultant images showed little change and the statistical limitations after photopeak gating became apparent.

The experimental measurements undertaken provide conclusive evidence of the feasibility of planar germanium detectors for use within positron emission imaging systems. It has been shown simple pulse shape analysis techniques can by employed to improve spatial resolution and hence imaging performance.

It doesn't matter how beautiful your theory is, it doesn't matter how smart you are.
If it doesn't agree with experiment, it's wrong.

Richard P. Feynman

He was a wise man who invented beer.

Plato

Acknowledgements

Let me take this opportunity to acknowledge the roll played by a number of people whom have helped and supported me over the course of this study, both academically and personally. I would like to start out by thanking Prof. Paul Nolan, Head of Department, for providing me with the opportunity to study a Ph.D at Liverpool University. I would also like to thank my supervisor Dr Andy Boston for all of his support and guidance over the past four years.

A massive thank-you to my girlfriend Suzy who has provided an immeasurable amount of love, support and patience throughout my study. I apologise for all the physics related conversations you have had to tolerate over the years, those darn protons and neutrons must drive you to despair!

Moving back to the work related aspects (sorry Suzy!) I would like to thank all my fellow Ph.D students here at Liverpool, especially the detector group past and present; Gerard, Jenny, Sebastian, Ren, Matt, Laura, David, Alex and Majid. Thank you to Helen Boston for the support in setting up the experimental equipment including the now infamous broom handle^{TM} (patent pending!)

Many thanks to all the support staff at Liverpool, including Terry Burns, John Cresswell, Janet Sampson, Dave Seddon, Mark Norman and Jim Thornhill without whom this work would ultimately not have been possible. Thank-you to the rest of the staff, post docs and students whom I have sadly failed to mention by name.

Of course I owe a great deal of gratitude to my family, my mum and dad who really did make this all possible, my nan, granddad and brothers (deep breath) Lee, Carl, Michael, Jamie, Sam, Ben and finally the newest addition and only sister, little Amy.

Finally thanks to Ged and Aweys for all our lunch time conversations, and ale induced friday night blabbering on pretty much every subject you could imagine and some you probably never would.

Contents

List of Figures

List of Tables

Chapter 1

Introduction

1.1 Nuclear medicine

Nuclear medicine is the branch of medicine which utilises radioactive sources in diagnosis and therapy of patients. The medical imaging diagnostic techniques Positron Emission Tomography (PET) and Single Particle Emission Computed Tomography (SPECT) are two imaging modalities able to probe the physiological functions of a system. This information complements anatomical imaging modalities such as x-ray Computed Tomography (CT) and Magnetic Resonance Imaging (MRI). All of the techniques outlined provide a means of imaging patients non-invasively. The results are used to diagnose potential conditions including many forms of cancer and neurological problems. The scans can also provide means of examining the effectiveness of a treatment plan already in place for a known condition.

PET and SPECT both involve the patient being administered a radiopharmaceutical or tracer; a radioactive element chemically bound to a molecule known to have a specific behaviour within the body. The decay of the radioactive element leads to the creation of gamma-rays with characteristic energies. Detecting these gamma-rays makes it possible to produce images of the tracer distribution within the patient. The specific element and molecule used depends both on the imaging modality and the expected disease under study. For example in PET imaging the molecule ^{18}F-FDG

(fluorodeoxyglucose) is used for the assessment of glucose metabolism in the heart and the brain. It is also used for imaging tumours in oncology.

1.1.1 Positron Emission Tomography

This thesis discusses a potential instrumentation improvement for the PET imaging modality. PET imaging involves the administration of a positron decaying tracer. The emitted positron annihilates with a near-by electron forming two back-to-back 511 keV photons. The detection of both of these photons provides information about the location from which the decay occurred. The collected data from the detectors is processed by image reconstruction algorithms to produce 2D or 3D tracer distribution maps.

A significant problem for both PET and SPECT imaging is the possibility that the gamma-rays scatter and hence change direction before reaching the detector system. If included in the imaging analysis these events cause degradation of the final image and can therefore potentially effect the ability of the clinician to make accurate diagnosis.

1.1.2 Small animal imaging

Biological science has become increasingly interested in transgenic mouse models of human diseases during the last decade. The development of PET scanners capable of imaging small animals such as mice is currently an active research area. The small size of the animal imposes strict requirements on the scanner spatial resolution, approaching the theoretical limit due to the positron range. Two current leading designs for small animal imaging are the MicroPET II device [Che03] and the Oxford Positron Systems Quad-HIDAC [Jea99].

1.2 Segmented germanium detectors

Detectors fabricated from the semi-conducting element germanium are excellent for the detection of gamma-rays in the energy range of interest for nuclear medicine. Ger-

manium detectors have long been the workhorse of the nuclear physics community for gamma-ray spectroscopy due to their unrevealed energy resolution. They provide the backbone for numerous large international experiments where many tens or hundreds of detectors are combined to form advanced arrays [Lee90] [Sim97].

More recently germanium detectors can now be manufactured with electrical segmentation of a single crystal. This development provides some level of positional information about the gamma-ray interaction alongside the energy resolution mentioned. The availability of spatial data opens up the possibility of germanium detectors being integrated into nuclear imaging systems. Furthermore an analysis technique known as Pulse Shape Analysis (PSA) [Des02] can be applied to germanium detectors to improve the spatial resolution. With PSA the position of interaction of the gamma-rays within the detector is improved beyond that afforded simply by the segmentation of the detector crystal.

1.3 The SmartPET project

The aim of the SmartPET project is to develop a prototype small animal imaging system based on germanium detector technology. Two single crystal electrically segmented planar germanium detectors are fixed in a rotating gantry and attached to a digital electronics acquisition system. SmartPET is a dual-head configuration scanner and therefore the rotational motion is required to allow complete field-of-view coverage. SmartPET is predominantly designed to be used as a small animal PET scanner but many other forms of conventional and non-conventional imaging are possible. Some of the potential improvements SmartPET provides include:

- The energy resolution of germanium allows much greater discrimination of scatter events than any conventional scintillator based solution for PET and SPECT
- Multiple tracer SPECT, where more than one tracer is administered for a single scan is possible with such a system and would provide new possibilities for clinicians.

- The energy resolution in conjunction with PSA allows the system to individually track gamma-rays as they scatter through the detector itself, a technique known as gamma-ray tracking [Lee99]. This information opens up a plethora of new imaging options such as Compton imaging (collimator-less SPECT) and Compton assisted PET where the scattering profile is used to validate PET events.

- Depth of interaction information from PSA methods reduces considerably the potential parallax effects inherent in many conventional PET systems. Most existing systems have little or no sensitively to depth of interaction.

- With the use of PSA the SmartPET detector's spatial resolution is of the same order as conventional small animal systems. Improved spatial resolution can be achieved with advancements in PSA algorithms rather than needing increased numbers of smaller detector elements and electronics channels.

1.3.1 Aims of this work

The work presented in this thesis looks at the analysis of the first coincidence data sets collected with the two SmartPET detectors for the purpose of PET imaging. The aims of this work are:

- The development of analytical and statistical PET imaging algorithms for the SmartPET project. Using 'ideal' simulated data confirm the algorithms performance to provide confidence in their later application to experimental data.

- Develop software procedures for managing the experimentally collected data and converting it to a format convenient for use by the imaging algorithms. Provide feedback on experimental procedures and data processing improvements that could be applied to later experimental work.

- Apply the imaging algorithms to the first coincidence data set. Produce reconstructed images of ^{22}Na point-sources and contrast the imaging performance for

different reconstruction algorithms and parameters.

- Using simple PSA techniques improve the detector spatial resolution beyond that of the segmentation size alone. Reproduce the reconstructed images for comparison with the results obtained without PSA.

Chapter 2

The physics of Positron Emission Tomography

2.1 Introduction

The physics principles governing positron emission and detection for purposes such as functional medical imaging can be divided into two sets of processes. Firstly the emission of a positron (e^+) from a β^+ decaying nucleus and the subsequent annihilation with a nearby electron (e^-), creating two co-linear 511 keV gamma-ray photons. Secondly the detection of these photons via their interaction in a semiconductor or scintillator based detector system. The photons provide an indirect means of measuring that an annihilation event has occurred along the line joining the two interaction sites.

2.2 Positron emission and annihilation

The existence of a subatomic particle with the same mass but opposite charge to that of the electron was first postulated by Paul Dirac in 1928 [Dir58]. Four years later Carl Anderson experimentally confirmed the existence of such a particle, the antimatter equivalent of the electron which became known as the positron.

2.2.1 β^+ decay

Beta decay is a radioactive decay mechanism that unstable atoms can use to move towards a more stable configuration. In the process of beta decay either an electron or a positron is emitted from the nucleus and therefore there are two types of beta decay, β^- (electron) and β^+ (positron).

Unstable nuclides with a large proton imbalance may decay to a more stable daughter nuclide via β^+ or positron decay. In β^+ decay one of the protons within the nucleus transforms into a neutron and two leptons; the positron and neutrino. This process, which proceeds by the weak nuclear force can be written as:

$$p \rightarrow n + e^+ + v_e \tag{2.1}$$

Because the neutron mass is greater than that of the proton additional energy is required for the decay to take place. β^+ decay can only occur inside nuclei when the absolute value of the binding energy of the daughter nucleus is higher than that of the parent. The equation for the β^+ decay of ^{22}Na is given by:

$$^{22}_{11}Na \rightarrow ^{22}_{10}Ne + e^+ + v_e \tag{2.2}$$

The available excess binding energy is shared between the recoiling daughter nucleus and the two leptons. The emitted β particle therefore carries off some of the available energy ranging from almost zero up to a specific maximum value, which is dependent on the parent nucleus involved in the decay. The maximum energy of the positron plays an important role in PET imaging because it relates to the maximum range of the positron before annihilation, a fundamental limit for imaging. The positron emitting ^{22}Na source is used throughout this study, the decay scheme for this nuclide is shown in figure 2.1.

2.2.2 e^+ e^- annihilation

As positrons pass through matter they interact and lose kinetic energy via ionisation or elastic scattering predominantly with atomic electrons. These interactions will

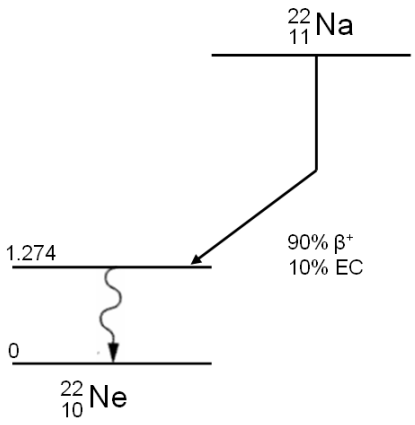

Figure 2.1: Decay scheme diagram for the ^{22}Na nuclide. 90% of decays yield the positron required to facilitate imaging.

cause deflections in the path followed by the positron. Ultimately the positron will collide with an electron with both particles being in thermal equilibrium with their environment. The electron and positron may combine to form a quasi-stable compound system called a positronium. The positronium has a lifetime of no more than 150ns and whose existence is terminated when the electron and positron annihilate. Alternatively the electron and positron may annihilate directly without first forming the quasi-stable state.

Conservation of energy and momentum dictates that two gamma-ray photons of energy 511 keV (equal to the rest mass of the electron and positron) are emitted in opposite directions if the annihilation takes place at rest. In reality the particles will have some residual momentum leading to a small ranges of photon energies and therefore deviation from collinear emission although typically these effects are smaller than 0.5^o [DeB50]. Figure 2.2 shows a schematic diagram of the positrons life from emission to annihilation.

Three or more photon decay channels exist but the probabilities are small in comparison. In the case of a free positron the three photon probability is 1/373 that of the two photon decay mode [Ore49]. In materials such as water the triple photon yield is typically of the order 0.5%. The detector geometry used in this work is not

Nuclide	E_{max} (MeV)	Half-life (mins)	Range in Water (mm)	
			Max	Mean
^{11}C	0.959	20.4	4.1	1.1
^{13}N	1.197	9.96	5.1	1.5
^{15}O	1.738	2.03	7.3	2.5
^{18}F	0.633	109.8	2.4	0.6
^{22}Na	0.546	1.37×10^6	2.0	0.5
^{68}Ga	0.783	68.3	8.2	2.9

Table 2.1: Properties of several commonly used nuclides in PET imaging studies. E_{max} refers to the maximum energy that can be carried away by the positron.

suited to the measurement of the triple photon decay although attempts to image from three photon decays have had some success [Kac01].

The complex nature of the positron's path before annihilation makes prediction of a mean range for positrons in a material as a function of initial kinetic energy (which is related to the nucleus the decay originated) very complex. Hence values for the mean range are generally based on empirical measurements. Table 2.1 outlines the range of positrons in water for a number of different nuclides used for medical imaging applications.

2.3 Interaction of photons with matter

Photons interact with matter through a number of different mechanisms, depositing part or all of their energy after interactions with atomic electrons. In the case of PET systems where the energy range of importance stretches from 10 keV to beyond 511 keV only two processes, the photoelectric effect and Compton scattering need to be considered [Figure 2.3]. Pair production (the creation of a electron-positron pair) occurs only at energies above 1 MeV and so can be ignored. Other scattering processes such as Rayleigh and Thomson scattering can be neglected as they are only

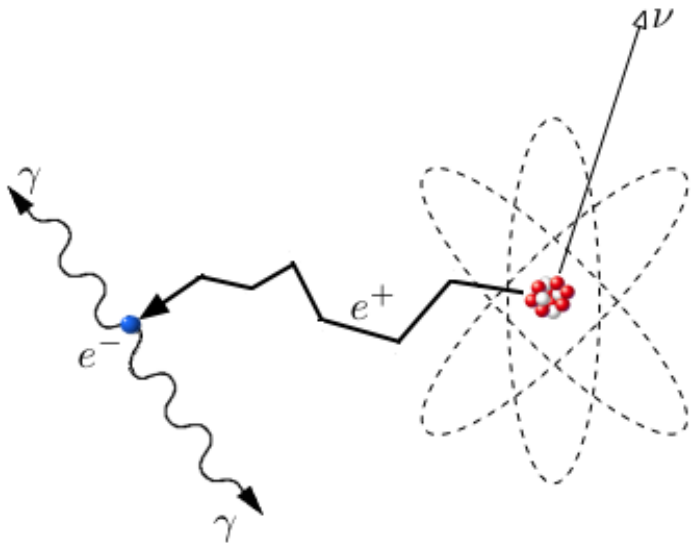

Figure 2.2: Depiction of the positron's lifetime from the production in a β^+ decay of a nucleus to the annihilation with an electron, leading to the signature back-to-back 511 keV photons.

important at much lower energies than considered in this work.

2.3.1 Photoelectric effect

The photoelectric effect is the dominant interaction mechanism for low energy photons (up to 200 keV in germanium). The photon is completely absorbed by a bound atomic electron, transferring all of the photon's energy to the electron which is subsequently ejected from the atom. The energy of the outgoing photo-electron is given by following simple equation:

$$E_{e-} = E_\gamma - E_b \tag{2.3}$$

where E_b is the atomic electrons binding energy and E_γ is the energy of the incident photon. No single valid expression exists for the cross-section of the photoelectric effect which can be applied to all photon energies and atomic number (Z) but the

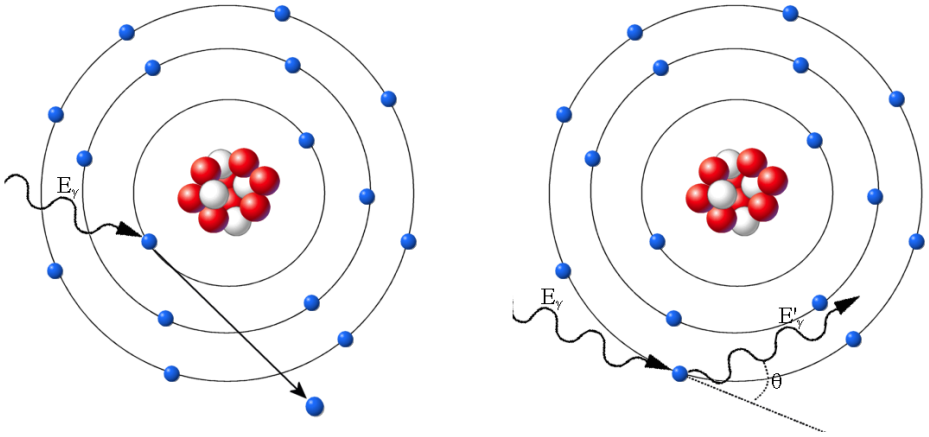

Figure 2.3: Illustration of the two most significant interaction mechanisms of gamma-rays with matter in the energy range 10-2,000 keV. Left: The photoelectric effect Right: Compton scattering.

probability is approximately given by [Dav52]:

$$\sigma_{pe}(E_\gamma, Z) \approx C \times \frac{Z^n}{E_\gamma^{\sim 3}} \tag{2.4}$$

Where C is a constant and n is a value typically between 4 and 5. The vacancy left by the ejected electron in the atomic shell (usually the k shell) is filled by electron rearrangement with the energy being carried away in the form of x-rays or Auger electrons.

2.3.2 Compton scattering

For photons with energies between ~200 keV and 10 MeV the dominant interaction mechanism is Compton scattering. The photon of incident energy E_γ scatters off a weakly bound atomic electron transferring a fraction of its energy to the electron. The incoming photon is scattered through an angle θ between 0 and 180 degrees with a reduced energy E'_γ. Assuming the electron is unbound and at rest, from conservation of energy and momentum, the energy of the scattered photon is related to the incident energy and scattering angle by equation 2.5.

$$E'_\gamma = \frac{E_\gamma}{1 + \frac{E_\gamma}{m_0 c^2}(1 - \cos\theta)} \tag{2.5}$$

The maximum kinetic energy that can be transferred to the recoil electron T_{max}, occurs when $\theta = 180^o$. From equation 2.5 it can be shown that the maximum value is given by:

$$T_{max} = E_\gamma \frac{2\alpha}{1 + 2\alpha} \tag{2.6}$$

where $\alpha = E_\gamma / m_0 c^2$. At 511 keV $\alpha = 1$ and hence $T_{max} = 2/3$ x 511 $\approx$ 340 keV. This fixed maximum value for a single incident energy gives rise to the characteristic feature observed in gamma-ray energy spectra known as the *Compton edge*.

The scattering angle distribution for a given energy E_γ is not constant, the differential scattering cross-section is given by the Klein-Nishina formula [Dav65]. At 511 keV photons are highly forward focused as shown in figure 2.4

2.3.3 Total cross-section and attenuation

The total cross-section for a photon interacting in a material is simply given by the sum of each possible interaction processes individual cross-section:

$$\sigma_{total} = \sigma_{phot} + \sigma_{compt} + \sigma_{pair} + \sigma_{thom} + \sigma_{rayl} \tag{2.7}$$

The linear attenuation coefficient μ, defined as the fraction of a beam of x-rays or gamma rays that are absorbed or scattered per unit thickness of the absorber material, is proportional to the total cross-section:

$$\mu = N\sigma_{total} = \frac{N_a \rho}{A}\sigma_{total} \tag{2.8}$$

where N is the density of atoms, N_a is Avogadro's constant, ρ the material's density and A the molecular weight. The attenuation of a collimated beam of initial intensity I_0 is $I = I_0 e^{-\mu x}$. The linear attenuation of the important processes as a function of energy for germanium are shown in figure 2.5.

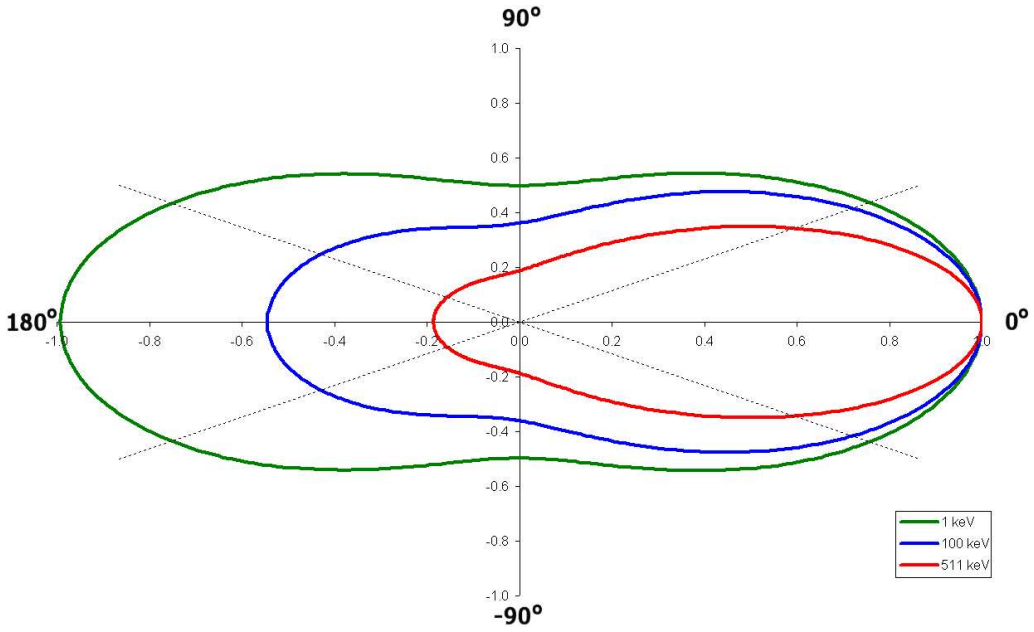

Figure 2.4: Polar-plot showing the Compton scattering cross-section against deflection angle θ for 1, 100 and 511 keV photons. At 511 keV forward focused scattering is highly probable. The dotted lines show the $\pm 30^o$ angle which is approximately half the detector opening angle for the experiments outlined later in chapter 5.

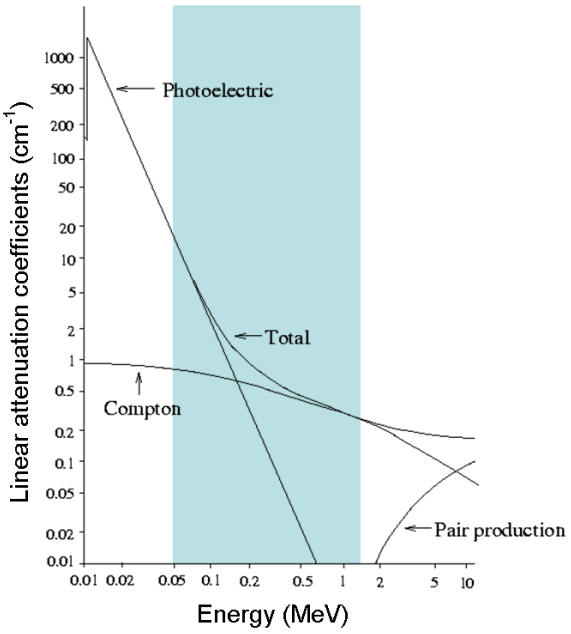

Figure 2.5: Linear attenuation coefficients for the individual interaction mechanisms photoelectric, Compton and pair production along with the total attenuation as a function of energy in germanium. The shaded area indicates the energy range of importance in PET studies.

An understanding of attenuation is important in medical imaging applications. Attenuation coefficients in the body vary greatly between the bone and soft tissue. The simple illustration [figure 2.6] demonstrates why projection data in PET needs to be corrected for attenuation.

Most commercial PET scanners now incorporate a x-ray Computed Tomography scanner into the same device housing the PET system to allow for measurements of the attenuation or transmission map prior to the positron imaging stage [Tow03].

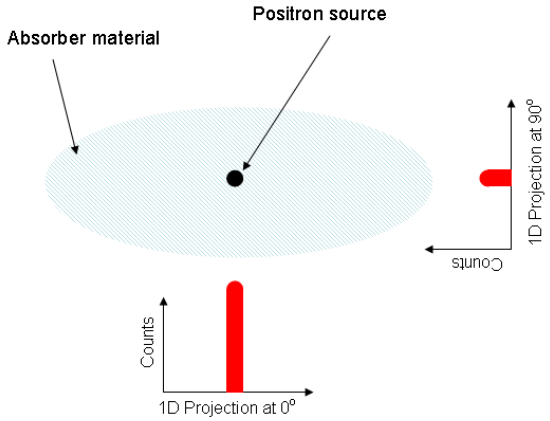

Figure 2.6: The presence of an absorber material causes attenuation of the photons from the source. The total number of coincidence events varies as a function of the projection angle θ.

Chapter 3

Semiconductor physics

3.1 Introduction

Solid state detectors, due to density properties provide much higher sensitivities than their gas based counterparts. Therefore PET systems are almost exclusively based on scintillator or semiconductor materials. Semiconductors have found wide-spread usage as radiation detectors in many fields including nuclear, particle and astrophysics. The reason semiconductors are so important is due to their electrical properties and hence excellent intrinsic energy resolution. The energy resolution of a typical scintillator such as bismuth germinate (BGO) is ∼10% FWHM for a 511 keV photon. Compared with a value of ∼0.4% at the same energy in a germanium semiconductor detector. The vast improvement in energy discrimination makes semiconductor detectors excellent for spectrometry based applications.

3.2 Semiconductor band-gap properties

In semiconductors like insulators the Fermi level lies between the filled valence band and unfilled conduction band. Both have zero conductivity at 0k. The band-gap between the valence and conduction bands in a semiconductor material is much smaller than in insulators. At moderate temperatures the gap is small enough to allow some

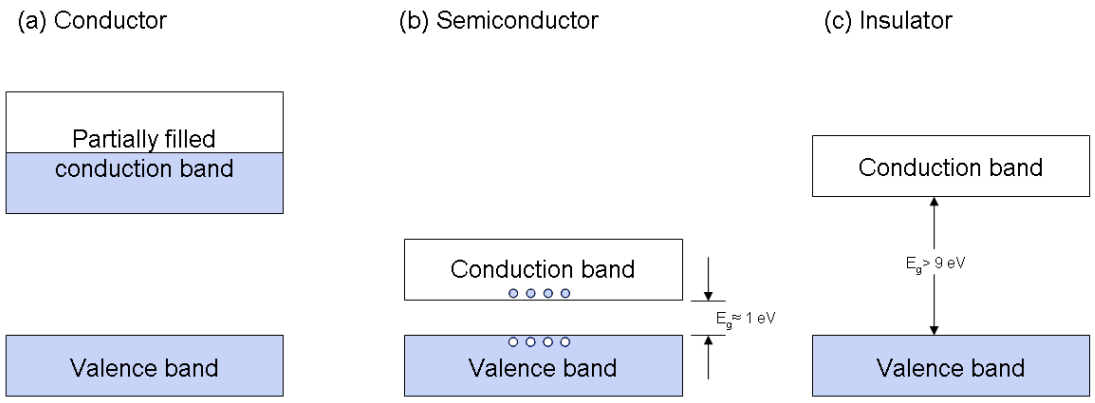

Figure 3.1: Energy band diagram for conductors, semiconductors and insulators.

valence electrons to be thermally excited into the conduction band. Figure 3.1 shows a basic schematic of the difference between the allowed electron energy levels in conductors, semiconductors and insulators. Electrons excited into the conduction band and the associated hole left in the valence band form what is known as an electron-hole pairs. Under the influence of an electric field E, these electrons and holes migrate in opposite directions through the material leading to a drift current flow with a density given by:

$$J = \mid e \mid E(n\mu_n + p\mu_p) \tag{3.1}$$

where n is the number of electrons in the conduction band, p is the number of holes in the conduction band μ_n and μ_p are the electron and hole mobilities.

3.2.1 Doping

The electronic properties of a semiconductor can be altered in a controllable manner by adding small amounts of impurities. These impurity atoms modify the effective band-gap structure, introducing additional energy levels in the forbidden region between the valence and conduction band. The impurities are called dopants and come in two forms; donors from group V in the periodic table which have an extra electron or acceptors from group III with one less electron. Doping with donors (acceptors)

is known as n-type (p-type) doping. The semiconductor is then said to be of n-type (p-type) and has an abundance of extra electrons (holes).

3.2.2 The p-n junction

A p-n junction is formed when a single crystal of semiconducting material is both p-type and n-type doped in different areas. At the junction between the two doping types some of the free electrons in the n-region will diffuse across the junction and combine with the holes in the p-region, leading to a negative ion concentration in the p-region. This equivalently leads to a concentration of positive ions on the n-type side of the junction. A negative space charge forms near the p-type region and a positive space charge near the n-type. The space charge region induces an electric field directed from the positive charge to the negative, in the opposite direction to the diffusion current. At some point therefore the electrons migrating across the junction reach an equilibrium. The drift current due to the electric field cancels out the diffusion current due to the concentration gradient.

A photon interacting with the germanium in the depletion region will produce electron-hole pairs which may then be swept to the edges of the crystal due to the electric field gradient, constituting an electric current.

Applying a reverse voltage (bias) across the junction further hinders electron diffusion, attracting any free electrons away from the junction. At the same time the negative voltage applied to the p-type end also attracts holes away from the junction. The consequence of applying the reverse bias is that all available charge carriers are attracted away from the junction, and the depletion region effectively grows larger. The total width of the depletion region is given by [Sze02a]:

$$d = \sqrt{\frac{2\epsilon_r V}{eN}} \tag{3.2}$$

where V is the applied bias, N is the impurity concentration and ϵ_r the materials dielectric constant.

3.2.3 Germanium

Germanium is a single element semiconductor found in group IV of the periodic table. It's atomic number (Z=32) compared with that of silicon (Z=14) makes it an excellent element for photon detection. Germanium has a face-centred cubic (FCC) crystalline structure with a two atom basis. Further physical properties of germanium are tabulated in 3.1. Due to the small band-gap electrons are thermally excited into the conduction band at room temperature. Therefore to reduce this potential source of noise germanium needs to be cooled and is typically operated at liquid nitrogen temperatures.

The two most common detector designs are the closed end coaxial and planar configurations. Coaxial detectors can be manufactured with a larger active detection area but have more complex electric fields, especially in the front face of the detector. Both geometries can be manufactured with electrical segmentation which divides the detector into multiple sections. The two planar detectors used in this study are segmented using double sided orthogonal strips.

3.3 Charge carrier production in germanium

The photoelectron produced following the interaction of a photon in the detector will lose energy via two processes, impact ionisation and radiation emission. Impact ionisation is the dominant interaction mechanism at lower energies and is given by the Bethe-Block formula [Leo93]. Radiation emission (Brehmstrahlung) becomes prevalent at several tens of MeV. The energy loss for the photoelectron is given by the sum of the two processes [equation 3.3].

$$\frac{dE}{dx}_{total} = \frac{dE}{dx}_{ion} + \frac{dE}{dx}_{rad} \tag{3.3}$$

For a photoelectron of energy E the number of electron-hole pairs generated N, after total energy loss is given by:

$$N = \frac{E}{\epsilon_{pair}} \tag{3.4}$$

Atomic Number A	32
Atomic Weight Z	72.6
Atoms	4.4×10^{22} cm^3
Density	5.32 g/cm^{-3}
Dielectric constant ϵ_r	16.2
Intrinsic carrier concentration (300 K)	2.0×10^{13} cm^{-3}
Intrinsic resistivity	46 Ω·cm
Energy gap (300 K)	0.67 eV
Energy gap (0 K)	0.75 eV
Ionisation energy (77 K) ϵ_{pair}	2.96 eV
Fano factor (77 K)	0.08
Electron mobility (300 K)	3900 cm^{2}V·s
Hole mobility (300 K)	1900 cm^{2}V·s
Lattice constant (a)	565.75 pm

Table 3.1: Physical properties of intrinsic germanium [Kno00a]

where ϵ_{pair} is the average ionisation energy, the energy required to excite one electron from the valence band. Some of the available energy is dissipated in lattice vibrations therefore ϵ_{pair} is a statistical value and is necessarily greater than the band gap energy.

When considering the variation in the numbers of electron-hole pairs created for a given energy Poisson statistical models cannot strictly be applied. Poisson statistics applies to independent processes whereas in our case the production of one electron-hole pair affects the probability of another pair being created. Fano [Fan47] introduced an experimentally calculated correction factor F, to account for the difference between a Poisson model and the observed results.

$$\sigma_N = \sqrt{FN} = \sqrt{F\frac{E}{\epsilon_{pair}}} \tag{3.5}$$

A Fano factor of unity indicates an independent process in agreement with Poisson statistics. In germanium at an operating temperature of $77K$ $F \simeq 0.08$.

3.4 Signal generation

The electric field created by the p-n junction itself is too small to prevent large scale electron-hole recombination. Under the influence of the applied reverse biased field the electron-hole pairs do not recombine but instead drift towards the electrodes. The field strength at any point within the detector crystal can be calculated by solving the Poisson equation which in one dimension is given by:

$$\frac{d^2V(x)}{dx^2} = -\frac{\rho(x)}{\epsilon_r} \tag{3.6}$$

where $V(x)$ is the electric potential, $\rho(x)$ is the charge density and ϵ_r is the dielectric constant of the material. For a planar detector configuration the value of the electric field in the uniform section of the detector is given by [Kno00b]:

$$\mid E(x) \mid = \frac{V}{d} + \frac{eN_a}{\epsilon_r}\left(x - \frac{d}{2}\right) \tag{3.7}$$

Charge carriers moving in the vicinity of an electrode maintained at constant potential induce a current to flow in the external field. The instantaneous value of this current

for a planar detector is given by Ramo's theorem [Ram39]:

$$i(t) = q\frac{E(x)v_d(x,t)}{V(x)} \tag{3.8}$$

where $E(x)$ is the electric field strength and v_d is the drift velocity of the charge carriers. For a multi-electrode device the induced current is calculated based on an extension to Ramo's theorem known as Green's reciprocity theorem. The induced charge on one electrode is given by [Rad88a]:

$$i(t) = qE_w v_d(x,t) \tag{3.9}$$

where E_w is the weighting field, an artificial field which provides a measure of the electrostatic coupling between the moving charge and the electrode of interest. v_d is the drift velocity. Figure 3.2 illustrates the idea of the weighting field for a multi-strip planar detector and shows the variation of the induced current with time for two separate strips.

Ortec designed, charge sensitive preamplifiers integrate the incoming current pulse from the detector onto a capacitor which is then discharged by a resistive feedback circuit [Kno00c]. The resultant charge pulse is characterised by a fast leading edge which relates to the charge collection time within the detector and a slow exponential decay.

3.4.1 Real charge events

The real or net charge is the term given to the time varying charge pulse measured by the electrode collecting the electrons or holes. An example real charge pulse shape is presented in figure 3.3. The maximum amplitude of the pulse is proportional to the energy deposited in the interaction. The shape of the initial rising edge of the pulse provides information about the depth of interaction in a planar detector. Pulse Shape Analysis (PSA) is a technique which involves quantifying the properties of the digitally sampled electrode response to provide information about the interaction location in the detector to higher precision than due to the strip size itself.

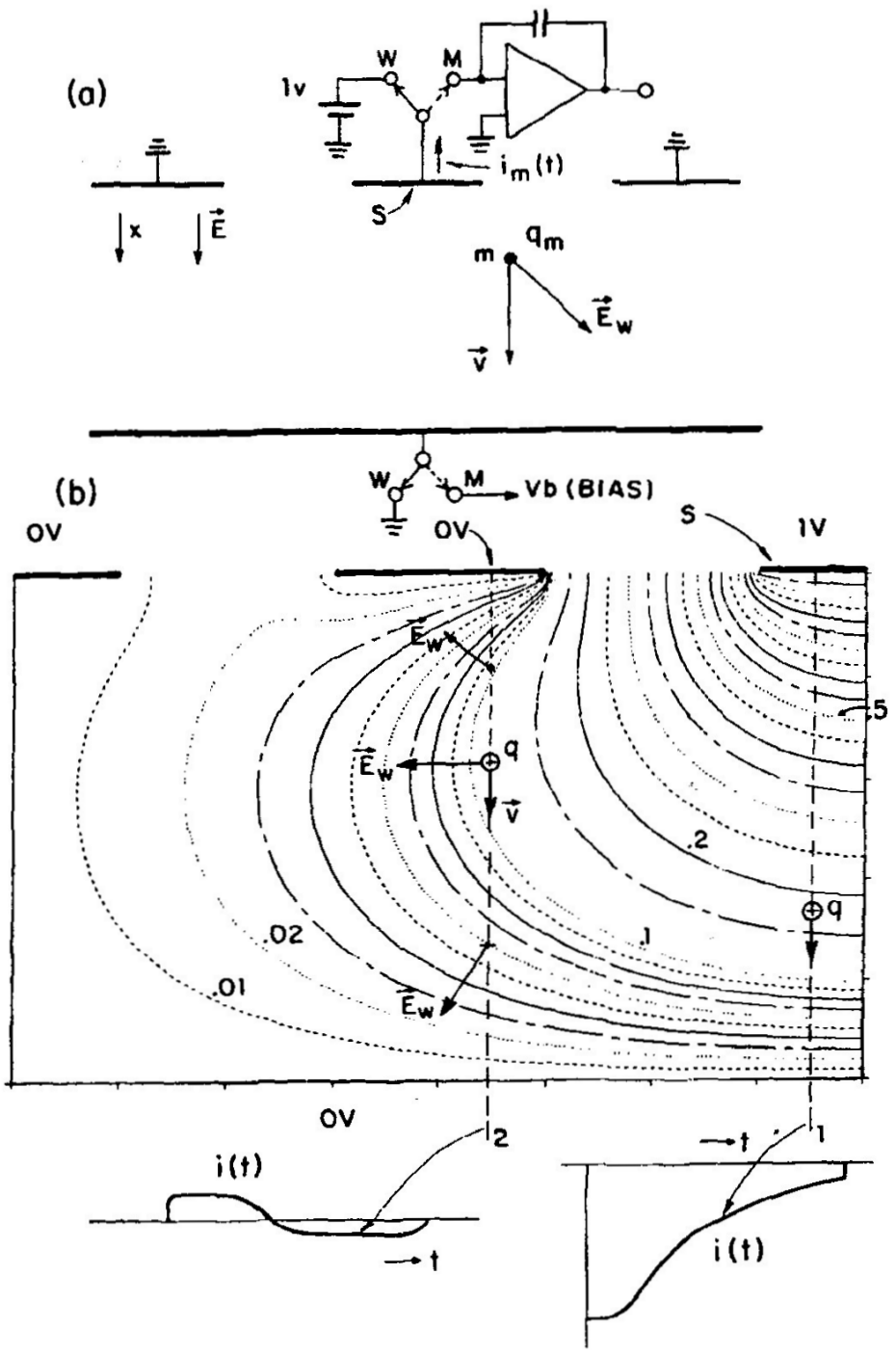

Figure 3.2: Illustration of the weighting field concept and its use in determining the induced current on a multi-electrode planar detector configuration. The weighting field is plotted with respect to the sensing electrode S as a set of equipotential lines. For two possible interaction locations the induced charge on S is shown depicting the difference between real and image charge [Rad88b].

3.4.2 Image charge events

All other electrodes not precipitating in the charge collection process will see an induced pulse shape with no net height variation. Generally the signal is only measurable above the noise for the nearest neighbour electrodes either side of the real charge collecting strip. These pulses are often termed image, transient or mirror charges. Example image charges are shown in figure 3.3.

The asymmetry between the two nearest neighbour strips on either side of the net charge provides information about the lateral x-y position of the interaction. A variable such as the gross area of the image charge from each neighbour can be used to calculate the asymmetry parameter:

$$\text{Asym} = \frac{A_{left} - A_{right}}{A_{left} + A_{right}} \tag{3.10}$$

Calibration of the asymmetry as a function of interaction position for each detector strip provides a means of position determination on an event-by-event basis.

3.4.3 Convolved charge events

Multiple gamma-ray interactions within the detector located in adjacent strips leads to pulse shapes which have a convolved real and image charge response. While deconvolution of these events is an on-going research topic they can be identified and removed from the data set used for imaging with relative ease.

Multiple interactions within a single strip (but at different positions) pose a bigger problem for PSA methods and again their unravelling is an active research topic. For PET imaging the location of the first interaction is of importance. Multiple interactions within a strip have diminishing consequence on the image reconstruction for interaction points located closer together.

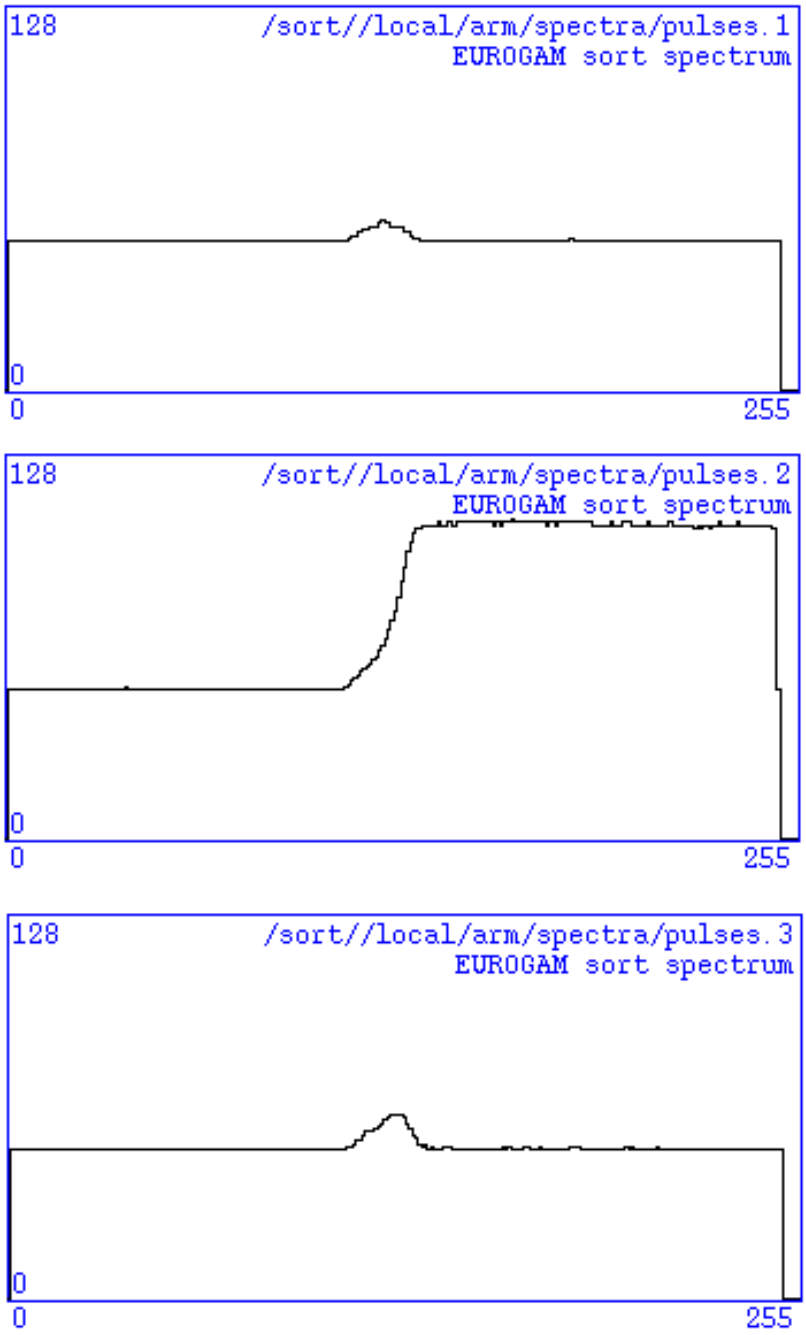

Figure 3.3: The pulse shapes from three adjacent strips on one face of a SmartPET detector. A gamma-ray has interacted in the middle strip leaving a real charge event with a magnitude proportional to the deposited energy and rising edge profile related to the interaction depth. The two spectator strips either side see a positive image charge, the relative size of these image charges provides details about the lateral position of interaction. The shape of the image charge also contains some depth information but the smaller signal size and hence lower SNR can hinder its usefulness.

3.5 Energy resolution

The energy resolution of a germanium detector is typically quoted as the FWHM of a specified photopeak from a mono-energetic gamma-ray. The overall energy resolution of the detector, ΔE^2_{total} is influenced by three intrinsic system factors and a Doppler based term added in quadrature:

$$\Delta E^2_{total} = \Delta E^2_{stat} + \Delta E^2_{char} + \Delta E^2_{elec} + \Delta E^2_{dop} \tag{3.11}$$

- ΔE_{stat} relates to the statistical variation in the number of charge carriers created:

  $$\Delta E^2_{stat} = 2.35^2 \, F \, \epsilon_{pair} \, E \tag{3.12}$$

  where E is the photon energy. F is the Fano factor introduced earlier, ϵ_{pair} is the energy required to create a single electron-hole pair.

- ΔE_{char} is the contribution due to incomplete charge collection within the detector volume. The effect becomes more dominant in larger volume detectors.

- ΔE_{elec} represents the broadening effect due to all of the electrical components following the detector.

- ΔE_{dop} arises due to Doppler broadening related to the velocity of the source nuclide if travelling close to the speed of light and the angle subtended by the detector geometry in relation to the source.

The superior energy resolution of a semiconductor like germanium compared with scintillator detectors arises predominantly due to the value of ϵ_{pair} (2.96 eV) in comparison to the scintillator equivalent which is of the order 100eV. A scintillator intrinsic energy resolution is dominated by this statistical variation in created charge carrier numbers.

3.6 Timing resolution

The total rise-time of a real charge pulse is typically of the order ~100-250ns. The time arises as a result of the finite velocity of the charge carriers which is of the order 1cm per 100ns and is affected by a number of factors; the detector size, geometry, impurities, applied electric field and interaction position.

Of greater importance to this research is the time resolution of a germanium coincidence system. This is defined as the FWHM of the distribution curve of time intervals between the detection of two gamma-rays emitted almost simultaneously. A time resolution of the order 5-10ns is obtainable with the appropriate fast timing electronics for this detector.

3.7 Efficiency

The efficiency of a germanium detector can be quoted in a variety of ways depending on the required use and therefore it is of importance when considering efficiencies to understand these differences. The main efficiency measures are outlined below:

1. Absolute efficiency is given by the ratio of photons detected to the number emitted:

$$\epsilon_{abs} = \frac{Number\,of\,detected\,photons}{Number\,of\,emitted\,photons} \tag{3.13}$$

   The efficiency may be quoted for full energy depositing events at a given energy only (photopeak) or for all energy depositing events. Absolute efficiency measurements are influenced by the source-detector geometry. Absolute efficiency is important in PET when comparing two competing commercial scanner designs due to the influence this has over the time or dose level required to achieve the same number of recorded events.

2. Intrinsic efficiency compares the ratio of photons detected to the number incident on the detector.

$$\epsilon_{in} = \frac{Number\,of\,detected\,photons}{Number\,of\,emitted\,photons\,incident\,on\,detector} \tag{3.14}$$

Similarly to absolute efficiency the value can be given for full energy or all events. The advantage of intrinsic efficiency is the value is no longer relative to a certain source-detector setup. Intrinsic efficiency is a useful quantity when comparing different materials properties for use in PET systems.

3. Relative efficiency relates the detectors performance compared to that of a 76mm^2 NaI(Tl) scintillator detector for the 1332 keV gamma-ray from a ^{60}Co source placed 25cm from the front face of the detector. Relative efficiency is a historical solution for comparing different shapes, sizes and material detectors for use in gamma-ray detection. The criteria for calculating relative efficiency can also be applied to gamma-ray energies other than 1332keV to provide a means of understanding performance as a function of incident energy.

Chapter 4

Image reconstruction techniques

4.1 Data acquisition considerations for imaging

A number of detector geometries exist for clinical and research PET systems. The two most prominent designs include a complete ring of detector elements in which all projections are measured simultaneously or a rotating dual-headed detector configuration. SmartPET is a rotating dual-head planar system in which the two germanium detectors provide position sensitivity. This position sensitivity effectively creates many quasi-detector elements which can be generally treated as equivalent to a large number of smaller independent detectors. Dual-headed configurations are typically cheaper to produce, due to the smaller quantity of detector material and read-out electronics needed. These systems require the detectors (or patient) to be rotated through 180 degrees in order to build a complete data set from which to image. Hence rotational systems generally require longer duration scans to achieve the same level of statistics.

All PET systems count coincidence events between pairs of detectors or quasi-detector elements. A coincidence is defined as two separate detector elements measuring an energy deposit within a small temporal window known as a coincidence window. Further conditions may also apply such as the energy deposited in both detectors passing a specified energy gate and the line joining the two detectors having

a valid acceptance angle.

The line joining two detector elements allowed to form a valid coincidence event is known as a Line Of Response (LOR) or Tube of Response (TOR) if the finite detector face area is considered. Image reconstruction in PET is built on the assumption that the positron decay occurred somewhere along the line joining the two detectors.

Localising the decay position more accurately from time-of-flight (TOF) measurements is possible with sub-nanosecond timing performance. From speed of light calculations a timing uncertainty of 1ns corresponds to a 15cm uncertainty in spatial resolution. Semiconductors and most scintillator detectors and their electronics do not possess such timing properties and hence can not measure the difference in arrival times of the two photons[1]. Commercial whole-body scanners based on the scintillators BGO, GSO and LSO have factory default coincidence windows of 12, 8 and 6ns respectively [Tar03]. The scintillator material lanthanum bromide ($LaBr_3$) is currently receiving substantial interest from the research community and shows great promise. The excellent energy, timing and efficiency properties suggest this scintillator will play an important role in future PET systems once manufacturing issues are overcome.

4.1.1 Coincidence event categories

Events labelled as coincidence after passing the timing, energy and spatial criteria can be sub-divided into four categories [Fig 4.1].

1. *True coincidence* events in which both detected photons belong to the same positron decay and neither photon has significantly interacted in the surrounding material before both reaching opposite sides of the tomograph. These are the ideal imaging events.

[1] The scintillators BaF_2 and CsF are able to produce the timing resolution needed for TOF-PET, there is also renewed interest in the research arena for TOF-PET using LSO [Mos03a]

2. *Random* or *accidental coincidence* events arise when two unrelated positron decays occur within the timing window but only one photon from each decay is detected and are assumed to have originated from the same decay. In this case an incorrect LOR is assigned. The fraction of randoms is related to the activity of the source and the width of the coincidence window.

3. *Scatter coincidence* events occur when one or both of the photons from a single decay Compton scatter before reaching the detector system. Compton scattering will cause an energy loss and change in direction of the photon [Ch 2.3.2]. However if the energy loss is small enough the photon can still pass the applied energy gate. The fraction of scatter events is not a function of activity but constant for a given object and tracer distribution. The width of the photopeak energy window and the intrinsic energy resolution of the detector material used determines the probability of failing to identify scatter events.

4. *Multiple coincidence* events involve the detection of more than two photons within the timing coincidence window. Due to the ambiguity in assigning a LOR these events are generally rejected and not used by the imaging algorithms. Like randoms the fraction of multiple events is a function of source activity and coincidence window width.

PET systems aim to minimise the fraction of random and scattered coincidence events. Improved timing resolution can reduce the number of randoms but the window must be wide enough to allow for the finite photon travel times across the scanner. The improved energy resolution of germanium allows an energy gate width of around 2 keV compared with 300 keV for a typical commercial BGO detector [Tar03]. This can potentially allow scatter event discrimination orders of magnitude beyond that available to the conventional scintillator based systems. Using equation 2.5 the scintillator energy window can potentially fail to detect scatters of up to 60^o while for germanium the value is around 5^o.

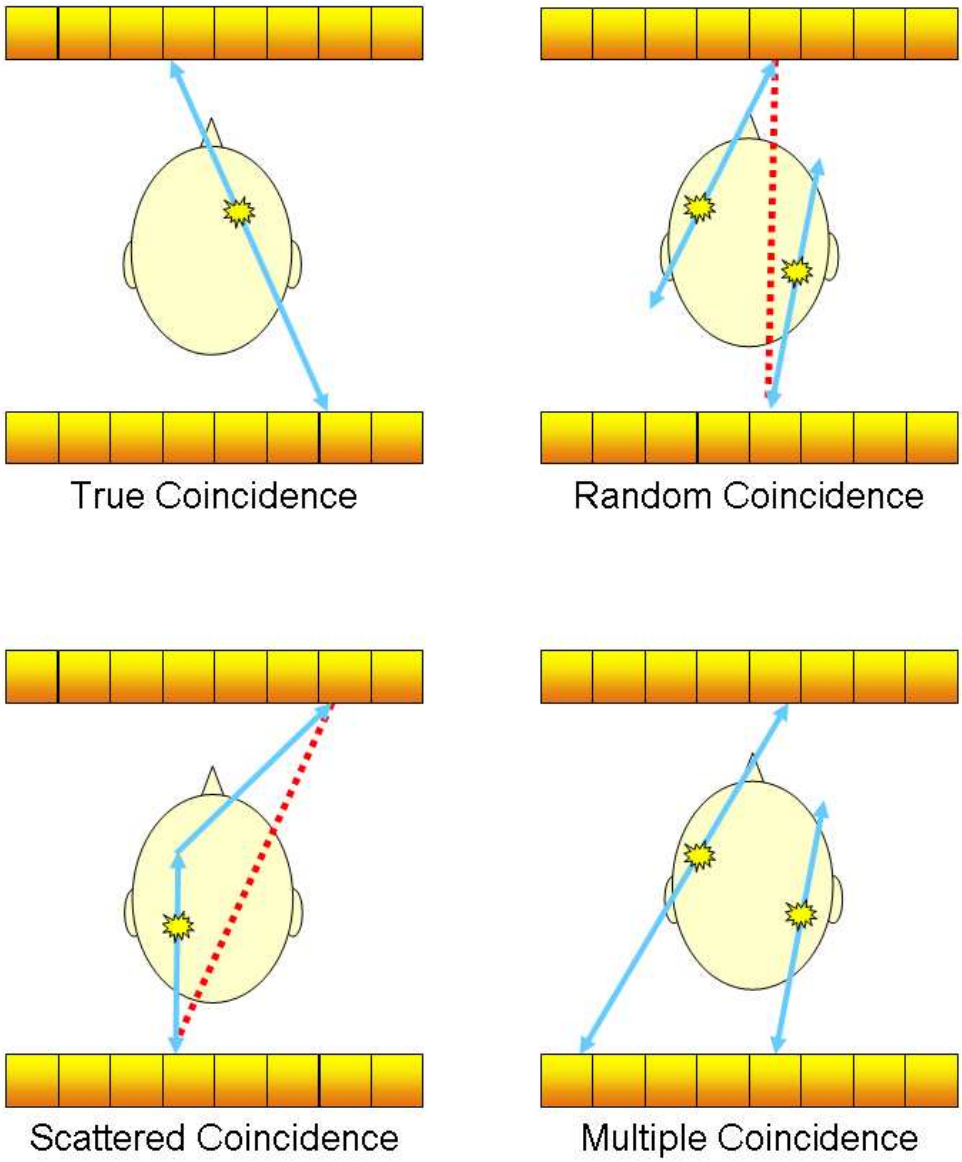

Figure 4.1: Diagrammatic representation of the four different coincidence events that are recorded by a PET scanner. A whole-body PET system operating in 3D mode for a typical scan would measure 50% random events, 25% scatter and 25% true [Mos03b].

Some fraction of random and scattered events will always ultimately be included in the coincidence count rate which must be accounted for in some way. Random events can either be estimated using a delayed coincidence window in which only randoms will be measured or from the singles count rate between each pair of detector elements using equation 4.1.

$$R_{ab} = 2\tau N_a N_b \tag{4.1}$$

Where $N_{a,b}$ is the singles rate of each element and 2τ is the coincidence window width. Estimations of the average number of random coincidences for each LOR can be used to improve image reconstruction. These estimated values are either subtracted from the total count rate or in the case of iterative algorithms modelled as part of the system matrix [Ch 4.4.1].

4.1.2 Initial SmartPET imaging considerations

A large number of image reconstruction techniques exist today, many of the methods have the same theoretical basis but different implementations [Def03a] [Oll97]. The choice of algorithm and it's implementation is highly influenced by the scanner data acquisition methodology and operating parameters.

The following discussion provides a brief overview of how the SmartPET system configuration effects the image reconstruction process. Event selection criteria for the initial SmartPET imaging which impact the reconstruction algorithm are also outlined.

Multiple slice 2D imaging

The initial imaging has focused on reconstructing sets of two dimensional slices along the rotation axis. The imaging discussion presented will therefore be limited to multiple slice 2D methods rather than fully three dimensional reconstruction techniques. Both analytic and iterative imaging algorithms have been applied, further details concerning the algorithms are provided later in this chapter.

LOR usage for imaging

The number of counts in all possible LOR between the two planer detectors are measured during acquisition. Current SmartPET image reconstruction is based primarily on the parallel beam fraction of LORs. Use of the quasi-parallel LORs connecting 'opposite-but-one' detector elements is also studied. The additional LOR is assumed to also be parallel and positioned centrally between the two true parallel lines. This increases the number of bins, and slices from N to $N(N-1)$, where N is the number of effective detector elements.

Data acquisition model

PET acquisition systems record events in either a histogram mode or as a simple list. With commercial scanners the number of LORs is often greater than the number of events recorded in a typical scan i.e. most LORs do not measure many events. In this situation it is common to rebin LORs close to each other to improve signal to noise, at the cost of some spatial resolution. Recent developments in iterative image reconstruction however utilise a list mode data set and hence have no need for rebinning and the associated loss of spatial resolution [Rea98]. The initial work presented using the SmartPET detectors does not require the rebinning operation mentioned to overcome statistical limitations therefore image reconstruction has been based on histogram data. Due to the data collection techniques currently employed it remains possible to reconstruct using list mode algorithms in the future from the same collected data set.

4.2 The sinogram

The sinogram provides a simple and universal framework to describe the measured LOR count data from a complete PET scan. The sinogram matrix, typically two dimensional, is passed to the reconstruction algorithms from which a resultant image is calculated. The following section provides an introduction to the sinogram in

preparation for discussion of the algorithms applied to it during image reconstruction.

4.2.1 Line integrals, projections and sinograms

A pair of detectors d_a and d_b form a LOR, $L_{d_a d_b}$. The number of counts measured by the LOR is a Poisson variable with a mean value $\langle p_{d_a d_b} \rangle$ given by:

$$\langle p_{d_a d_b} \rangle = \tau \int_{FOV} d\vec{r} f(\vec{r}) \psi_{d_a, d_b}(\vec{r}) \tag{4.2}$$

Where τ is the acquisition time and $f(\vec{r})$ is the tracer distribution, assumed to have no time dependence. $\psi_{d_a, d_b}(\vec{r})$ is a sensitivity function. For data pre-corrected for scatter and random events the sensitivity function is zero except along the line or tube joining the two detector elements. This is because the corrected data will contain just true coincidence events which only occur along the LOR between the two detectors[2]. The equation then simplifies to the line integral of the positron-decay distribution between the detectors [equation 4.3].

$$\langle p_{d_a d_b} \rangle = \tau \int_{L_{d_a d_b}} d\vec{r} f(\vec{r}) \tag{4.3}$$

Consider a fixed angle θ, where θ is the angle of rotation of the complete detector system from a defined axis x. The combination of each of the equally spaced parallel beam LORs forms a one dimensional projection of the source distribution, $p_\theta(t)$.

Figure 4.2 shows two independent measured 1D projections of a 2D source distribution $f(x, y)$ at fixed angles θ_1 and θ_2. Combining all the equally spaced projections between 0 and 180^o provides a two dimensional distribution $p(t, \theta)$ called a sinogram. Tomographic image reconstruction can be understood as the process of calculating the source distribution $f(x, y)$ from knowledge of the sinogram $p(t, \theta)$.

Measured data may not naturally form an equally distributed (parallel beam) sinogram which is often a requirement of image reconstruction algorithms. In these cases interpolation methods are employed to recover an uniformly spaced Cartesian

[2]Ignoring the affect of non-collinear photons.

grid. The SmartPET rotating planar geometry means such interpolation is not required if just the parallel beam LORs are considered and the angular sampling is stepped in equal increments.

4.2.2 Theoretical sinogram generation

During the course of this research software has been developed to calculate ideal sinograms from greyscale images which represent a source distribution $f(x, y)$. The simulated sinograms allow for the testing and development of the image reconstruction code prior to the commissioning of the SmartPET detectors. Figure 4.3 shows sinograms generated using this software. A complete guide to the software is presented in Appendix B.

4.3 Analytical reconstruction

Recovering the source distribution from projection data analytically first requires the formulation of mathematics describing the relationship between the continuous source distribution and an infinite set of projections. From this an inverse operation can be sought which can be applied to the discrete data set measured.

The mathematical problem of two dimensional reconstruction from an infinite number of one dimensional projections was solved by Johann Radon in 1917 [Rad17] long before the invention of CT or PET scanners.

4.3.1 Radon Transform

The Radon Transform[3] (RT) [Dea83] of a distribution $f(x, y)$ is given by the line integral:

$$p(t, \theta) = \int_l f(x, y)\, dl \tag{4.4}$$

[3]Also known as the x-ray transform.

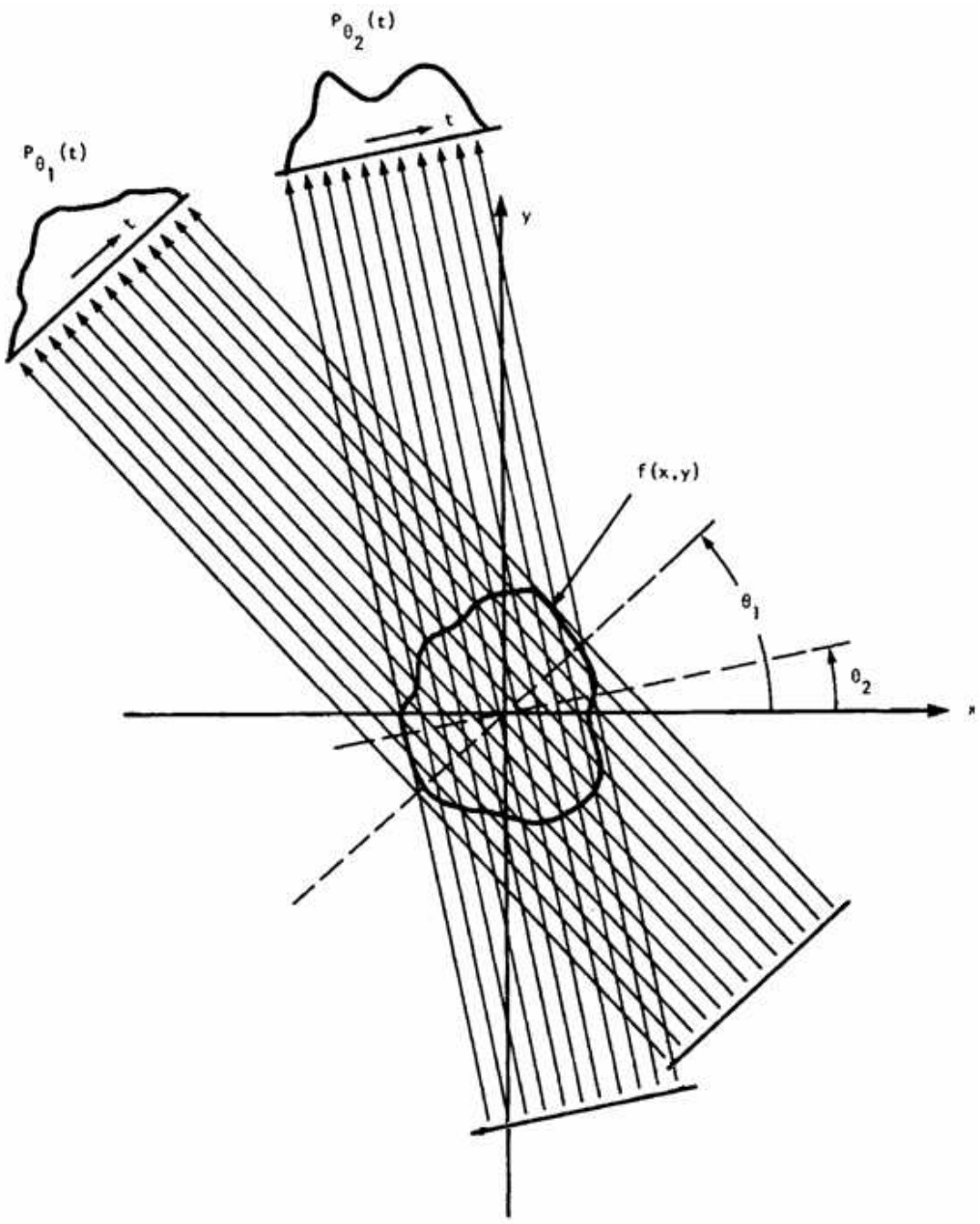

Figure 4.2: A uniform source distribution $f(x, y)$ is sampled at two angles θ_1 and θ_2 giving two 1D projections, $p_{\theta_1}(t)$ and $p_{\theta_2}(t)$ where t is the co-ordinate along the projection axis. For full coverage projections need to be considered in the range $0^o \leq \theta$ $<180^o$, beyond this range angles are just effectively resampled with the two detectors interchanged.

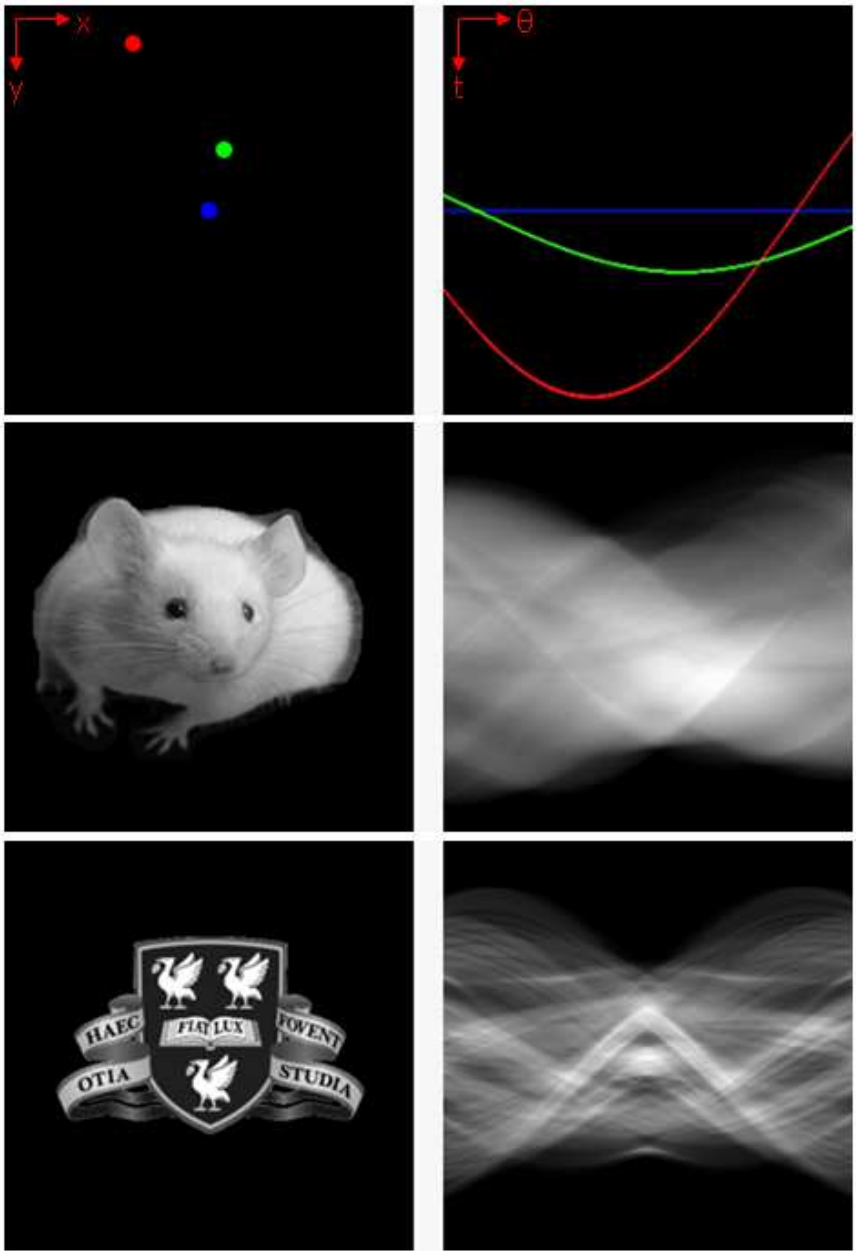

Figure 4.3: Three different greyscale base images (left) and their generated sinograms (right) using 256 projections and 256 detector elements with no induced noise. **Top:** Three point sources artificially coloured to emphasise the origin of the name *sinogram* i.e. a point source will follow a sinusoidal path through the sinogram. **Middle:** Sinogram generated from an image of a small animal. **Bottom:** Sinogram associated with the University of Liverpool's crest.

From geometric transform equations all points on the line must satisfy the equation $t = x\cos\theta + y\sin\theta$. Therefore equation 4.4 can be rewritten:

$$p(t,\theta) = \int\int f(x,y)\,\delta(x\cos\theta + y\sin\theta - t)\,dx\,dy \tag{4.5}$$

Solving the inverse Radon Transform provides a mathematical solution to recovering $f(x,y)$ given the projection data $p(t,\theta)$.

4.3.2 Central Slice Theorem

The solution to the inverse RT is based on the Central Slice Theorem (CST) [Bar04]. The CST relates the two dimensional Fourier transform of the distribution $F(v_x, v_y)$ to the one dimensional Fourier transform of the projection data $P(v,\theta)$ with the following equation:

$$P(v,\theta) = F(v\cos\theta, v\sin\theta) \tag{4.6}$$

Therefore with an infinite number of projections all of $F(v_x, v_y)$ can be mapped and a two dimensional FT of $F(v_x, v_y)$ yields $f(x,y)$. Reconstruction algorithms based on direct Fourier reconstruction use this approach.

4.3.3 Simple Backprojection

Another approach to image reconstruction is to simply project the measured values back through the image space. Mathematically backprojection is defined in equation 4.7 for continuous data, and equation 4.8 for a finite set of N evenly spaced projections spanning the range $0^o \leq \theta < 180^o$ [Pan99].

$$f_{BP}(x,y) = \int_0^{\pi} p(x\cos\theta + y\sin\theta\,,\,\theta)\,d\theta \tag{4.7}$$

$$f_{BP}(x,y) = \sum_{i=0}^{N} p(x\cos\theta_i + y\sin\theta_i\,,\,\theta_i)\,\frac{N}{\pi} \qquad \theta_i = \frac{i\pi}{N} \tag{4.8}$$

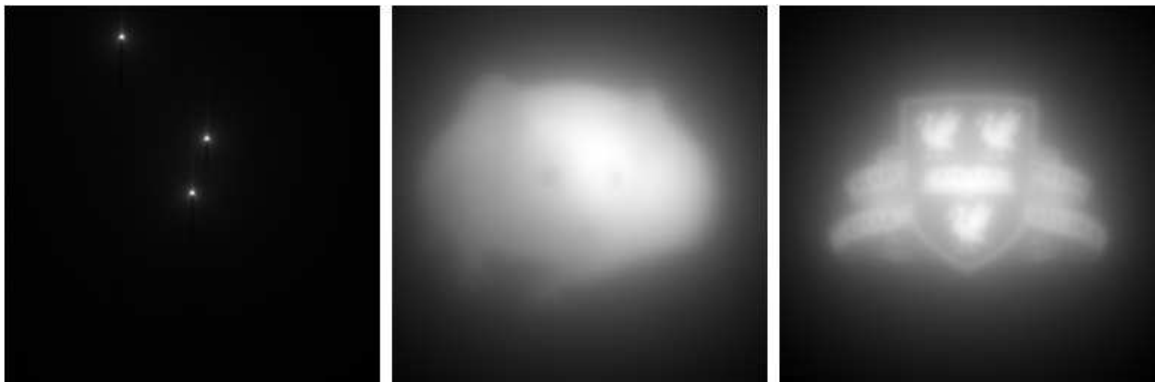

Figure 4.4: The three sinograms presented in figure 4.3 reconstructed using the simple backprojection algorithm.

Simple backprojection (SBP) alone produces blurred images as demonstrated in figure 4.4. This can be easily understood when considering a single point source located at the origin shown in figure 4.5. SBP from the sinogram convolves $f(x, y)$ with a $1/r$ distribution leading to the blurred image [Eq 4.9].

$$f_{BP}(x, y) = \frac{1}{r} \star f(x, y) \tag{4.9}$$

4.3.4 Filtered Backprojection

Consider the two dimensional inverse Fourier transform of the distribution $F(v_x, v_y)$:

$$f(x, y) = \int_{-\infty}^{\infty} \int_{-\infty}^{\infty} F(v_x, v_y)\, e^{-j2\pi x v_x}\, e^{-j2\pi y v_y}\, dv_x\, dv_y \tag{4.10}$$

Using the Central Slice Theorem [Eq 4.6]:

$$f(x, y) = \int_0^{2\pi} d\theta \int_0^{\infty} v\, P(v, \theta)\, e^{-j2\pi v(x\cos\theta + y\sin\theta)}\, dv \tag{4.11}$$

$$f(x, y) = \int_0^{\pi} d\theta\, p'(x\cos\theta + y\sin\theta, \theta) \tag{4.12}$$

where

$$p'(t, \theta) = \int_{-\infty}^{\infty} \mid v \mid P(v, \theta)\, e^{-j2\pi v t}\, dv \tag{4.13}$$

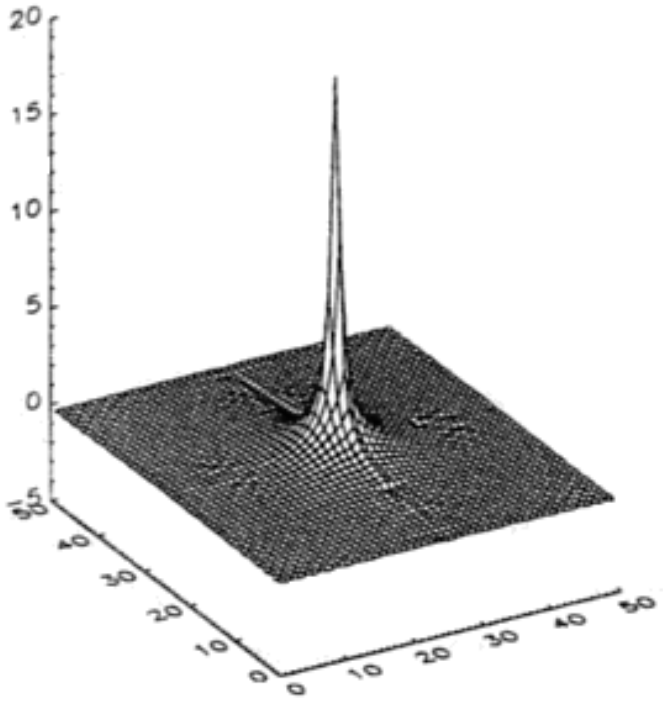

Figure 4.5: Two dimensional mesh of a backprojected point source with the $1/r$ blurring associated with simple backprojection.

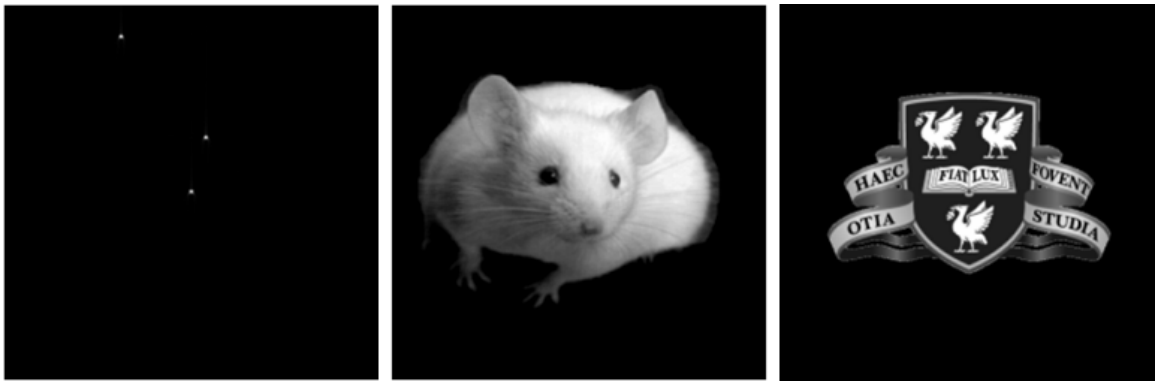

Figure 4.6: The three sinograms presented in figure 4.3 reconstructed using the filtered backprojection algorithm, applying a ramp filter in the frequency domain. The reconstructed images are almost undistinguishable from the initial images used to generate a sinogram.

The Filtered Backprojection (FBP) algorithm deconvolves the blurring associated with simple backprojection. This is achieved by multiplying the projection data in frequency space by a ramp filter $\mid v \mid$, before then applying the backprojection operator. Depending on the level of noise in the system an optional low-pass filter may also be applied. A 1D Fast Fourier Transform (FFT) is generally used to accelerate the process.

The drawbacks of FBP include the severe artifacts produced, especially in low statistics and LOR scans and the inability to model system effects. It still however remains a widely used technique largely due to its simplicity and computational speed which is an important consideration in clinical environments. However FBP remains a useful performance indicator, unlike statistical reconstruction where the quality of the system model between two scanners can play as an important a role as the actual physical characteristics of the systems.

The advantages of FBP over direct Fourier reconstruction are that the reconstruction stage can begin after a single projection has been measured. The Fourier method requires all projection data to be sampled before the calculation can commence. Sec-

ondly filtered backprojection like Fourier requires an interpolation method. The interpolation is carried out in the frequency domain in Fourier reconstruction while the backprojection stage of FBP applies an interpolation method in the space domain. Generally it is more accurate to carry out interpolation in the space domain than the frequency domain [Sta81]. Furthermore in most cases it is computationally faster to calculate a set of one dimensional Fourier transforms rather than a single two dimensional transform.

Figure 4.6 shows the three reconstructed images from the sinograms presented earlier in this chapter using the FBP algorithm and a ramp filter. The reader should note the sharpness of the reconstructed images after application of the filtered backprojection algorithm compared with that of the backprojection images presented previously in figure 4.4.

FBP filters

Mathematically the ramp filter is the ideal filter to apply to the projection data. In reality however measured data contains varying degrees of high frequency noise. A ramp filter strongly amplifies high frequency. In order to reduce the level of amplification a number of modified filters are often applied instead of the ramp filter. Most of these modified filters consist of the basic ramp filter multiplied by a second low-pass filter. Figure 4.7 shows the frequency response up to the Nyquist frequency v_{max}, of each of the different filters implemented for this work. The choice of filter is dependent on the level of noise in the system and typically would be selected empirically. The mathematical response of each filter is given in equations 4.14-4.18:

$$f_{ramp}(v) = \frac{\mid v \mid}{v_{max}} \tag{4.14}$$

$$f_{S.L}(v) = \frac{2}{\pi} \mid \sin\left(\frac{\pi \mid v \mid}{v_{max}}\right) \mid \tag{4.15}$$

$$f_{cos}(v) = f_{ramp} \times \cos\left(\frac{\pi \mid v \mid}{v_{max}}\right) \tag{4.16}$$

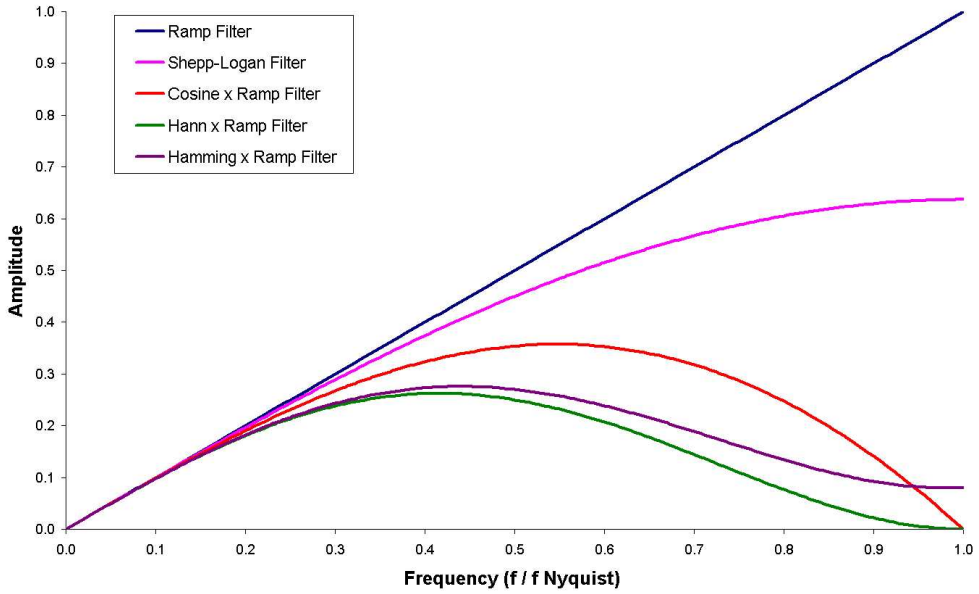

Figure 4.7: Filter response as a function of frequency up to the Nyquist frequency for the ramp, Shepp-Logan, cosine, Hann and Hamming filters.

$$f_{Hann}(v) = f_{ramp} \times \left(0.5 + 0.5\cos\left(\frac{2\pi \mid v \mid}{v_{max}}\right)\right) \tag{4.17}$$

$$f_{Ham}(v) = f_{ramp} \times \left(0.54 + 0.46\cos\left(\frac{2\pi \mid v \mid}{v_{max}}\right)\right) \tag{4.18}$$

4.3.5 FBP graphical interface software

Along with the development of the filtered backprojection algorithm itself an accompanying graphical interface was programmed as part of this work. The software implements the filters mentioned and several interpolation methods. It provides input/output options for a number of file formats including those associated with the data acquisition software used by the SmartPET project [MIDAS]. A complete guide to this software is presented in Appendix A.

4.4 Iterative reconstruction

Iterative algorithms approach image reconstruction from a different perspective than their Fourier based counterparts. Firstly an initial estimate of the image is used to calculate the expected measured sinogram values for such an image. The initial estimate is typically a uniform distribution with each pixel equal to unity. The expected values are calculated using a forward projection technique. The expected values are compared to the actual measured values for each LOR and a correction factor is found. These correction values are backprojected into the image space for each pixel. After a single iteration (each pixel in the image has been updated) the resultant image is closer to representing the measured data that the previous iteration's image. The process is repeated for many iterations until the image convergence criteria are met or an empirically selected number of iterations have been completed.

Iterative methods tend to be more computationally expensive than it's analytical counterparts. This to a large degree limited their initial take-up in clinical systems, confining them mostly to the research arena. As computer power has increased and the potential advantages have been proven they have become more prevalent. All commercial PET systems now come packaged with iterative reconstruction algorithms [Tar03] typically ML-EM or the accelerated counterpart OS-EM which are outlined in the remainder of this chapter.

4.4.1 System matrix

The system matrix (SM) is a two dimensional matrix containing the probability a decay in a pixel i, is measured by a LOR j, for all possible pixel and LOR combinations. This probability matrix is used to calculate the expected count rate for each LOR by multiplying it with the underlying source intensity map.

A simple matrix containing only geometric and attenuation correction models produces a sparse system matrix a, as most elements will be zero. The matrix can either be pre-calculated and stored in memory or sections of the matrix can be calculated

on-the-fly when they are needed. This reduces storage requirements at the cost of some performance overhead.

In this study a sparse matrix (outlined in the next section) containing only the geometric considerations has been implemented. For SmartPET 2D image reconstruction the total amount of pixels and LORs for the system matrix method implemented is small enough to allow the whole matrix to be pre-calculated once and stored in system memory.

4.4.2 Initial forward projection based SM

The system matrix implemented for use in this work is based upon a forward projection calculation. A point at the centre of each pixel is forward projected at each measured projection angle θ. The detector element covering the projected position is given a probability of one to measure a decay from that pixel [Method A in figure 4.8]. All other parallel beam LORs at this projection angle are given a probability of zero for measuring decays from this pixel.

An extension of the method above which forward projects a circle of diameter equal to the pixel size rather than a point [Method B in figure 4.8] is also implemented. The probability is now based on the area of the circle within each tube of response. The extended model better incorporates the finite pixel size allowing the possibility of multiple adjacent parallel beam LORs measuring a decay from the same pixel. All system matrix calculations in this work are based on the extended method.

4.4.3 Maximum Likelihood Expectation Maximisation

The Maximum Likelihood Expectation Maximisation (ML-EM) algorithm is the most commonly used iterative algorithm in PET. ML-EM was first applied to PET studies by two groups at around the same time, Shepp and Vardi [She82] and Lange and Carsson [Lan84].

The ML-EM is derived by first considering that the collected counts in a projection bin (LOR) is a Poisson process. The measured number of counts m_i in bin i if the

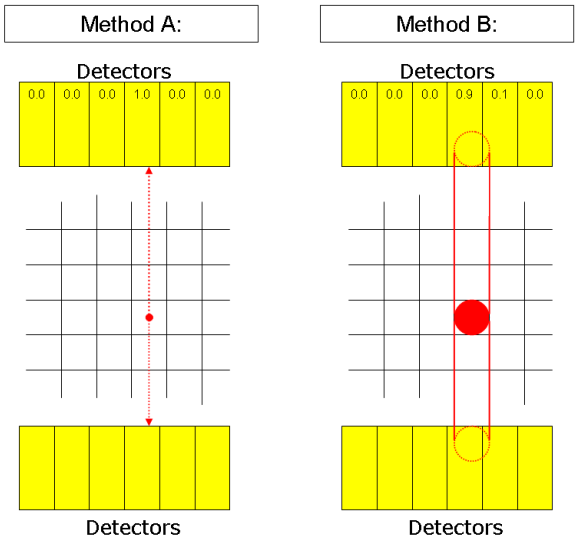

Figure 4.8: Two forward projection methods for calculating the probability a decay in a pixel is measured by the six displayed parallel beam LORs. The values shown in the top detectors indicate the probability of detection for that LOR.

mean is q_i is distributed according to the Poisson probability distribution:

$$Pr(m_i \mid q_i) = \frac{q_i^{m_i} \exp[-q_i]}{m_i!} \tag{4.19}$$

where $Pr(m_i \mid q_i)$ is the probability or likelihood of measuring m_i given the mean is q_i. By successive iterations ML-EM converges on the most likely image vector $\{n_j^k\}$ to have yielded the set of data $\{m_i\}$. The ML-EM equation 4.20 and 4.21 relates the value of a pixel in the next iteration to the current iteration value by multiplying with a correction factor. An attractive feature of the ML-EM equation is that if the initial estimate contains non-negative values then all subsequent iterations will also contain non negative pixel values. The ML-EM equation can be written as:

$$n_j^{k+1} = \frac{n_j^k}{\sum_{i=1}^{I} a_{ij}} \sum_{i=1}^{I} a_{ij} \frac{m_i}{q_i^k} \tag{4.20}$$

where

$$q_i^k = \sum_{b=1}^{J} a_{ij}\, n_b^k \tag{4.21}$$

n_j^k is the value of the pixel j after k iterations, a_{ij} is the probability of a decay in pixel j being detected in LOR i, m_i is the measured number of counts in LOR i and q_i is the expected number of counts in LOR i given an intensity distribution n. I is the number of pixels in the image and J is the total number of LORs in the scan.

Figure 4.9 displays the resultant images from the mouse sinogram data presented earlier for varying numbers of iterations. It can be seen from visual observation that initially the convergence rate between iterations is swift but later slows with increasing iterations. Analysis of the Peak Signal to Noise Ratio (PSNR) provides a numerical confirmation of this observation.

Peak Signal to Noise Ratio

A comparison of the PSNR [equation 4.22] between the reconstructed image K, and the base image I, as a function of iteration number shown in figure 4.10 nicely illustrates the convergence effect.

$$\text{PSNR} = 20 \log_{10} \left(\frac{255}{\sqrt{\text{MSE}}} \right) \tag{4.22}$$

where the Mean Square Error (MSE) is given by:

$$\text{MSE} = \frac{1}{MN} \sum_{i=0}^{M-1} \sum_{j=0}^{N-1} (I(i,j) - K(i,j))^2 \tag{4.23}$$

I, K are the two dimensional images being compared, M and N are the pixel size of these images in the two axis.

4.4.4 Ordered Subset Expectation Maximisation

To increase the convergence speed of the ML-EM algorithm and make it more feasible for clinical use an accelerated method was proposed by Hudson and Larkin in 1994 [Hud94] named Ordered Subset Expectation Maximisation (OS-EM).

OS-EM divides the measured data into S subsets or blocks [Equation 4.24]. Reconstruction from a single subset T_s of the data produces an image often referred

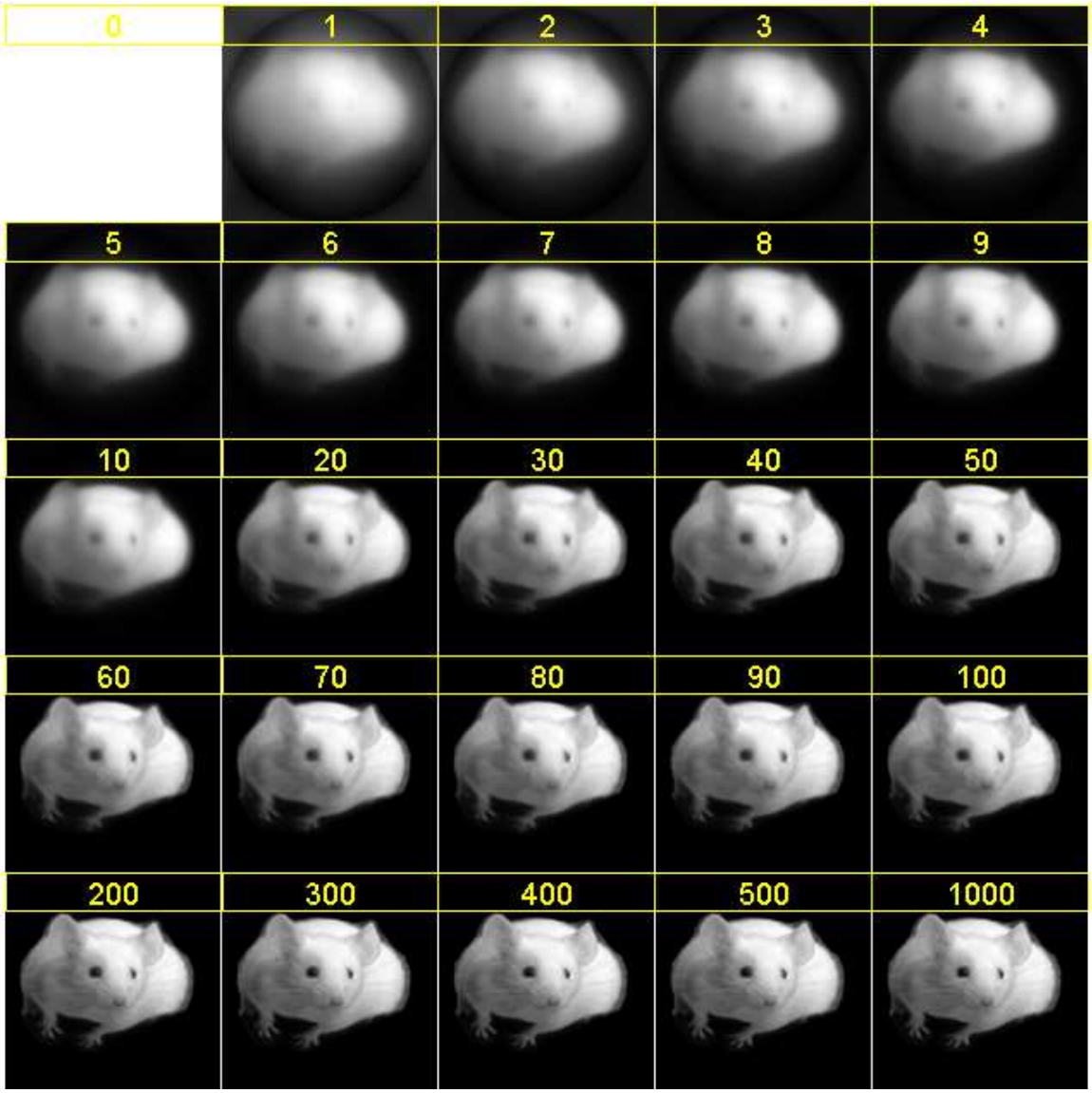

Figure 4.9: ML-EM reconstructed images after a varying number of iterations. The value above each image indicate the number of iterations required to reach that stage. The simulated data set size for these images is 128 detector elements, 128 projections with no induced noise. The image size is 128 pixels squared.

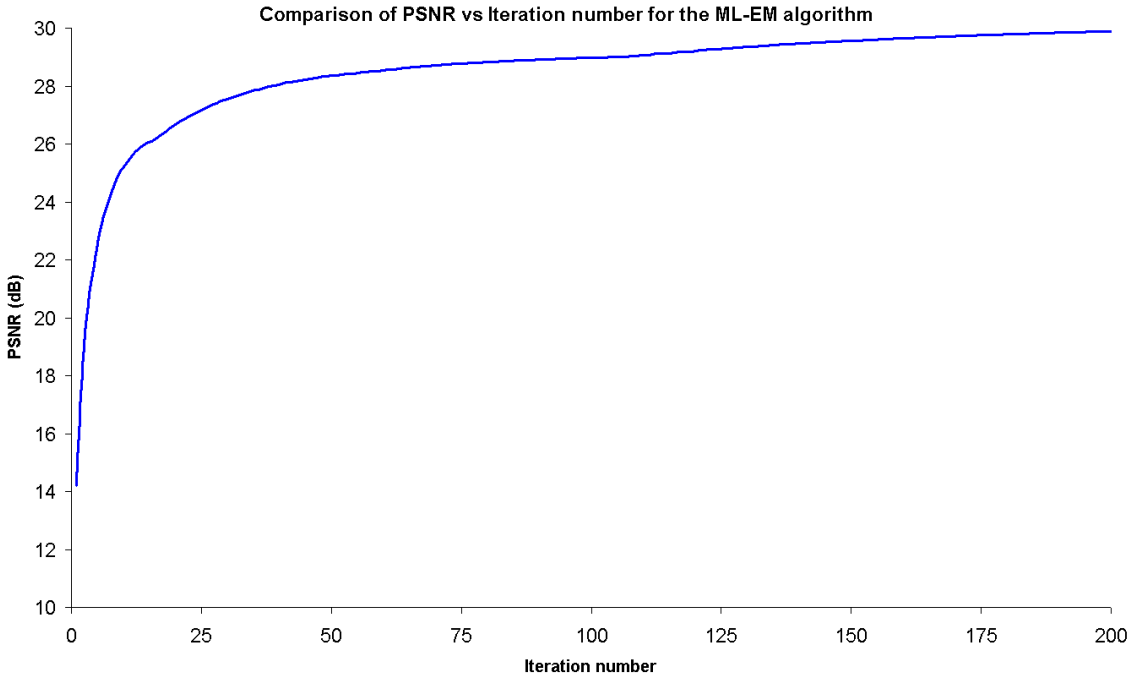

Figure 4.10: Peak Signal to Noise (PSNR) as a function of iteration number for the ML-EM algorithm based on the mouse sinogram data presented earlier. PSNR compares the image from each iteration with the base greyscale image used to produce the sinogram data.

to as a sub-iteration image. The next subset of data is used and the process is repeated until all subsets have been incorporated (numerically labelled $s = 1 \cdots S$). Looping over all subsets involves a similar number of mathematical operations and hence time as a single iteration of ML-EM. The later subsets act on the image matrix updated by the last sub-iteration rather than the last complete iteration, accelerating the convergence rate and producing a higher quality image for the same number of complete iterations. Figure 4.11 shows this effect using the simulated sinogram data, contrasting the quality of the reconstructed image over the first five iterations as a function of number of subsets.

$$n_j^{kS+s+1} = \frac{n_j^{kS+s}}{\sum_{i=1}^{l} a_{ij}} \sum_{i \epsilon T_s} a_{ij} \frac{m_i}{q_i^{kS+s}} \tag{4.24}$$

With optimisation of the number of subsets (level), the image produced after one complete iteration of all the sets is comparable to the resultant image from $N = S$ complete iterations of the ML-EM algorithm. Hence it can be seen as an acceleration of ML-EM by a factor equal to the number of subsets.

Mathematically the OS-EM does not guarantee convergence to a single solution but instead cycles between S unique solutions [Def03b]. In practise this is not a problem as iterative algorithms are rarely ran to convergence. Generally subsets include an equal number of equally spaced projections from the global set. A minimum of four projections is regarded as the limit required before reconstruction quality is degraded [Hud94] putting an upper limit on the number of subsets. Hudson and Larkin suggested a composite method where the number of subsets is reduced towards a single set as the image approaches convergence.

Reconstruction using one subset is equivalent to the ML-EM algorithm therefore ML-EM could in fact be viewed as a specialised case of the OS-EM algorithm.

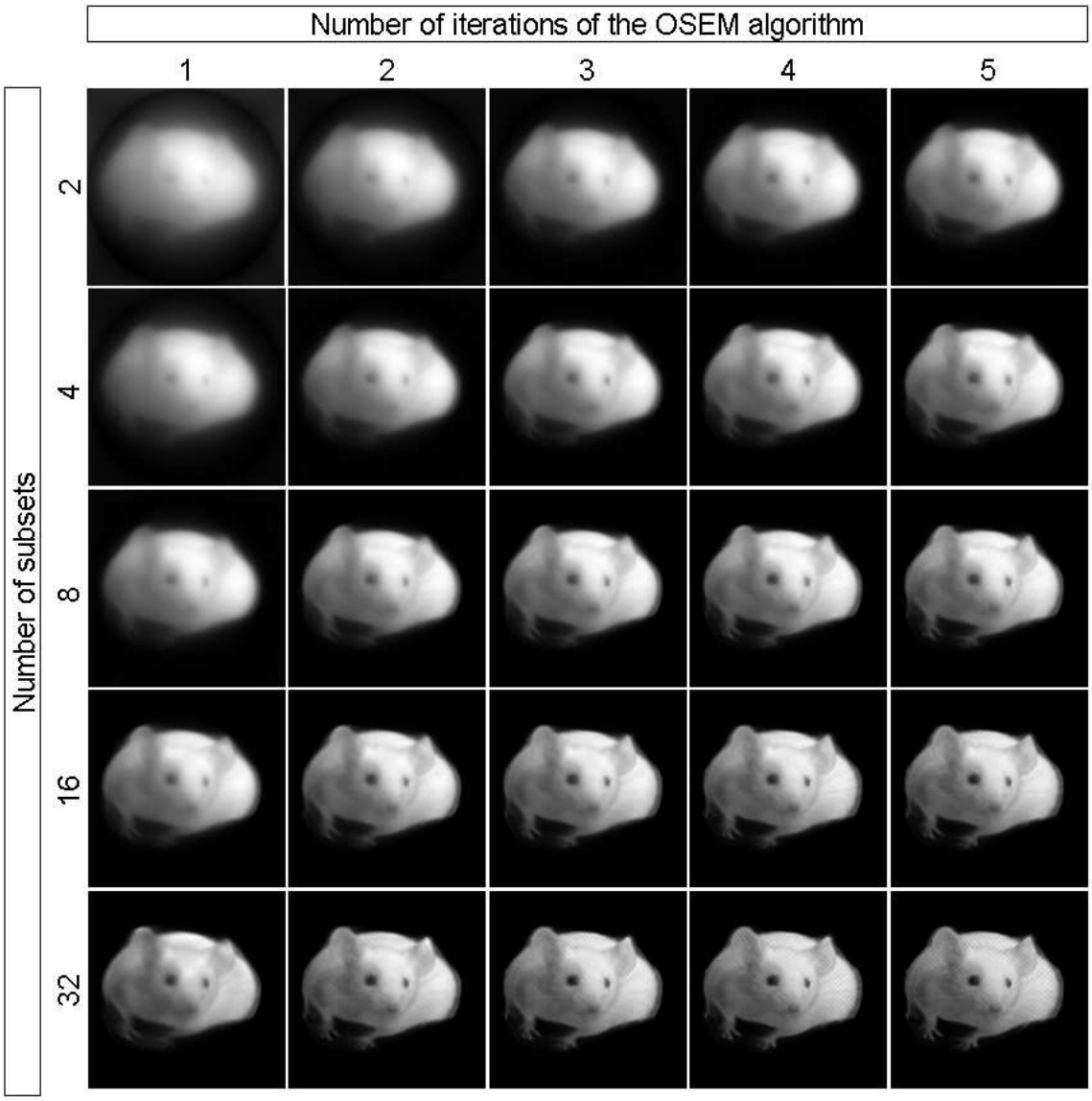

Figure 4.11: OS-EM reconstructed images during the first five iterations for varying numbers of subsets. The simulated data set has 128 projections with 128 detector elements. The images have been reconstructed on a 128x128 pixel grid.

4.5 Projection and detector element count considerations

To understand the influence the number of detector elements and projections has on the reconstructed images using FBP and ML-EM an investigation in which the two parameters are varied is presented. The sinograms were simulated with no noise induced from a 256x256 pixel base-image of the University of Liverpool crest.

4.5.1 FBP

The collection of images in figure 4.12 demonstrates how the reconstructed image quality varies from the FBP algorithm. The images have been reconstructed using the ramp filter with a Nyquist frequency cut-off and linear interpolation.

As the number of detector elements spanning the imaging space decreases so too does the resolving power. Only the largest structure, the area containing the crest itself being discernable with eight detector elements. Decreasing the number of projections with a large number of detector elements still enables the sharp edge detail to be observed but the artifacts from backprojection become increasingly prominent.

4.5.2 ML-EM

ML-EM handles limited numbers of projections more impressively than the analytical method with no induced streak artifacts in the background. With limited detector elements large ring artifacts are clearly seen. The algorithm appears to fit the data with smooth variation in the radial direction and discontinues in the azimuthal direction. This must be directly related to the large ratio between detector elements and projections, the artifacts are less pronounced as the ratio approaches unity. As with the FBP results for limited elements smaller details can not be resolved.

The resolving power is, as would logically be expected, related to the size of the detector elements and relatively independent of the algorithm used in the reconstruc-

tion. Increasing the number of detector elements per unit volume is far more beneficial than a similar factor increase in the number of projections.

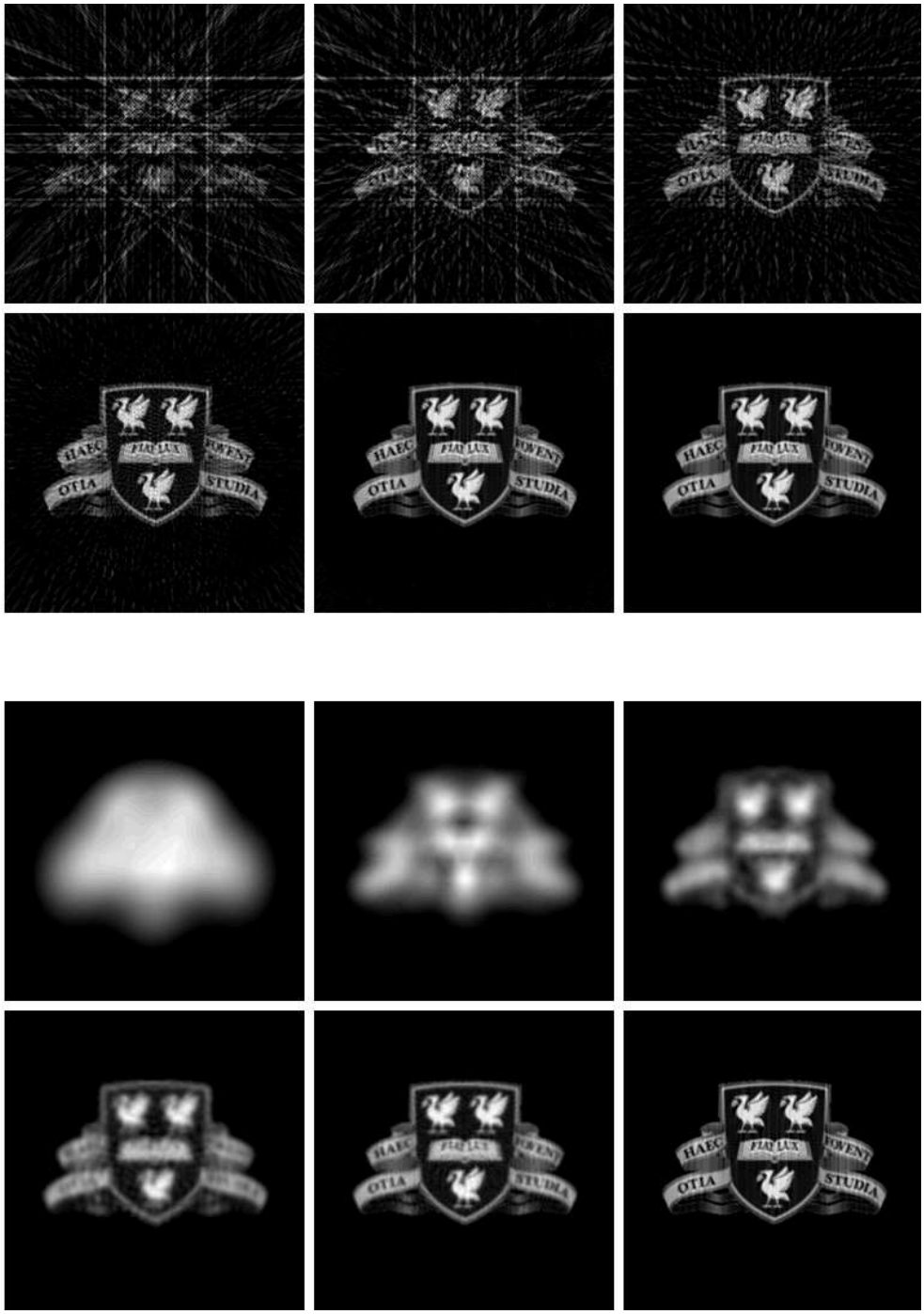

Figure 4.12: All images have been reconstructed using FBP with a ramp filter and linear interpolation. **Top six**: Images reconstructed from 256 detector elements and (left to right, top to bottom) 8, 16, 32, 64, 128 and 256 projections. **Bottom six**: Images reconstructed from 256 projections and (left to right, top to bottom) 8, 16, 32, 64, 128 and 256 detector elements.

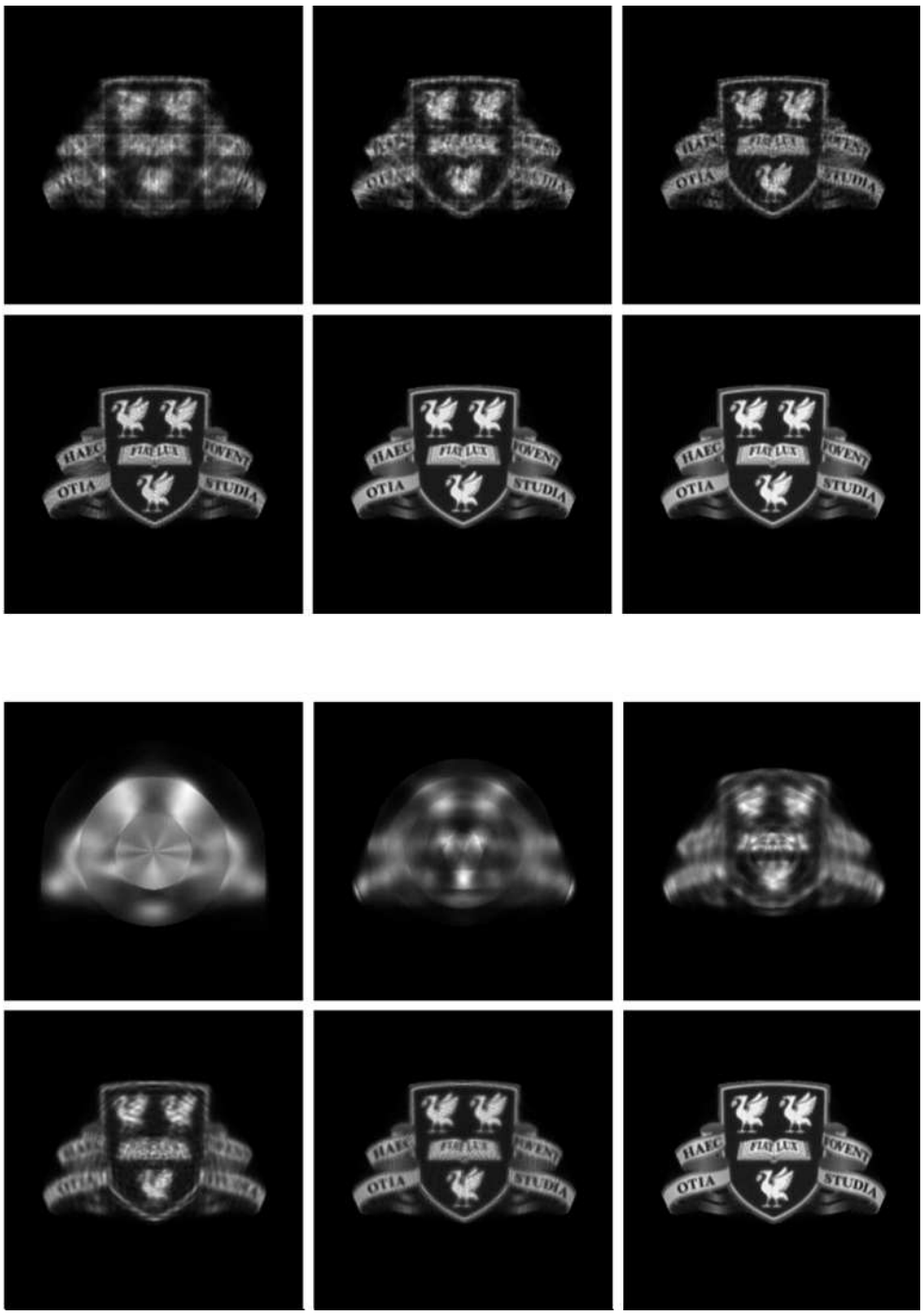

Figure 4.13: All images have been reconstructed using ML-EM with 100 iterations. **Top six**: Images reconstructed from 256 detector elements and (left to right, top to bottom) 8, 16, 32, 64, 128 and 256 projections. **Bottom six**: Images reconstructed from 256 projections and (left to right, top to bottom) 8, 16, 32, 64, 128 and 256 detector elements.

Chapter 5

Experimental procedure

5.1 Experimental setup

The following chapter provides an overview of the first PET imaging experiments performed with the SmartPET system between 11th October and 9th November 2005. Details about the detectors, acquisition system and experimental procedures are presented along with the operating performance of the two germanium detectors.

5.1.1 SmartPET detectors

The two detectors labelled SmartPET1 (SP1) and SmartPET2 (SP2) are orthogonal strip HPGe planar detectors manufactured by Ortec [figure 5.1]. The detectors each consist of a single 74 x 74mm crystal electrically segmented into 12 strips on both the AC and DC coupled faces, giving a total of 24 readout channels per detector. SP1 includes one further channel connected to the surrounding guard-ring but the channel is not utilised in this study. The active volume of the crystal is 60 x 60 x 20mm, giving a strip pitch of 5mm and an intrinsic spatial resolution of 5mm x 5mm x 20mm without the use of PSA [figure 5.2]. The AC coupled strips are $\sim$0.3μm thick separated by 180μm while the DC coupled contact is segmented with 50μm thick strips separated by 300μm . Fast charge sensitive preamplifiers with warm FETs

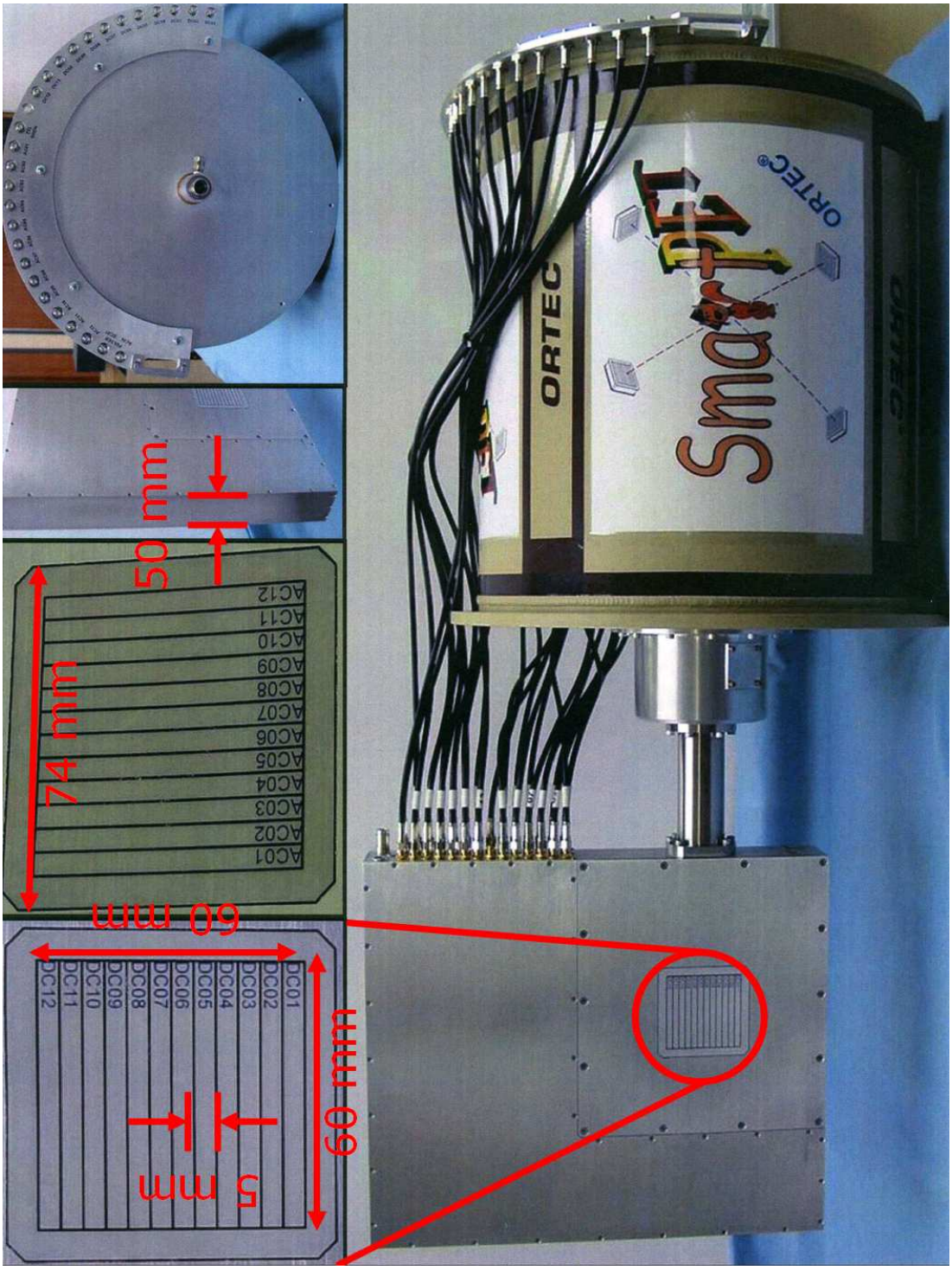

Figure 5.1: Photographs of the SmartPET1 detector along with annotated dimensions.

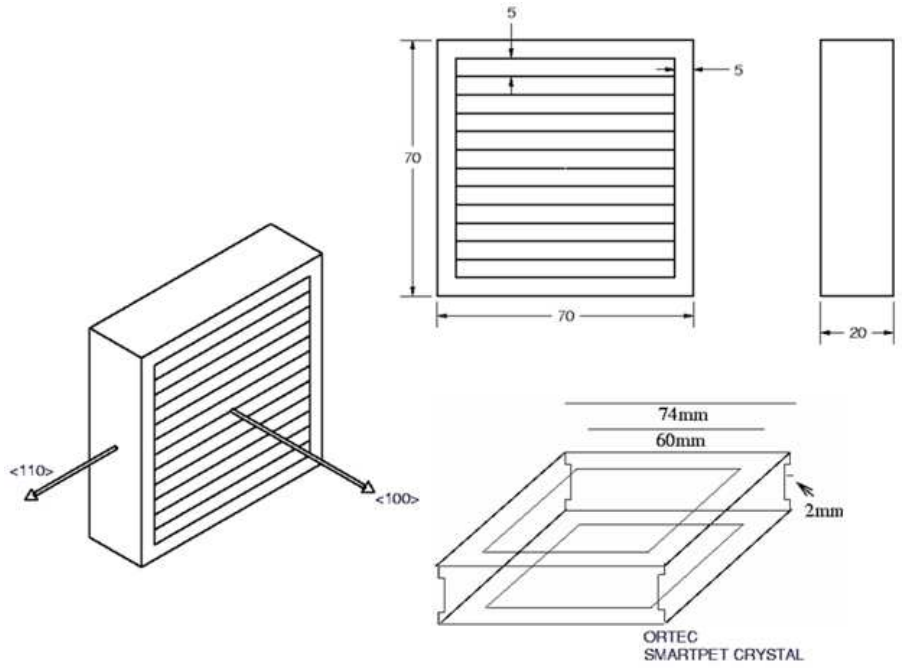

Figure 5.2: Schematic of the germanium crystal dimensions and lattice orientation.

are housed next to the crystal with the output cabling running to SMA connectors located on the back of the dewar. The dewars hold 12 litres of LN_2 which provides cooling for up to 72 hours. Details about the characterisation of the first detector can be found in the thesis of G. Turk [Tur06].

SmartPET1 DC11 channel

A known problem exists on the DC11 channel of the SmartPET1 detector. The defect which is believed to be due to a manufacturing error leads to charge sharing to the two adjacent strips, resulting in seemingly poor statistics for the strip. To reduce the impact of the strip the geometric arrangement of detectors and sources was selected such that DC11, which covers a slice along the rotation axis, is not important for the imaging of the sources.

5.1.2 Digital acquisition system

The experiments presented in this study utilised the GRT4 VME modules developed by CCLRC Daresbury [Laz03]. These cards digitise the charge pulses from the detectors resulting from photon interactions over a range of +/-1V using 14-bit, 80MHz FADCs. Each of these four-channel cards contains 2k of field programmable gate arrays (FPGAs) programmed with algorithms to time stamp the data and calculate photon energy using the moving window deconvolution (MWD) method [Geo93].

The electronics for the final SmartPET system are currently entering the testing phase. This compact PCI based system is a commercial solution provided by Lyrtech which combines several levels of FPGA and DSP processing designed to facilitate online PSA. This new acquisition system will operate using the total data readout (TDR) technique which requires no external hardware trigger.

Trigger

To simultaneously trigger all the GRT4 cards to record a digitised pulse from each channel a series of NIM units is used to supply an external hardware trigger. The twelve DC channel outputs from both detectors are connected to a Timing Filter Amplifier (TFA) and Constant-Fraction Discriminator (CFD) unit. A logic OR of the twelve signals from both detectors provided the two inputs to a logic AND gate which supplied the master trigger to the GRT4 cards. A Time-to-Amplitude Converter (TAC) unit provided means to sample the time difference between the two detector outputs triggering the system for each event.

5.1.3 Rotation system

The complete SmartPET system incorporates a custom built electronically controlled rotational frame shown in figure 5.3. At the time of the two experiments the stepper motors for the frame were not at a stage to allow their use in an experimental environment. Therefore an improvised system was devised in which the positron emitting

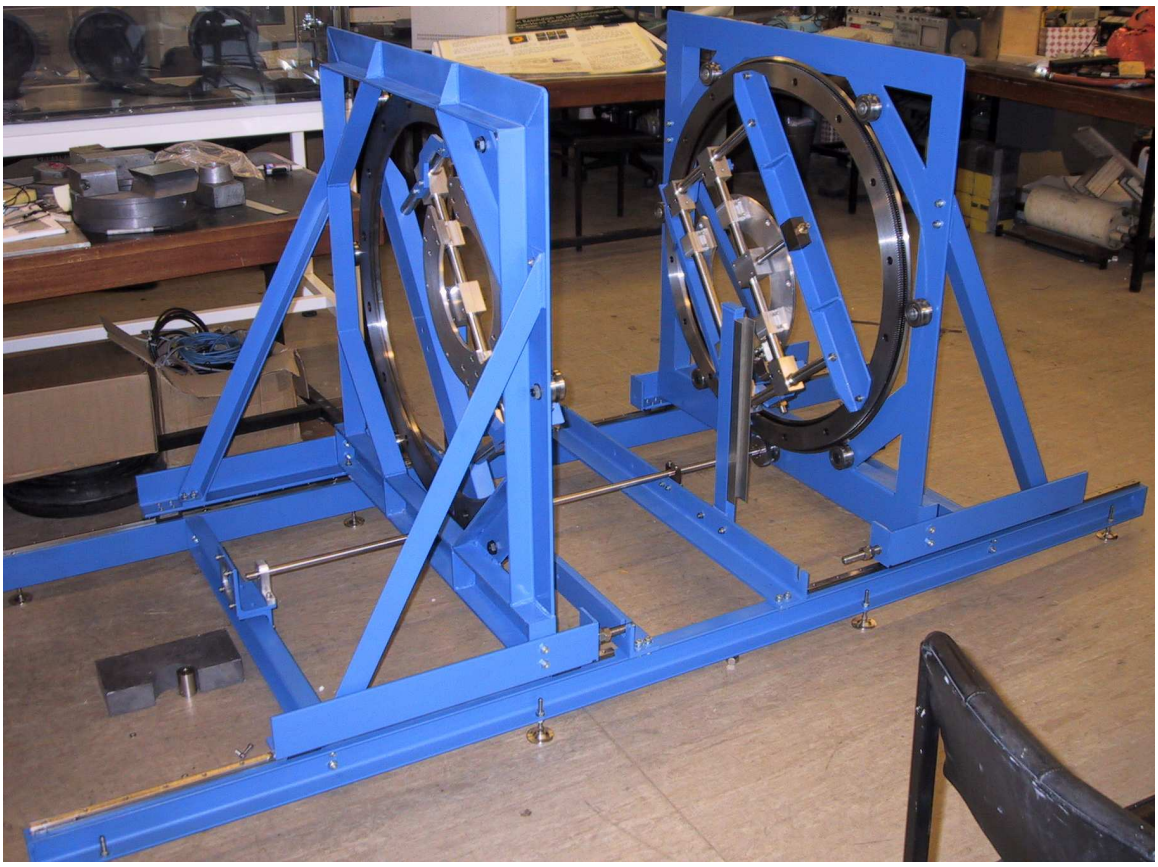

Figure 5.3: Picture of the automated rotational support frame designed for the Smart-PET system without the detectors or motors installed.

sources are fastened to a pole secured at both ends but allowed to rotate about its central axis. In this setup the pole and hence the sources are rotated as opposed to the detectors in the final system. The rotation of the pole was carried out manually with a systematic error estimated to be less than $\pm 0.5^o$.

5.2 Experimental details

The two SmartPET germanium detectors were positioned directly opposite each other in a planar PET system configuration with an inner face-to-face separation of 108mm [figure 5.4]. Due to the logistics of accommodating both detectors and their accompa-

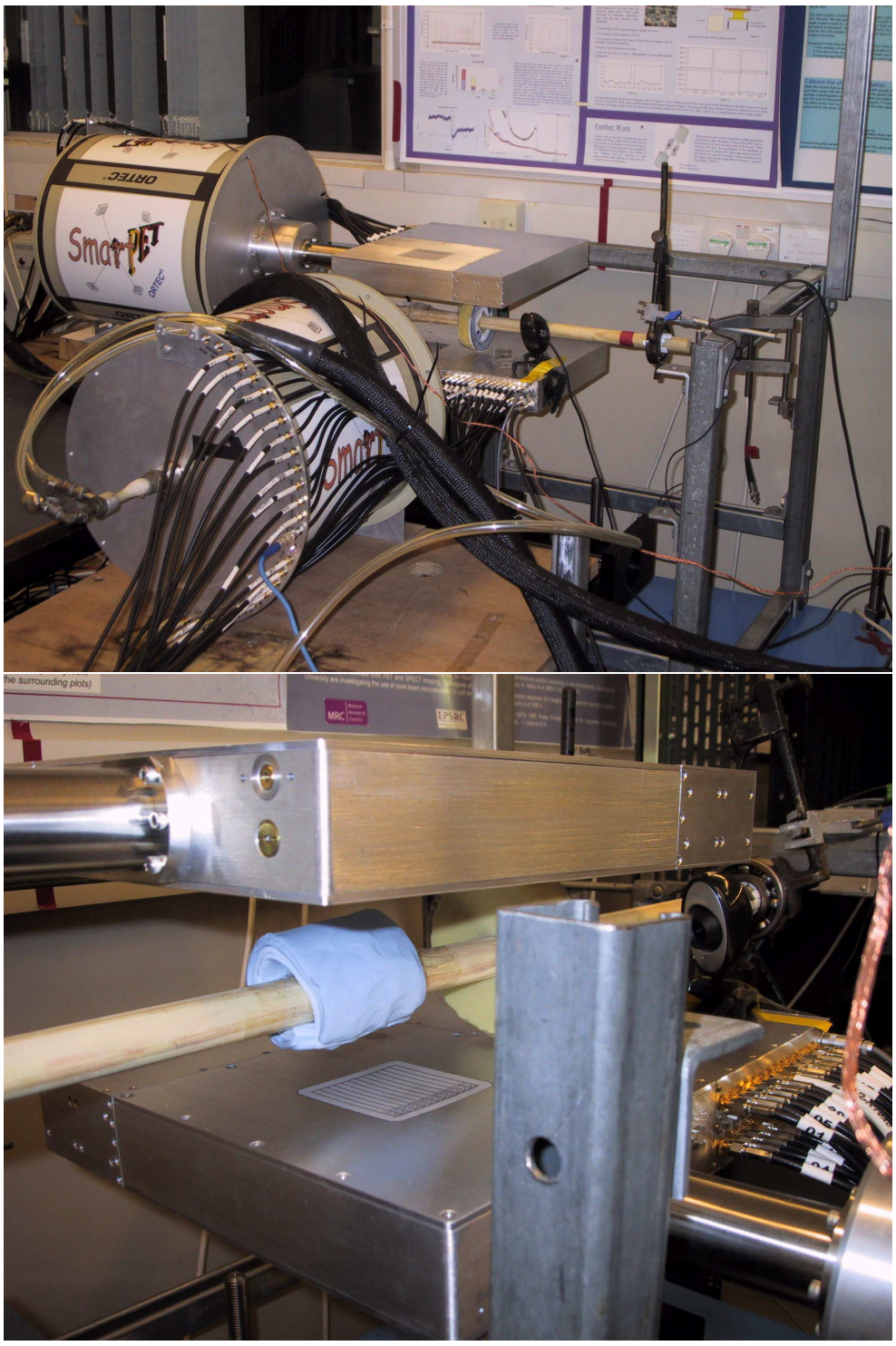

Figure 5.4: Photographs of the experimental setup. The lower picture shows the additional scatter material inserted between the detectors for the second experiment.

nying dewars within the lab, one detector was rotated 90^o with respect to the other. A pole secured at both ends but able to rotate was located centrally through the field of view of the germanium detectors.

Three ^{22}Na point sources were mounted securely onto the central axis at varying locations along the length of pole z, and different r,ϕ co-ordinates relative to the rotation axis. The three sources, labelled locally NSL329, NSL361 and NSL485 were known to have an activity of 2.5, 4.9 and 43.9 kBq at the time of the experiments. It was decided to locate the 2.5 and 4.9 sources within 5mm of each other towards the front of the field of view. The third source was positioned some 20-25mm further along the rotation axis to ensure the imaging of the two weaker sources was not compromised. Furthermore, the positioning of the third source ensured it would not be imaged by the DC11 strip of SmartPET1, which as outlined earlier has a mechanical defect. Additional low density material was positioned between the rotation pole and source to vary the radius from the rotation axis for each source.

Two separate experiments were conducted, firstly with the system setup as outlined above and secondly with a hollow cylindrical mass of scattering material (Blue Tak) between the sources and the detectors. The scattering material had an inner radius of 15mm and length 70mm. Whilst inserting the scatter material around the sources and rotation pole, care was taken to minimise any disturbance to their physical positions.

Both experiments collected data at 36 separate angles (projections) evenly spaced between 0 and 180^o with an angular separation of 5^o. Coincidence events were collected for 7 $\frac{1}{2}$ hours per projection, 270 hours total to ensure ample statistics. Due to limitations in the output data rate of the electronics used and also the weak strength of the sources in comparison with the source strengths often found in such experiments [Tai01] the much longer collection time per projection was required.

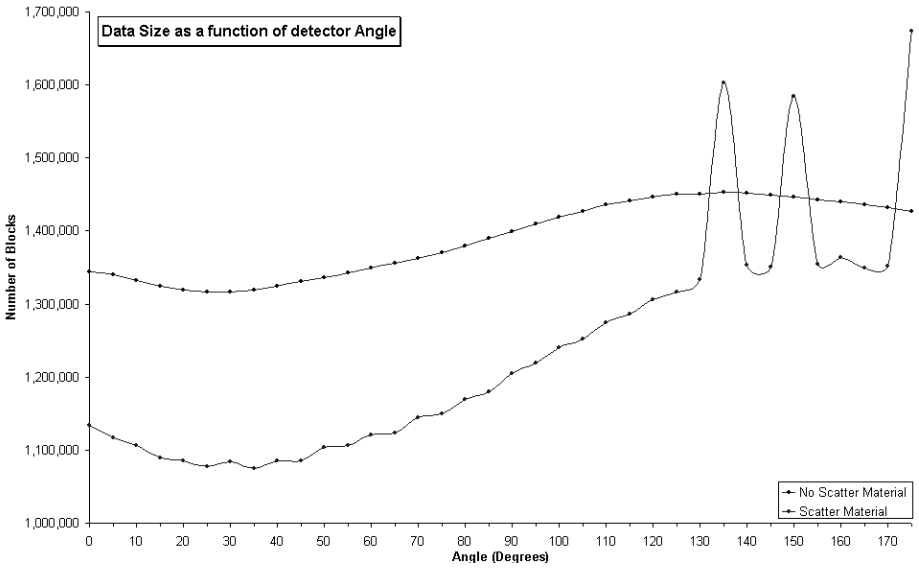

Figure 5.5: Data size / events as a function of angle. The anomalous peaks arise after a component failure required the removal of the TAC signal, increasing the available bandwidth for event processing.

5.3 Data collection and processing

In total ∼100 million coincidence events were recorded with no scattering material and ∼89 million with the scattering material introduced. Initially all 49 channels from the detectors were digitised and stored for each event producing a total data output of 3052 Mb and 2713 Mb for the no-scatter and scatter measurements respectively. This data was written to twelve SuperDLT tapes for each experiment. The data collection as a function of angle for both experiments, which is directly proportional to the number of events is shown in figure 5.5. The 20-30% increase seen in the scatter data at 135^o, 150^o and 175^o was the result of a change to the electronics system after a component failure required the TAC signal to be removed.

5.3.1 Geometric zero suppression

Reducing the data size collected during the experiments is vital to both decreasing the time required for later offline analysis and also reducing the tape and disc storage requirements to a more manageable level. To achieve this a technique called geometric based zero suppression is employed.

Geometric zero suppression involves examining the pulse shape from each channel and comparing the baseline difference at either end of the pulse. If this difference is greater than a specified lower limit ($\sim$10keV) the channel is labelled as having measured an energy depositing event and the pulse is flagged as one to be kept. As analysis carried out later in this work requires the ability to compare image charge in the two adjacent strips (or one in the case of an edge strip) either side of a real event these two strips are also flagged as useful. After analysing all channels in this way, any strip not marked as containing either real or image charge (or a convolution of the two) is removed from the re-output data stream.

Zero suppression reduces the data size to 760 and 656 Gb which is approximately 25% of the original size without any reduction in the number of events. The zero suppressed set of data was written to four SuperDLT tapes per experiment.

5.3.2 Event labelling convention

Both planar detectors have an AC and DC coupled face and for any given event these four faces will have an associated number of strips measuring an energy deposit. The number of strips measuring an energy deposit on any one face is sometimes referred to as the fold of that face and has a value ranging between zero and twelve in these detectors. Events can hence be grouped based on the four fold values with a labelling convention such as [1,2,2,1] where the four numbers correspond to [SP1 AC fold, SP1 DC fold, SP 2 AC fold, SP2 DC fold].

5.3.3 Single pixel event presort

For this preliminary study of imaging performance with the SmartPET system, only events which deposit energy in a single strip on each of the four faces will be considered for use in the image reconstruction algorithms, i.e. the [1,1,1,1] events. These events account for ~20% of the overall total number of events. The rational behind the choice is related to the additional complexity of using events in which more than one strip fires. For such events methods must be employed to decide which of the strips contains the first interaction point. Furthermore PSA based position improvement techniques are complicated by such events, a scenario discussed in more detail during the next section.

The zero suppressed data was presorted into a third set of files containing only the [1,1,1,1] events with a total overall size of 110 Gb and 104 Gb for the two experiments. This represents just 3-4% of the original data size and was stored onto computer hard disc. It is from this subset of the data the imaging analysis presented in chapter 6 is based.

5.3.4 Beyond [1,1,1,1] event imaging

Future work will focus on increasing the types of events used in SmartPET image reconstruction to include higher order event types for example [2,1,2,1] or [2,2,2,2]. Table 5.1 contains the fraction of events falling into these categories showing the potential maximum gain in statistics by utilising the events which are likely to have been caused by the gamma-ray scattering between strips. Techniques need to be developed to decide which of the strips is believed to contain the first interaction, the important event for positron emission imaging.

Image Reconstruction (IR) based on sub-pixel detector resolution, as will be explained in chapter 6, relies on the analysis of the image charge area for the adjacent strips either side of the real charge. Hence use of events which include fold two or greater on a single detector face for sub-pixel IR includes an additional constraint based on the distance separating the real charge events. A scattering distance of

Event Type	No Scatter Material (%)	Scatter Material (%)
[1,1,1,1]	18.4	20.0
[2,2,2,2]	2.6	2.1
[3,3,3,3]	0.08	0.06
[1,1,1,1] to [2,2,2,2]	61.4	61.4

Table 5.1: Event type breakdown. Note : [1,1,1,1] to [2,2,2,2] refers to all combinations of event containing fold one or two on each face. Up to 3x more events could be utilised for imaging if higher order scattering folds are taken into account.

several strips is less probable than scatters into the adjacent strip, yet these are the more complex events to analysis with PSA due to potential signal convolution.

Three possible levels of event complexity exist, each requires a more advanced algorithm than the previous:

1. Real events separated by two or more strips can be utilised straight-forwardly as no convolution of nearest neighbour image charge takes place.

2. Real events separated by a single strip require methods to contend with the double image charge convolution in the middle strip.

3. Real events in adjacent strips require methods to contend with image and real charge convolution in the two pulses.

To evaluate the challenges ahead table 5.2 lists the relative fraction of events which include at least one two fold detector face and are separated by a given number of strips from the point source data.

5.3.5 Line-of-Response usage

The SmartPET system records coincidence events between all pixel combinations joining both detectors. This initial study however uses a subset of all the possible

Min. Strip Separation	Fraction of Events
2	0.05
1	0.12
0	1.00

Table 5.2: Fraction of events which include at least a single fold two component as a function of strip separation.

lines-of-response (LOR). The current imaging algorithms developed utilise the LORs between the directly opposite pixels in each detector i.e. the set of LORs which run perpendicular to the front face of the detectors. These LORs span the whole imaging space and are equally separated in both sinogram dimensions (r,θ) so additional interpolation is not required. As this set of LORs are parallel to the detectors depth axis knowledge of interaction depth is not required and which simplifies their usage in image reconstruction algorithms. This set of LORs is perfectly adequate to image from as it spans the entire field of view, assuming enough statistics are collected in each LOR. The statistical limitation is the reason algorithms exist which can utilise many more LORs and will be an area for future development required for the SmartPET project.

Although the SmartPET detectors are orthogonal strip detectors they effectively have an electrically segmented grid size of 12^2 or 144 pixels each measuring 5mm^2. Therefore potentially 144^2 or 20,736 LORs per projection. However using only the LORs outlined above reduces this value to 144 LORs per projection or 0.7% of the theoretically possible. As data was collected at 36 projections, a total of 5,184 LOR are used to produce the basic images shown in chapter 6. Table 5.3 outlines the numbers and fractions of events from the two experiments which ultimately end up contributing to the reconstructed images. The increase in imaging events when the scatter material is introduced is known to be related to the relative position of the sources relative to the parallel LORs. The conclusion can be made because the increase in events seen in the imaging case is not reproduced in either the total or

	No Scatter Material	Scatter Material
Total Events	100,026,762	88,905,498
Total [1,1,1,1]	18,003,597 (18%)	16,979,468 (19%)
Imaging [1,1,1,1]	72,299 (0.07%)	109,404 (0.12%)

Table 5.3: Fraction of events which are used by the image reconstruction algorithms for the two experiments.

total [1,1,1,1] values.

The discussion above is further complicated when PSA techniques are used to increase the granularity of the detector, reducing effective pixel size to around $1mm^3$. Even when ignoring depth of interaction, which can be calculated using PSA this still produces potentially 25x more LORs per projection.

5.4 Energy resolution

The typical energy resolution at 511keV for each strip of the two detectors are presented in table 5.4. The values have been measured from an ^{22}Na point source using the MWD algorithm applied to the digitised traces. The resolution of the 511keV photopeak is broadened as a result of the positron momentum upon annihilation, as can be seen in the plot of energy resolution as a function of incident gamma-ray energy shown in figure 5.6. Spectra collected during the imaging experiments for the twelve AC channels of SmartPET1 are displayed in figure 5.7.

5.5 Time resolution

A coincidence timing window of 100ns was set within the hardware trigger system's logic units, hence data readout triggered if both detectors observed a energy deposit

Channel	SmartPET1 Energy Resolution keV, %	SmartPET2 Energy Resolution keV, %
AC01	4.28 (0.84)	3.50 (0.68)
AC02	3.68 (0.72)	3.89 (0.76)
AC03	3.85 (0.75)	3.50 (0.68)
AC04	3.74 (0.73)	3.53 (0.69)
AC05	3.71 (0.73)	3.63 (0.71)
AC06	3.84 (0.75)	3.54 (0.69)
AC07	3.81 (0.75)	3.56 (0.70)
AC08	3.78 (0.74)	3.63 (0.71)
AC09	3.77 (0.74)	3.41 (0.68)
AC10	3.90 (0.76)	3.63 (0.71)
AC11	3.78 (0.74)	3.94 (0.77)
AC12	4.11 (0.80)	3.86 (0.76)
DC01	3.92 (0.77)	3.94 (0.77)
DC02	3.28 (0.64)	3.85 (0.75)
DC03	3.48 (0.68)	3.77 (0.74)
DC04	3.55 (0.69)	3.82 (0.75)
DC05	3.22 (0.63)	3.59 (0.70)
DC06	3.28 (0.64)	4.00 (0.78)
DC07	3.31 (0.65)	3.83 (0.75)
DC08	3.37 (0.66)	3.81 (0.75)
DC09	3.41 (0.67)	4.00 (0.78)
DC10	3.36 (0.66)	4.11 (0.80)
DC11	4.47 (0.87)	3.76 (0.74)
DC12	3.73 (0.73)	3.80 (0.74)

Table 5.4: Energy resolution measurements from the 12 AC and 12 DC channels at 511keV (^{22}Na source) for both SmartPET detectors using the digital acquisition electronics.

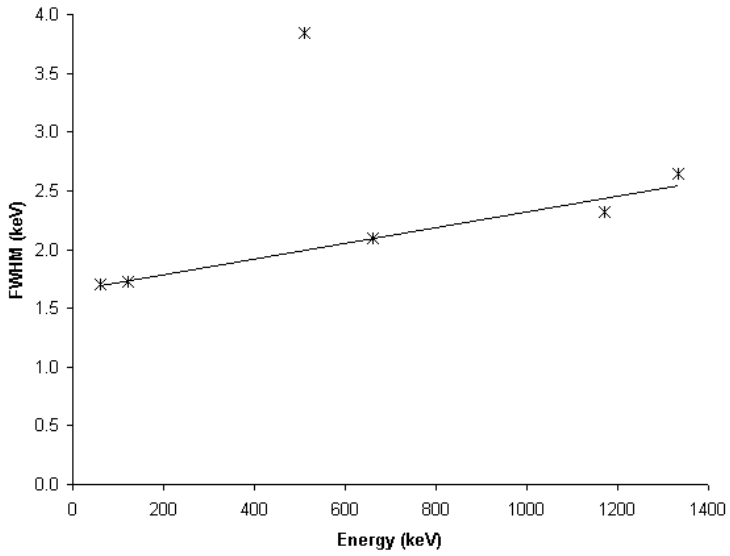

Figure 5.6: Energy resolution (ΔE) as function of energy (E) for the AC06 strip of SmartPET1. The performance at 511keV is hindered due to the additional influence of positron annihilation energy fluctuations.

with this coincidence window. Due to the weak source strength and hence low number of potential decays per second it was decided a relatively large window would improve statistics and limit the sensitivity due to the less than optimal timing resolution achieved with the system at the time of these experiments. With the strength of the sources used it can be calculated that there is a $\sim$2.3% probability of two independent decays occurring within the same 100ns interval. The rate of random coincidence is therefore expected to be insignificant for the two experiments performed as the probability is further reduced by the requirement of the system to measure two unrelated photons (one per detector) from the resultant four produced.

It is reasonable to assume the optimal timing resolution of the final SmartPET system will be in the region of 10-20ns and hence an order of magnitude smaller coincidence window will be implemented in the completed scanner. As the new electronics system being developed for the SmartPET system will not require an external hardware trigger setup and coincidence logic, the coincidence window will be implemented

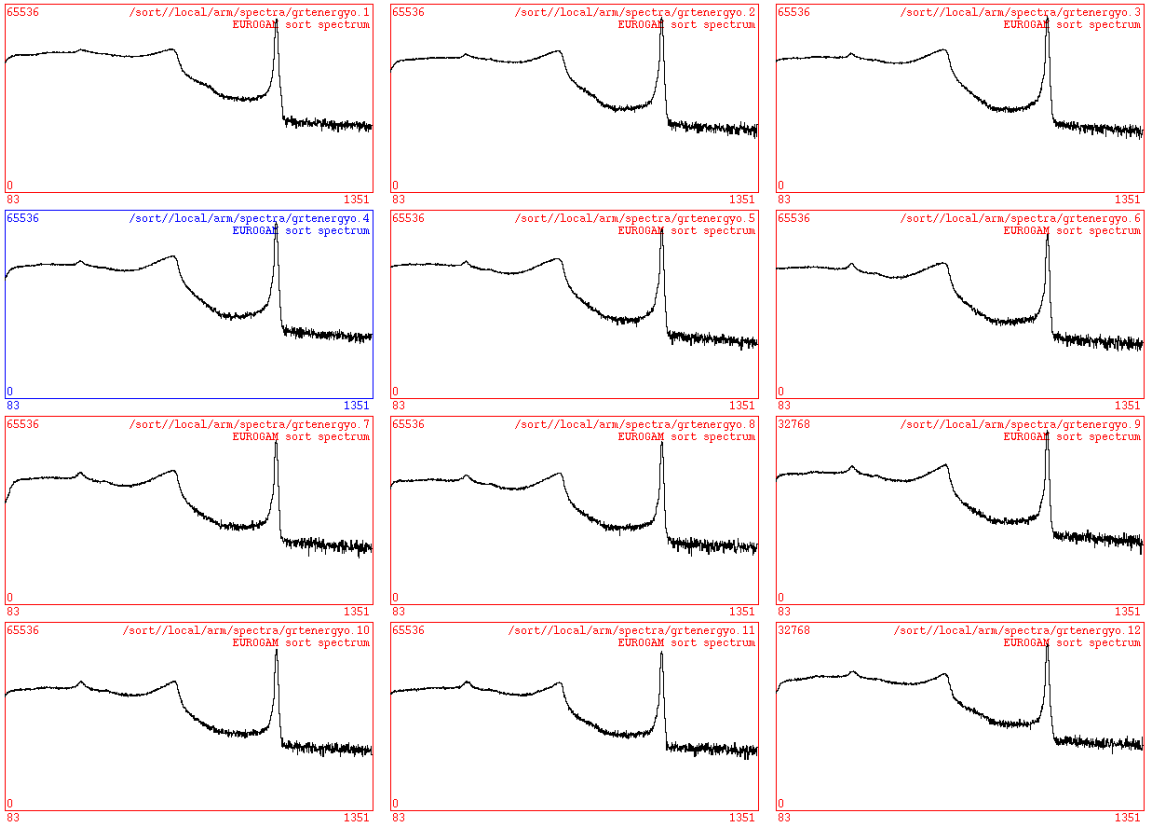

Figure 5.7: Experimental energy spectra from the 12 AC channels of the SmartPET1 detector showing the 511keV annihilation peak. The y-axis, containing the number of counts is plotted on a logarithmic scale.

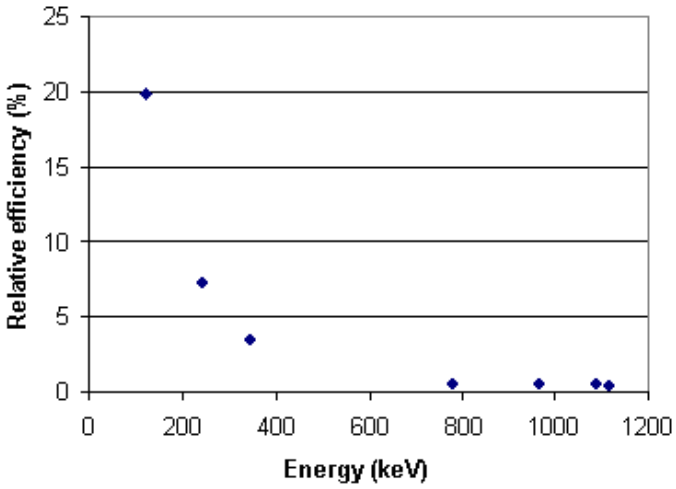

Figure 5.8: Relative efficiency as a function of incident gamma-ray energy for the AC06 channel of SmartPET1.

in software. This will allow greater control of the window width and investigations into its the effect on reconstructed image quality.

5.6 Detector efficiency

Relative efficiency measurements were performed for the AC06 channel of the SmartPET1 detector. A point source of ^{152}Eu was positioned 25.0cm from the front face of the detector and the relative efficiency of the detector investigated with an analogue electronics setup. The relative efficiency as a function of incident gamma-ray energy is presented in figure 5.8. Absolute efficiencies for this detector measured using a ^{133}Ba point source are presented in the thesis of G. Turk [Tur06].

5.6.1 Peak-to-Total

The fraction of events in which 511keV is deposited in both SmartPET detectors are presented in table 5.9. The values are consistent with peak-to-total (P/T) measurements made with the detectors individually, the product of both detectors P/T equals

	No Scatter Material			
Event Type	No Gate (%)	511 keV Gate	(Relative %)	P/T
[1,1,1,1]	18.38%	0.42%	5.21%	2.30%
[2,2,2,2]	2.60%	0.52%	6.39%	19.92%
[3,3,3,3]	0.08%	0.02%	0.27%	27.79%
[1,1,1,1] > [2,2,2,2]	61.42%	4.40%	54.19%	7.16%
			Overall P/T	**8.11%**
			Imaging P/T	**2.88%**

	Scatter Material			
Event Type	No Gate (%)	511 keV Gate	(Relative %)	P/T
[1,1,1,1]	19.99%	0.23%	6.60%	1.13%
[2,2,2,2]	2.13%	0.19%	5.66%	9.08%
[3,3,3,3]	0.06%	0.01%	0.22%	13.03%
[1,1,1,1] > [2,2,2,2]	61.37%	1.97%	57.64%	3.21%
			Overall P/T	**3.42%**
			Imaging P/T	**2.03%**

Figure 5.9: Table from each experiment detailing the fraction of events and peak to total percentage for each type of event. The first column indicates the type of event, while the second and third show the fraction of total events observed with and without an energy gate on the 511keV photopeak in each category. The fourth column (titled relative %) indicates the fraction of photopeak only events belonging to each event type. Finally the peak-to-total is presented for each event type along with the overall and imaging P/Ts.

the percentage of events measured during the imaging experiments depositing 511keV in *both* detectors. The overall P/T for all events of each experiment is 8.1% and 3.4% respectively, figures which indicate the effectiveness of the scattering material. The P/T for those events used to image (the [1,1,1,1] parallel beam LORs) is 2.9% for the non-scatter and 2.0% for the scatter material experiment.

5.7 System sensitivity

This chapter is concluded with a discussion on the sensitivity of the SmartPET system in terms of the number of detected events as a function of decays and in turn how this relates to the number of useful imaging events. From the combined source activity of 51.3 kBq and a beta decay branching ratio of 90%, a potential 46.2 thousand decays per second are available for detection. The system received ~400 trigger requests per second in coincidence mode or ~1% of the decays. Unfortunately limitations in the electronics data transfer rate resulted in only 100-120 of these triggers being recorded. Hence the system, with an improved electronics configuration would have measured ~3.5 times more events without change to the detector or source configuration. Conversely the results presented as part of this study could have been achieved with a 3.5 times short scan time if collected with the final SmartPET electronics, corresponding to 2 hours per projection. From the P/T values above it can be concluded that a photopeak count rate of 8Hz and 3Hz was achieved for the non-scatter and scatter experiments respectively.

Theoretically all of these events can be used for the task of imaging, although this study has two further imposed conditions. Firstly only fold [1,1,1,1] events are considered, reducing the available counts by a factor of ~5 [Section 5.3.3]. Secondly the LOR criteria of parallel only LORs being used within the reconstruction algorithms leads to a geometric suppression with just 0.7% of events expected to pass this second condition. The actual value is very dependent upon source positioning due to solid angle considerations. From the two values presented it would be estimated that one in a thousand of the recorded events are currently incorporated into the imaging algorithms, an estimation consistent with the figures presented in table 5.3.

Chapter 6

PET imaging analysis

6.1 Application of pulse shape analysis

In this work Pulse Shape Analysis (PSA) techniques are applied to the data sets in order to improve the spatial resolution of interaction positions within the detectors. Later in this chapter the success of the approach is investigated by reconstructing images with and without the use of PSA. First an overview of how image charge analysis is used in this study is presented together with results from a collimated source experiment to ascertain an independent level of confidence in the technique.

6.1.1 Image charge asymmetry

The image charge area for the two nearest neighbour strips to the collecting strip are measured for single strip firing events. From these two values the asymmetry parameter is calculated event-by-event with equation 3.10. All of the asymmetry values from the experiment are then histogramed for each strip across both detectors, giving forty-eight asymmetry distributions. Plots of the asymmetry distribution from the twelve SmartPET 1 DC channels after analysis of all [1,1,1,1] events are shown in figure 6.1. The plots show a fairly symetric distribution about the central zero value. Asymmetry values necessarily lie between the limits -1 and 1, the actual distributions

tail off at around (0.75).

To use the asymmetry distribution for each strip as a calibration of interaction position against asymmetry two assumptions are made. Firstly the asymmetry of the image charge area is directly related to the relative position of interaction. Values approaching the two limits -1 and 1 indicate interaction near to either edge of the strip while values around zero indicate interaction closer to the centre of the strip. Secondly it is assumed that if the strip were to be split into a number of equally sized smaller sub-strips the number of interactions occurring in each sub-strip during the entire experiment is approximately equal. The asymmetry distribution can therefore by divided into a given number of equal area sections which directly map to a similar number of hypothetical sub-strips in the detector. Simple analysis provides the positions of these section boundaries in the asymmetry distribution. These values can then be used in a second traverse of the experimental data, the gates allow the assignment of a sub-strip for every event on an event-by-event basis.

The number of sections to divide the strip and hence asymmetry distribution into is arbitrary, in this study two situations are presented. A three sub-strip split which indicates if the believed interaction was closer to the left, centre or right-hand side of the strip and corresponds to a sub-strip size of 1.67mm. The second is where a five sub-strip division is investigated with the rationale that this leads to a sub-strip size of 1.0mm. This is approaching the expected limit of spatial sensitivity achievable with current germanium detectors.

6.1.2 Validation using a collimated source

The technique outlined for improving spatial resolution will of course not identify the correct sub-strip for every event and it does not have any methodology for handling photons scattering multiple times within a single strip. In the case of imaging, correct identification of every event is not required due to the statistical nature of the problem. If the method correctly identifies the sub-strip in most events then potentially the images should be improved. Another attractive feature of the method is the high

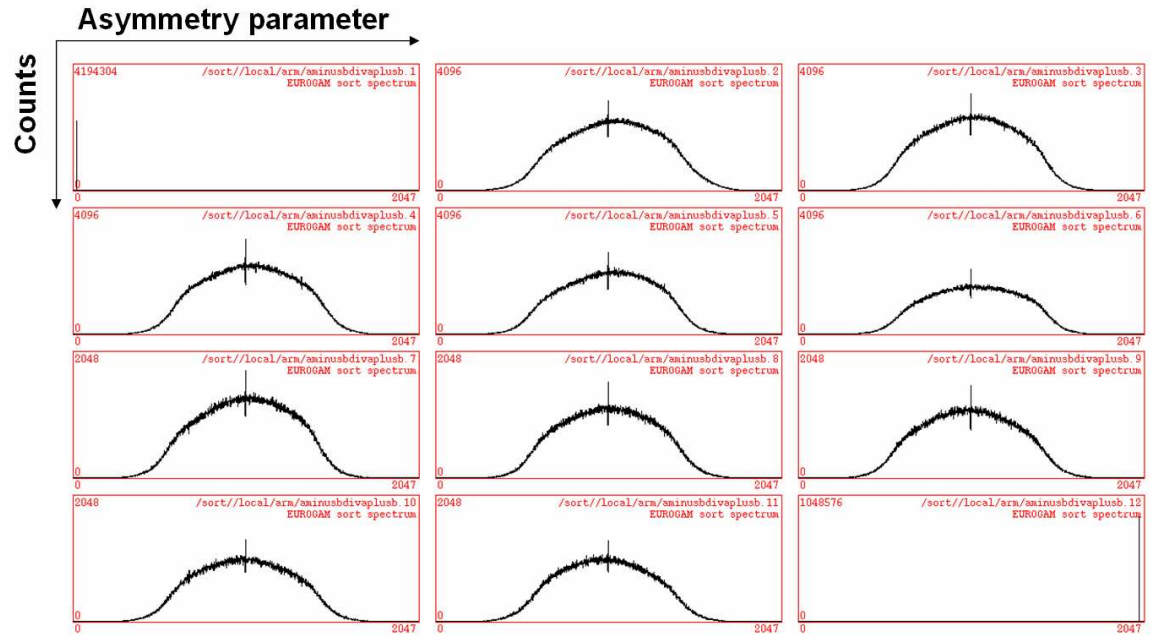

Figure 6.1: The asymmetry distribution histogram for each of the twelve strips on the DC face of SmartPET 1. Edge strips do not have two adjacent neighbours and hence the asymmetry distribution does not exist. The x-axis of each distribution runs from -1 to 1 but technical considerations with the analysis software lead to the re-scaling seen in the plots. The peak at the centre of the distribution occurs due to rounding issues related to small numbers very close to zero. The use of small image charge area values in the asymmetry formula can potentially produce large errors in the calculated asymmetry parameter, this is somewhat negated by the lower limit energy gate of 80keV applied to the data set.

likelihood incorrectly labelled events are placed (in the case of the five sub-section work) in a sub-strip either side of the correct position, limiting the error. It is a possibility that knowledge of the probability of incorrect sub-strip identification could later be incorporated into the system matrix of iterative imaging algorithms. This will decrease the blurring effect associated with such events.

Using a 1.0mm collimated source of ^{137}Cs (662keV) in conjunction with the x-y scanning table system at the University of Liverpool [Des02], validation of the PSA method was conducted by comparing the number of events labelled as being in each sub-strip as a function of scanning table position. As the collimated beam was stepped across the AC06 strip of SmartPET1 in five 1.0mm increments the histogramed asymmetry distributions are shown in figure 6.2.

The simple validation test indicates the image charge asymmetry technique is able to identify the correct 1.0mm sub-strip at least 50% of the time. Complications arising from the diameter of the collimatored beam incident on the detector. The possibility of gamma-rays traversing the lead and the alignment of the system suggest the true probability of correct identification is higher than this figure, which is sufficient for imaging applications. Over 78% of events are either identified correctly or have an error of one sub-strip. The long tails on the edge distributions lead to some loss of accuracy. The skew and hence long tails, most evident in the edge sub-pixel are related to the physical amount of germanium material to either side of the sub-strip. Events in the tales are believed to result from gammas scattering within, and across the strip. Future enhancements to the method should concentrate on improving this situation by identifying multiple single pixel interaction events. The collimated source experimental method for validating PSA techniques has some drawbacks (collimator size, source type), but it does provide a simple test and gives worst case estimates for the projected success of a technique. In the future Monte Carlo simulations which correctly model image charge shapes could provide a gold standard determination of PSA technique accuracy.

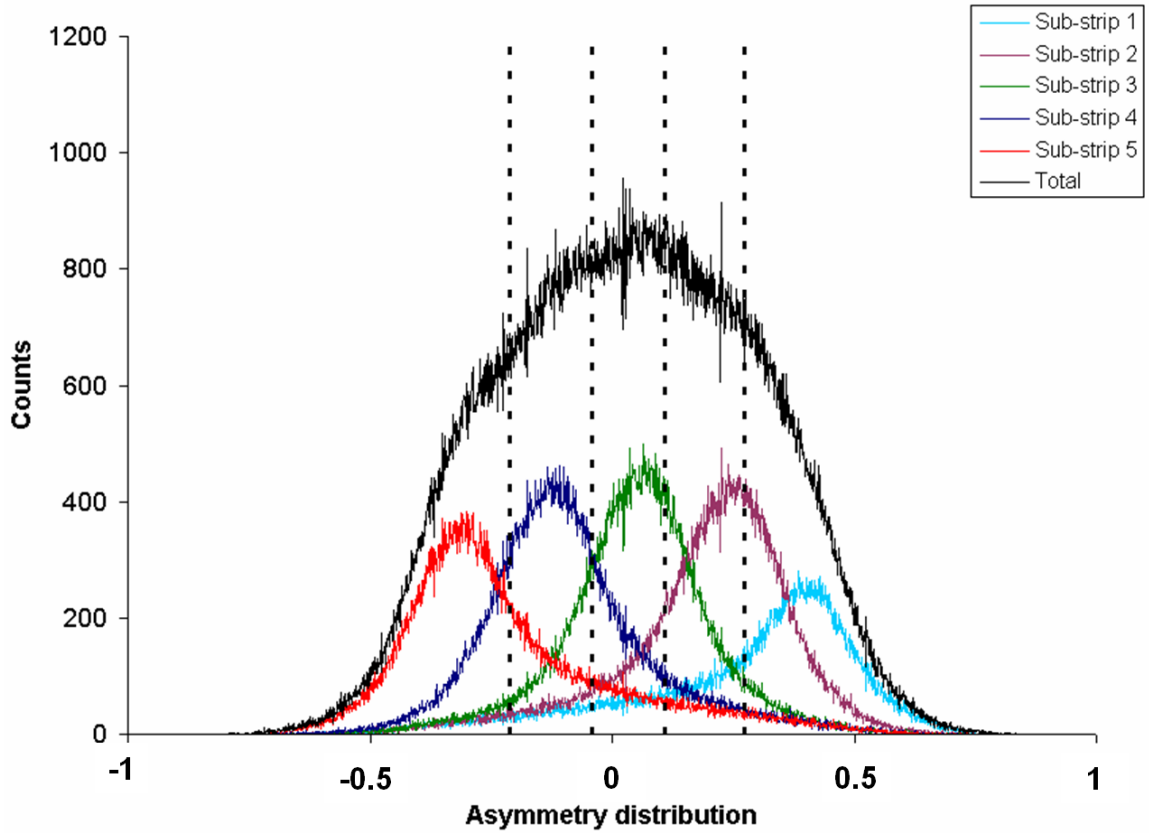

Figure 6.2: Asymmetry distributions as a function of scanning table position for five 1mm steps across AC06. The total asymmetry distributions is also shown and the locations of the four asymmetry gates (shown as broken vertical lines).

6.1.3 The edge strip limitation

A limitation of the PSA method is the requirement of a strip on either side of the interaction strip. The edge strips of each face therefore pose a problem. In this study the edge strips have not been used for PSA improved imaging. Research into a technique which would allow positional determination from a single image charge is an ongoing topic within the group. Recent analysis from collimated scan data [Coo06] has shown positive results but the method is yet to be applied to a PET data set and the output used for image reconstruction. The same method can also be applied to events in which more than one strip measures an energy deposit and due to the proximity of the strips both image charges are not available because of convolution complications.

6.2 Centre of rotation correction

Imaging algorithms typically assume the centre of rotation (COR) of a system corresponds to the mid-point along the face of both planar detectors, giving the maximum possible field of view. However this assumption can be incorrect due to misalignment errors, and COR correction offsets are needed to ensure optimal imaging. COR corrections for this study have been found empirically, by considering the resultant FBP images of a point source with filters and interpolation turned off. It is easy to see the effect of COR misalignment and correct for it as shown in figure 6.3. It was found COR offsets of 0.7mm and 1.6mm were needed for the non-scatter and scatter material experiments respectively. The difference in the two values hints at rotation axis displacement between the two experiments, an effect discussed further in the next section.

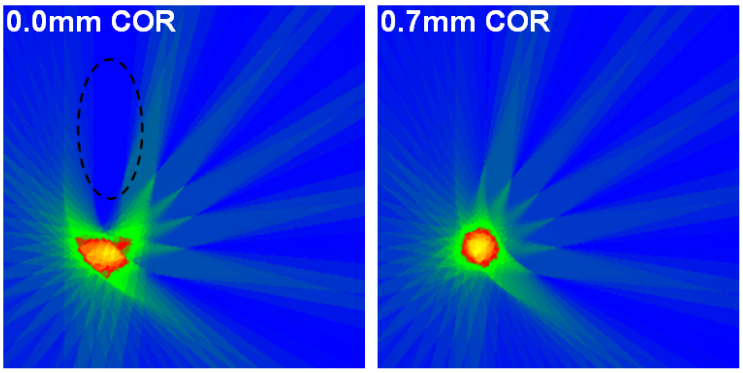

Figure 6.3: FBP images of a point source without (left) and with (right) a COR offset correction. FBP reconstruction with no applied filter and interpolation aid the identification and estimate of the COR offset, which can then be applied to all image reconstruction methods. The area within the dashed oval outline has zero background intensity and together with the arc like shape of the reconstructed point source is evidence of COR misalignment.

6.3 Sinograms

Sets of sinograms from the two imaging experiments are presented in the following section. A number of variables exist when considering the sinograms; the application of a photopeak energy gate, the use of PSA or the additional data points gained from the almost parallel nearest neighbour lines-of-response. Each of these variables has been treated in turn for both experiments to allow the reader to clearly identify the influence of each on the sinograms and later in this chapter the reconstructed images themselves.

The sinograms each cover a slice along the experimental rotation axis [figure 6.4] and the words slice and sinogram will be used interchangeably throughout this chapter. There are twelve sinograms and hence slices arising from the twelve strip segmentation, although this will be increased using the PSA methods mentioned previously. The horizontal axis of each sinogram contains the detector element, the t parameter

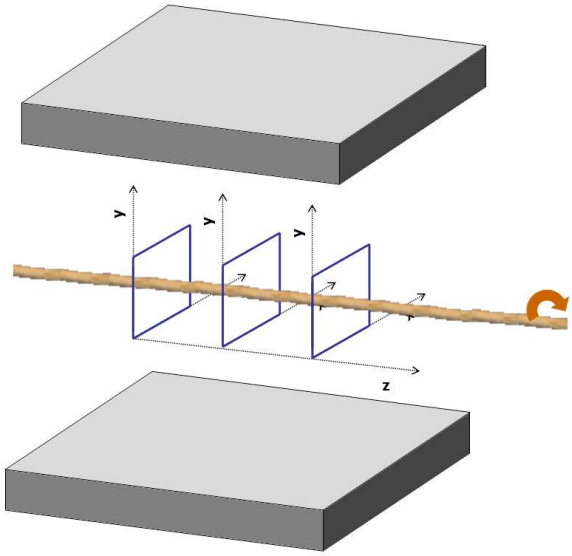

Figure 6.4: Schematic of the experimental setup detailing the orientation of the images and sinograms as slices along the rotation axis of the system.

refered to in figure 4.2. The vertical axis is the rotation angle of the system from 0 to 175^o.

Displaying the sinograms graphically does not always give a feel for the number of counts collected in each, especially as different colour scales are sometimes needed to portray the desired information. Therefore the integrated number of counts in each sinogram is displayed in the bottom right-hand corner.

6.3.1 Experiment 1 - No scatter material

The first set of sinograms presented in figure 6.5 are from the detector segmentation without the application of a photopeak energy gate. A maximum energy deposit per detector of 525keV is applied to limit the impact of the 1274keV gamma-ray emitted as part of the ^{22}Na beta decay.

As outlined in the generated sinograms [figure 4.3] a point source will follow a

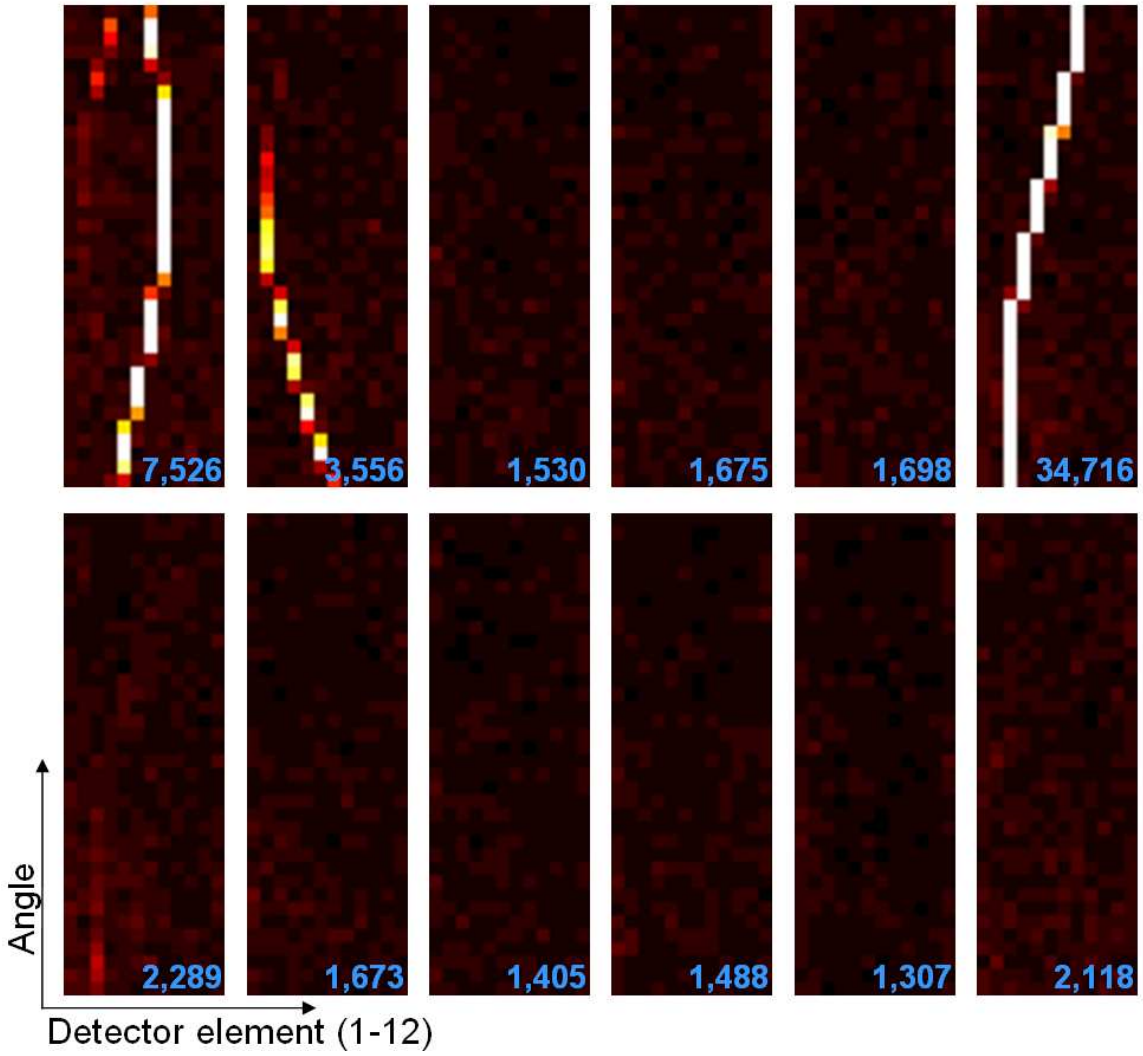

Figure 6.5: Twelve sinograms from the first imaging experiment using the SmartPET system. Top row (left to right): sinograms 1 to 6, Bottom row: sinograms 7-12. The sinograms are binned based on the 5x5x20mm detector segmentation with no applied photopeak energy gate. The three sources can be identified in slices 1,2 and 6. The values in the bottom right corner indicate the number of events in each sinogram slice.

sinusoidal path through the sinogram. From the twelve sinograms it can be seen from visual inspection that the three sources are located in separate slices, numbers 1,2 and 6. The motion of the sources through the sinograms may not appear sinusoidal due to limited sampling in the x-axis. The source in slice six is clearly the stronger of the three and this is in agreement with the known relative positioning of the sources prior to the experimental measurements, discussed in section 5.2.

Closer inspection of slice two reveals that this source appears to vanish at the higher y-axis values corresponding to the larger angles. In fact it can be seen faintly during the final angles in slice one alongside the source originally located in that slice. This strongly suggests a small perturbation of the systems rotation axis occurred at some point. The movement being large enough to cause the second source to relocate into the first slice while the other two sources remained in their respective positions. All three sources must have experienced the same magnitude translational motion therefore such a shift can be explained if the source which moved strip was located closer to a boundary than the others. Although the movement is not particularly welcomed and will have an impact on the image reconstruction is does demonstrate the systems sensitivity to small perturbations. Sinogram slice seven also appears to show a faint sensitivity to the source from the neighbouring slice six.

The counts in sinograms not containing a source are background events which have been assigned an incorrect LOR. These arise from the scattering of either photon before their detection, random coincidence events or the incorrect identification of the 1274keV gamma-ray as one of the two annihilation photons.

Photopeak energy gate

Applying a photopeak energy condition to the data of 511keV $\pm$ 10keV yields the sinograms presented in figure 6.6. Due to the relative activity of the three sources compared to the coincidence window width very few random events are expected to be counted. The removal of almost all the background counts when applying an energy gate strongly supports this conclusion. It suggests the vast majority of background

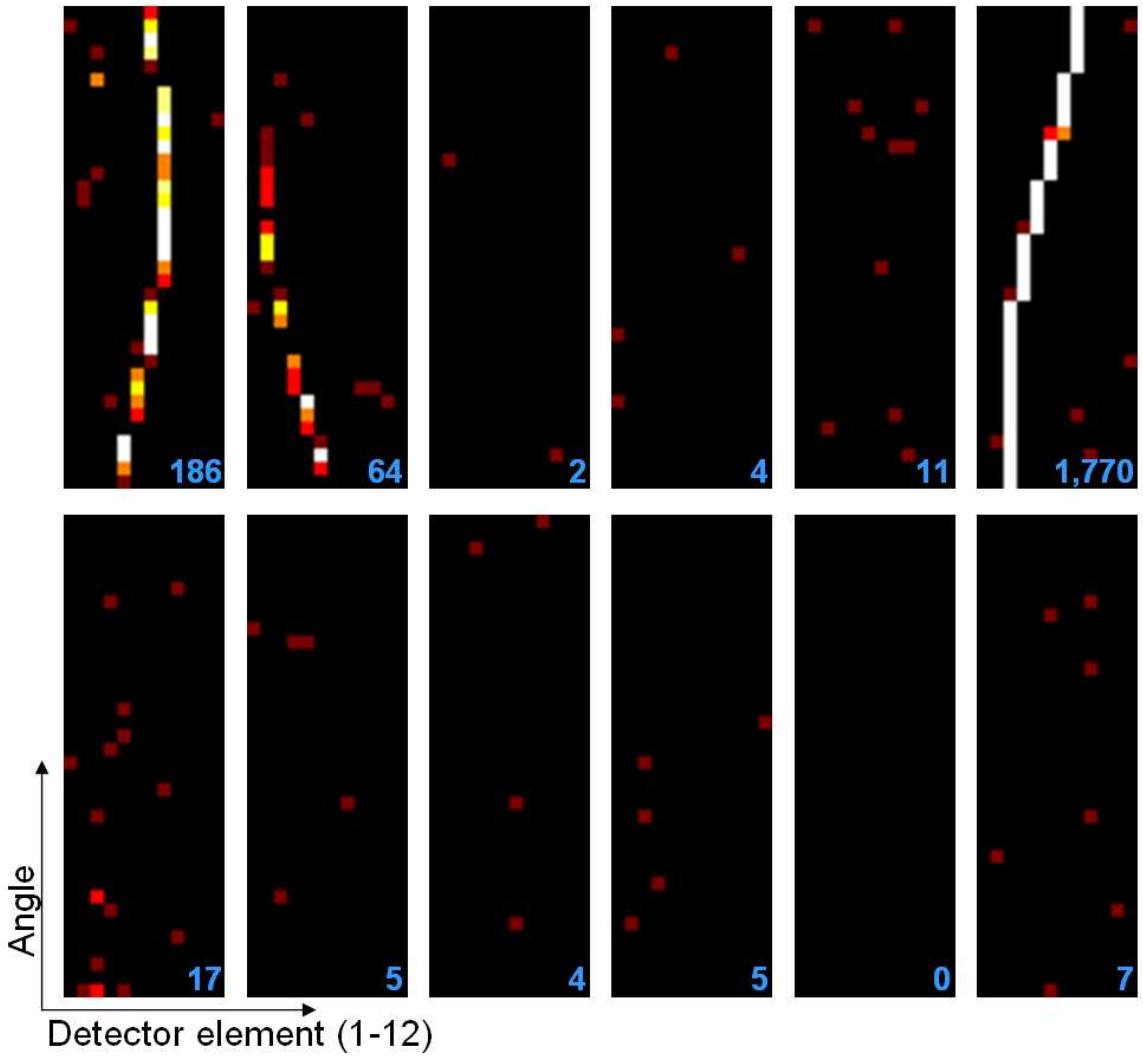

Figure 6.6: Sinograms shown in figure 6.5 reproduced with a photopeak energy gate. Only events depositing 511keV $\pm$ 10keV in both detectors are included reducing the statistics considerably. The background counts are almost completely removed from all the sinograms including those containing a source. The red squares indicate a single count within this plot.

counts in the original set of sinograms result from the scattering of one or more of the photons before reaching the detector or the incorrect identification of the 1274keV gamma-ray. The energy resolution of the germanium detectors allows the excellent discrimination of scatter and incorrect identification events but at a cost. A peak-to-total ratio of 2.9% severely limits the statistics in the sinograms. The affect of imaging from such limited statistics sinograms is presented in section 6.4.1.

The major problem with photopeak gating in this system is that many events which do not deposit full energy in the detectors but are good events for imaging are removed. This is due to the small finite thickness of the HPGe detector crystals. Events in which the photon(s) only scatter in the detector material and not the surrounding materials beforehand still form valid LOR for PET imaging. These events are very likely in a small scatter environment such as the experiments carried out as part of this thesis or typical small animal imaging which has a scatter fraction of between 5-30% [Yan06].

Additional almost parallel LOR

A technique to provide an additional, almost doubling of the number of elements in the x-axis used by some systems involves including almost parallel lines of response in the sinogram [Bai03]. Using the LORs connecting opposite-but-one detector elements and placing the extra data point equally spaced between the two parallel LORs gives an increase of $N-1$ samples. If the detector to detector distance is large compared to the detector element spacing these LORs can be considered parallel. The method is graphically illustrated in diagram 6.7.

The technique can be applied along the rotation axis direction too providing a similar increase in the number of slices and will be explored using the data from the second experiment. For the SmartPET system (when applied to the basic detector segmentation) the number of positions along the x-axis of each sinogram is increased to twenty-three. Figure 6.8 shows the resultant sinograms after the inclusion of these additional lines-of-response, the effect of imaging with the additional data points will

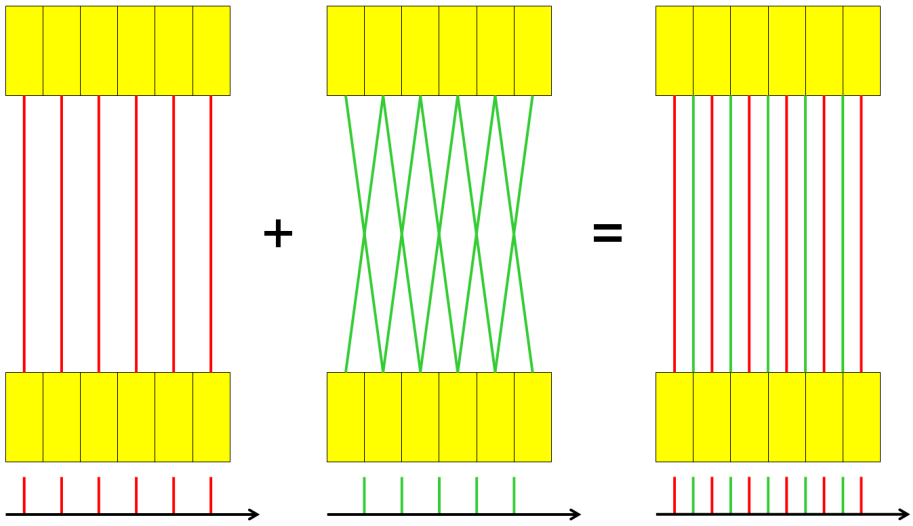

Figure 6.7: Combining the parallel LORs in the left sub-image with the nearest neighbour LORs (taken as the average of two LORs) from the centre image, assuming the additional LORs are parallel gives the sampling shown in the right sub-image.

be presented in section 6.4.1. The number of counts in background slices increases by a factor of two as would be expected, but the same does not hold true for the sinograms containing a source, which show an increase of 4,2 and 3 respectively. This can be explained by considering the solid angle each source makes with the detector elements defining LORs, some spatial locations will have a greater integrated solid angle coverage than others.

PSA improved spatial resolution

With the use of the pulse shape analysis the granularity of the detector can be improved by dividing the strips into small sub-strip regions. This in turn increases the number of detector elements and hence LOR in the sinograms. The effect of 3 and 5 sub-strips using PSA which corresponds to 1.67mm and 1.00mm detector spatial resolution is investigated. Sinograms for the strips containing a source (1,2 and 6) are displayed in figure 6.9.

The sinograms for 5.0mm, 1.67mm and 1.0mm are displayed horizontally with the

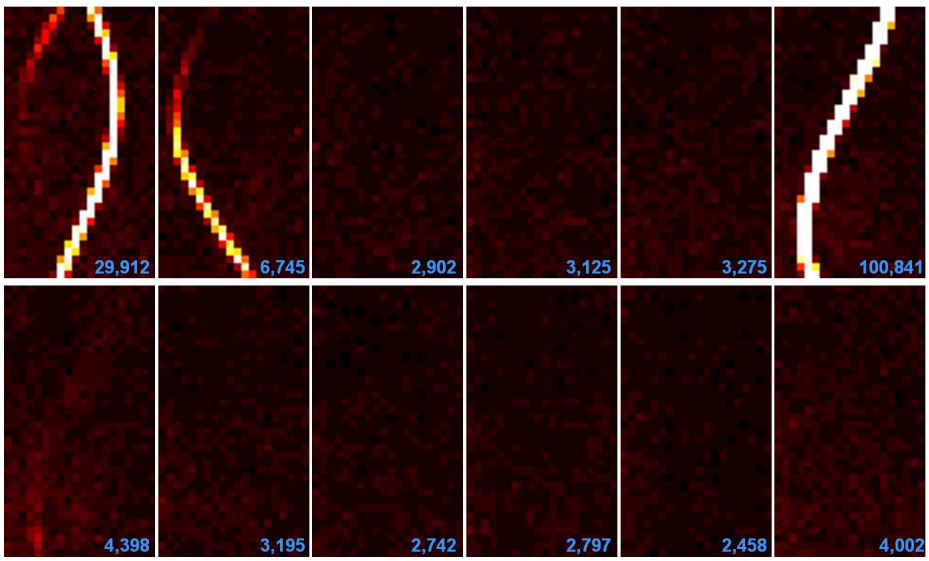

Figure 6.8: The additional sampling from using almost parallel LORs increases the number of statistics and appears to improve the quality of the sinograms with the source paths now looking more sinusoidal.

x-axis resized to aid comparison. If only parallel LORs are considered the number of statistics would be expected to fall by a factor of 3 and 5 for the PSA sinograms as only a 1/3 or 1/5 of the increased number of LORs will be parallel. Observation of the total counts in each sinogram shows this to be the case. It can also be seen that sinograms generated with PSA show a reduced FWHM across the bins sensitive to the sources. The shape of the sinogram is more discernable, the curvature in slice six over the first angles provides a good example. PSA allows features of the curve to be resolved which were not visible before its application, due to the width of each bin. Although the spatial improvement technique using PSA can in theory be extended beyond the 1mm division, however results beyond this level show no improvement in the sinograms. This is due to a number of reasons including the detector insensitivity, statistical uncertainties due to the reduction in counts (leading to decreased SNR) and the accuracy of the method when employed at the sub-millimetre level.

The improvement in the sinograms presented in figure 6.9 gives a high degree

of confidence in the PSA technique. It would therefore be expected to see superior imaging results from such sinograms when the reconstruction algorithms are applied.

6.3.2 Experiment 2 - Additional scatter material

As with the first experiment the initial set of sinograms presented in figure 6.10 are generated from the detectors electrical segmentation only with no photopeak energy gate. The slices containing sources are reproduced adjacent to the same slices from the first experiment for comparision in figure 6.11.

The sinograms from the second experiment show two of the sources are now located in slice one, consistent with the final angles from the first experiment. The other source is still located in slice six. The scatter material has increased the number of counts in the background sinograms by a factor of two.

Comparing the two experiments directly in figure 6.11 reveals that the sources have shifted in the negative x-axis direction as a result of the scatter material application. One of the sources in the first slice is seen in the left edge sinogram bin at some angles, which will cause complications later when applying the PSA position improvement method and will be discussed in more detail at that point.

Photopeak energy gate

When the sinograms are generated with a photopeak energy gate much the same response is seen as in the first experiment with almost all background counts being removed [figure 6.12]. This indicates the usefulness of an energy gate in the presence of a scattering material. The limited statistics will again provide a problem to the image reconstruction algorithms.

Additional almost parallel LOR

In the second experiment data set the additional almost parallel LOR technique has been extended. The method is used to now also provide an increase in the axial direction together with the sinogram x-axis presented in the first data set. Figure

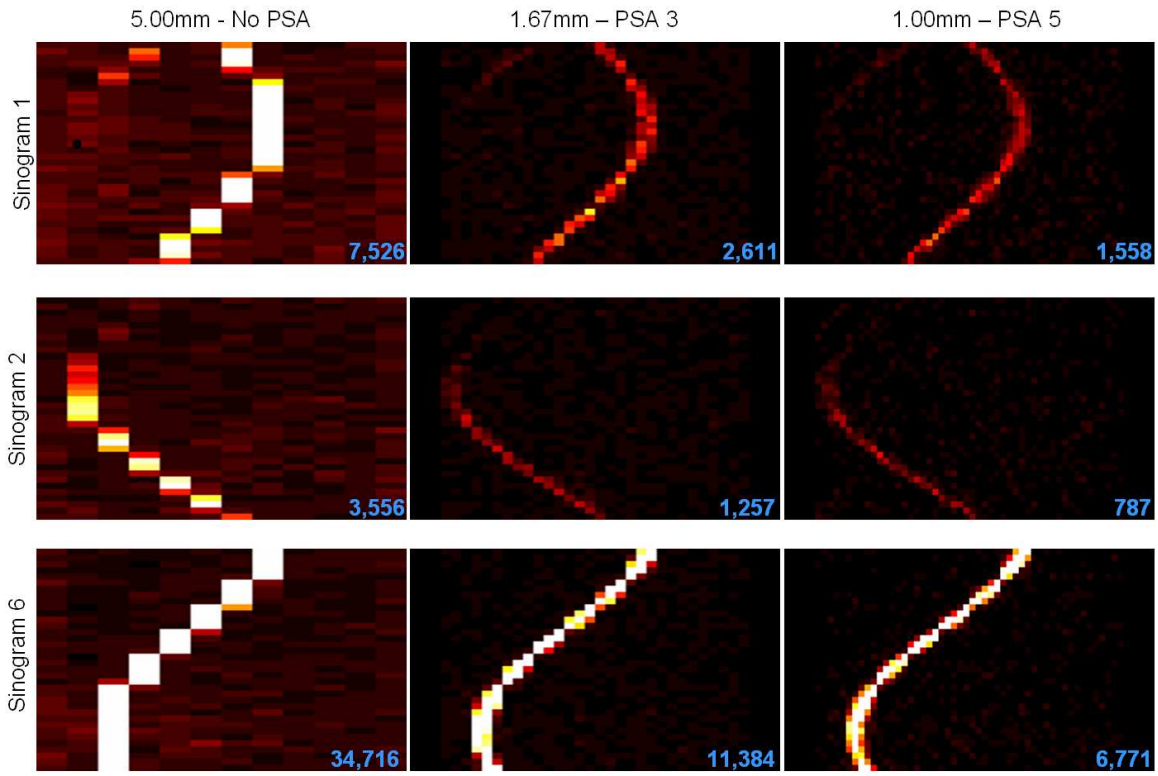

Figure 6.9: Comparison of the influence of PSA on sinograms containing sources from the first experiment. Each of the three sources is displayed on a horizontal line with three sinograms corresponding to no PSA, 3 and 5 division PSA. Due to large variations in counts across sinograms different colour scales are used and hence colour should not be used as a guide for judging statistics. Total counts in each sinogram are presented as a value in the bottom corner of the sinogram.

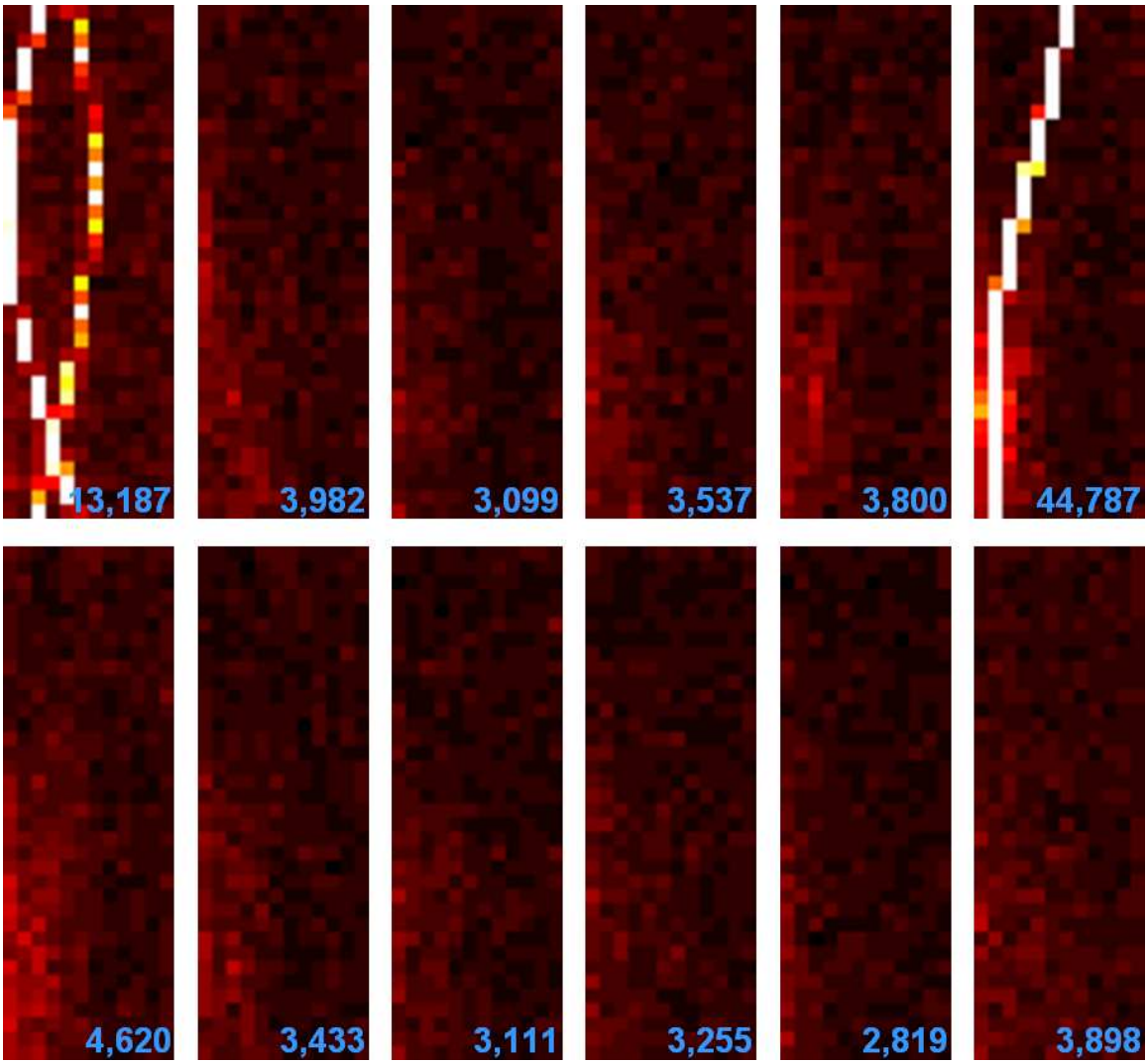

Figure 6.10: The initial set of sinograms from the second imaging experiment after the introduction of additional scatter material between the sources and detectors. The number of counts in background LORs is increased by a factor of two after the introduction of the scatter material.

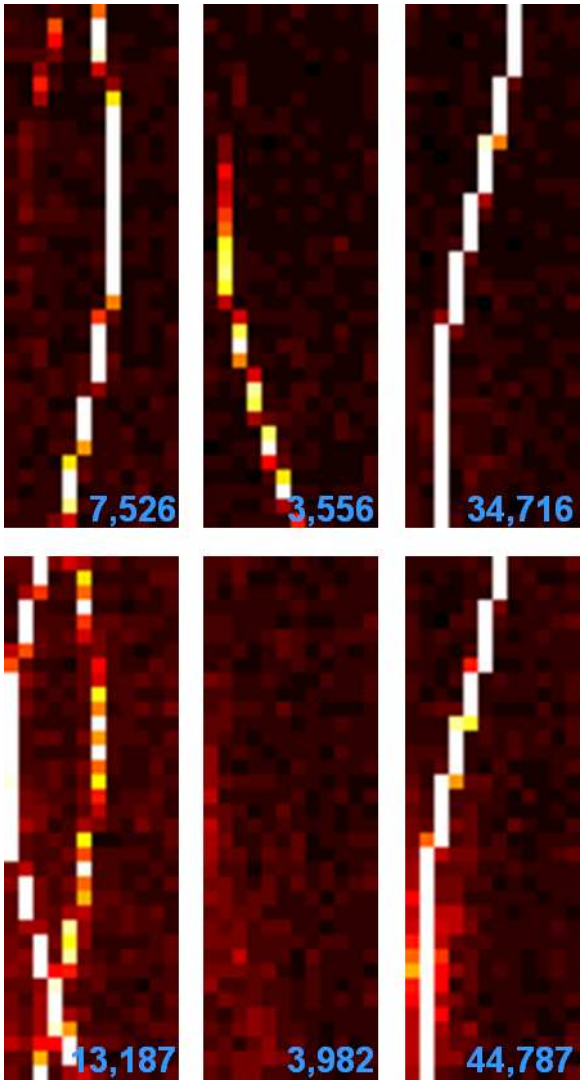

Figure 6.11: Comparison of the previously presented sinograms from the two experiments. The top row contains sinograms 1,2 and 6 from the first experiment (no scatter material) while the bottom row contains the same three sinograms from the second experiment (scatter material). Along with the noted movement of the source from slice two into slice one near the end of the first run, a shift in the negative x-axis of magnitude one pixel is seen.

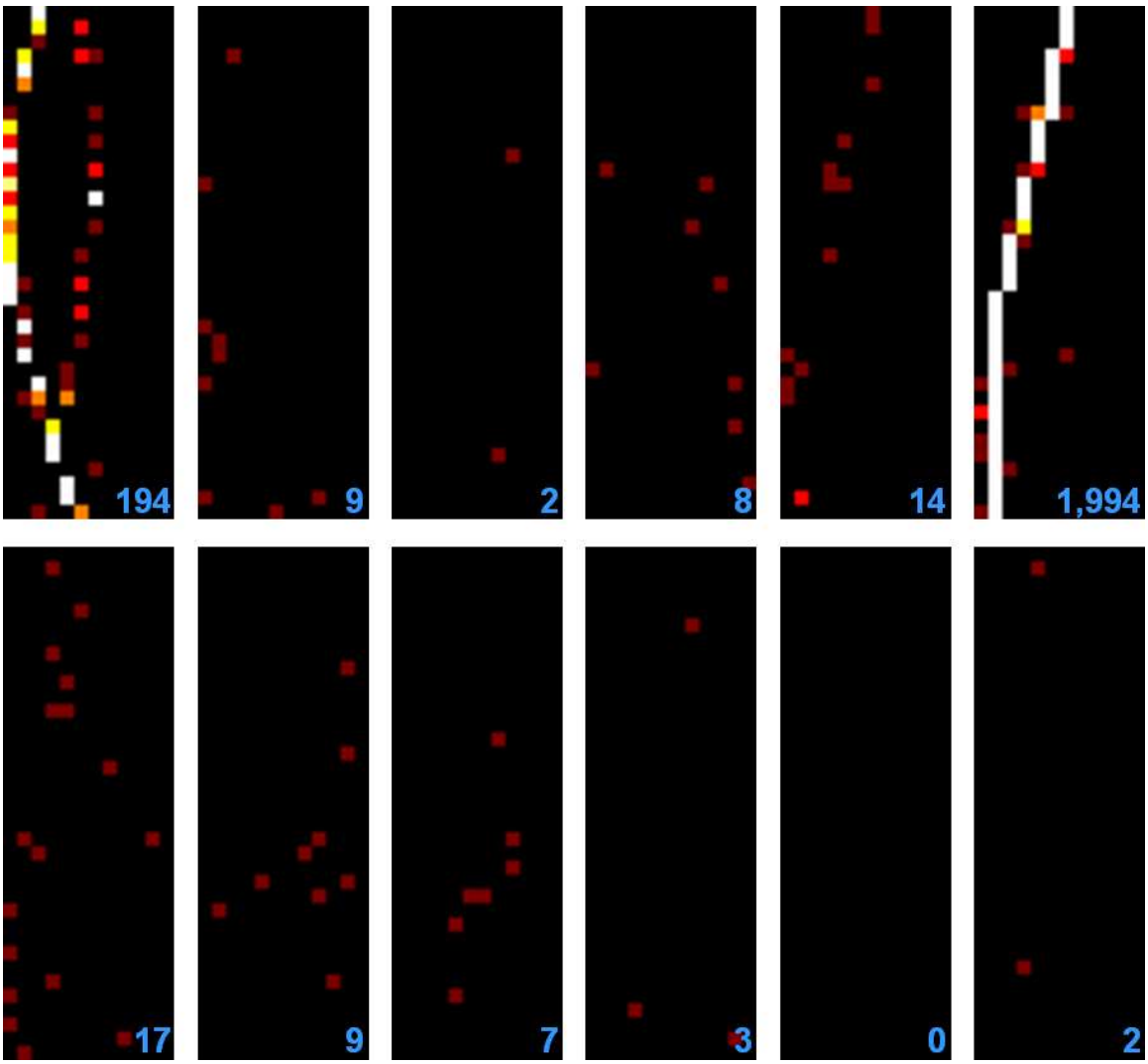

Figure 6.12: Sinograms shown in figure 6.10 reproduced with a photopeak energy gate. Similar results are observed as those from the first experiment. One of the two sources located in slice one has extremely limited statistics, which will no doubt hinder the reconstruction algorithm's ability to images this source.

6.13 displays twenty-three sinograms which includes the twelve basic sinograms from parallel LOR and the additional eleven from the nearest neighbour extension in the axial direction. One interesting feature to note is the appearance of the most active source in three separate sinograms which includes two of the additional nearly parallel sinograms. This may initially appear incorrect, but it is demonstrated in the left diagram of figure 6.14 that many locations exist which are potentially measured in three sinograms when the average of two nearly parallel LORs are utilised. If only one LOR is used rather than the average of two then it would only be possible for a source to appear in two sinograms, a situation depicted in the right hand image of figure 6.14. It should be noted that the depth of interaction plays an important role, a complication not included in the above discussion. Depth of interaction effects cause parallax problems for measured LORs in most scanners. SmartPET however, with the use of PSA can provide depth information to similar precision as the two orthogonal axes. This will be of great benefit when the number of LORs used in imaging is extended as part of the future development of the SmartPET system.

PSA improved spatial resolution

The use of PSA to improve spatial resolution results in the sinograms is shown in figure 6.15, where now just the two sinograms containing a source are considered. PSA has again been used to divide the strips into 3 or 5 sub-stripes corresponding to 1.67mm and 1.0mm position resolution respectively.

A problem arises in the PSA method when dealing with the edge strips. When only one adjacent strip and hence image charge exists the asymmetry method can not be applied. This can be seen as a blank area on the left and right hand side of PSA sinograms corresponding to interactions taking place in the detectors edge strips. If the source happens to be in the edge strip, as is the case in sinogram 1, then the sinogram will contain projections in which the source does not appear and will hinder the reconstruction algorithms. The problem can be overcome with different approaches to the positional calibration of pulse shape characteristics.

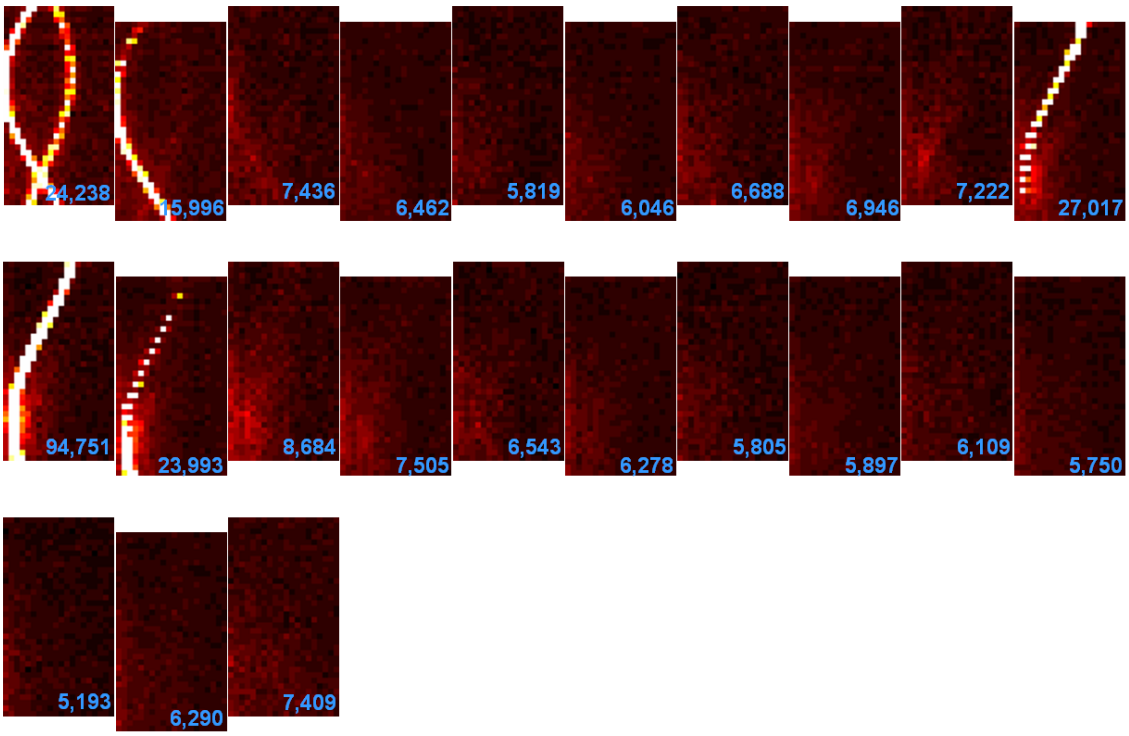

Figure 6.13: Sinograms reproduced with the additional data points from the almost parallel LORs included. Use of these LORs is extended along the rotation axis giving a total of twenty-three sinograms running from top to bottom, left to right. The slightly raised sinograms are the original twelve while the lowered are the additional sinograms gained from the almost parallel LOR technique.

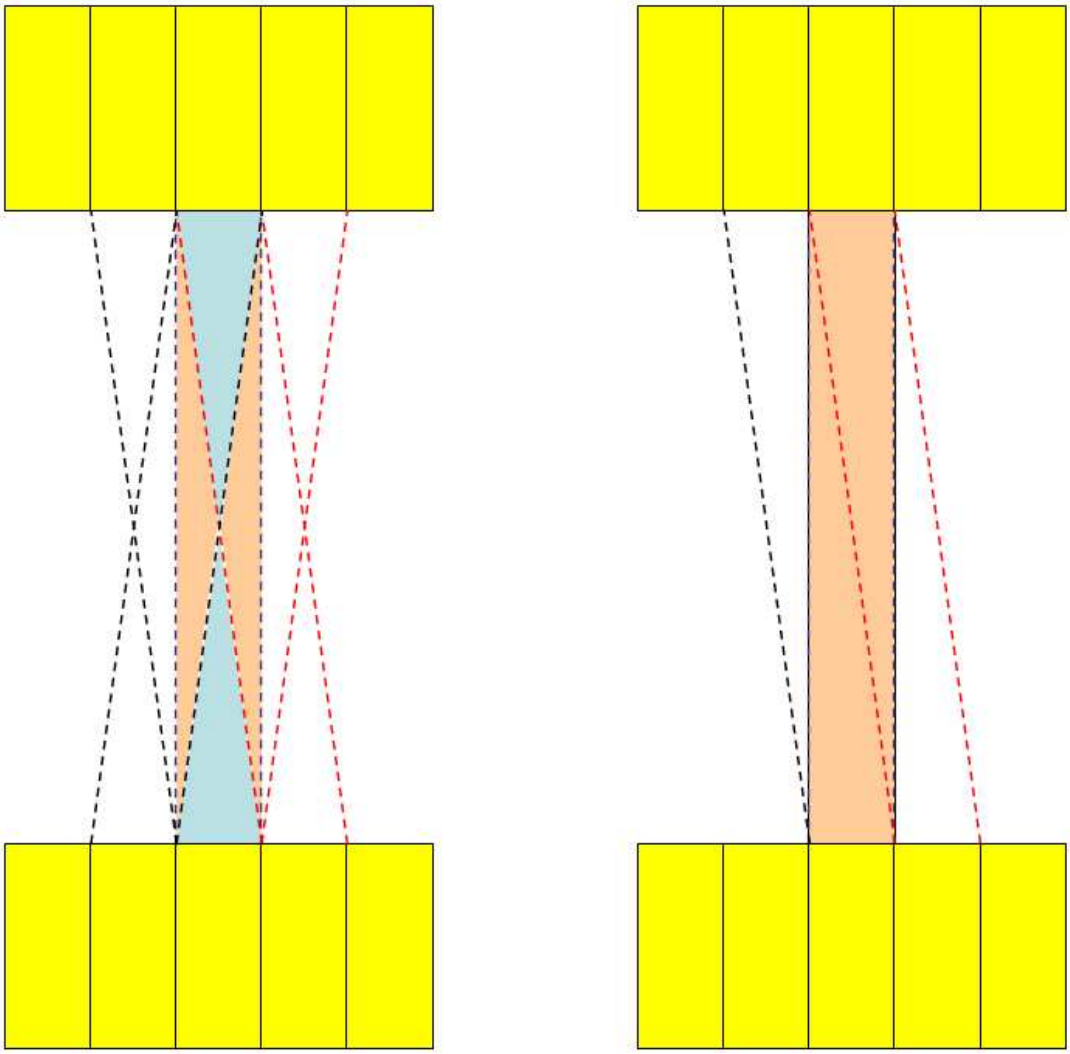

Figure 6.14: Diagrammatic explanation of the phenomenon of point sources appearing in two or even three sinogram slices when applying the almost parallel technique. In the left image, for a region covered by a single parallel LOR, positions covered by two sinogram slices are shown in salmon while pale blue regions are measured by three sinogram slices. The image on the right indicates the situation if only one direction of almost parallel LOR is used rather than an average of two.

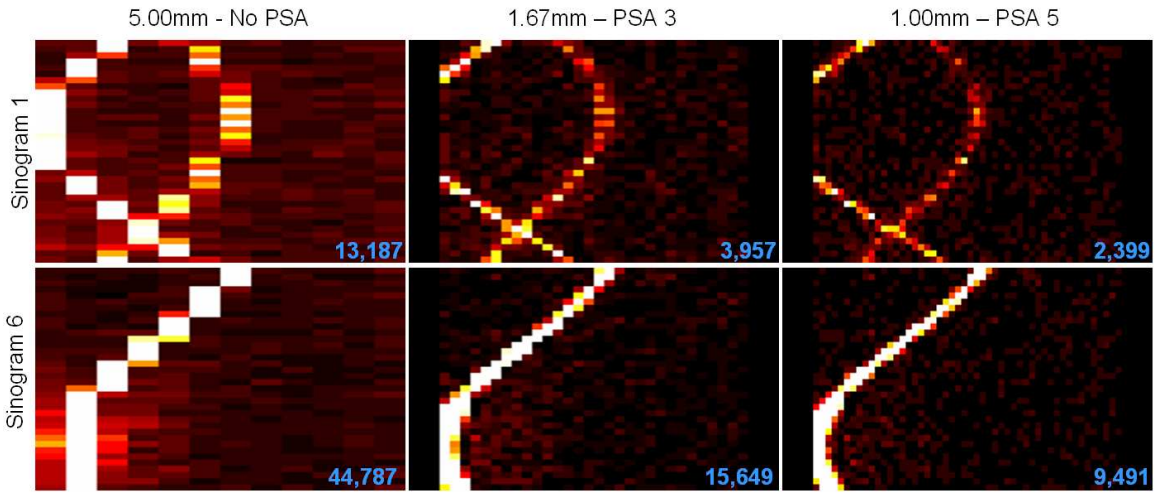

Figure 6.15: Sinograms from the two slices containing a source(s) in the second experiment. The sinogram with no PSA, 3 and 5 sub-strip PSA are displayed horizontally for both slices.

6.4 Reconstructed images

Reconstructed images from the sinograms for both experiments are presented in the following section. Images have been reconstructed onto a 256x256 pixel grid of physical dimension 60mm^2 which corresponds to the field of view of the SmartPET system. Due to variations in absolute values each image has been scaled independently and a consistent linear colour mapping has been applied to yield images with better visual contrast than either greyscale or negative greyscale provide.

The analytical FBP and iterative ML-EM algorithms used for the reconstructions are presented separately. FBP images unless stated, have been reconstructed with the application of a ramp filter and linear interpolation. ML-EM images are produced for 100 iterations of the algorithm as there is empirically no discernable improvement to the image quality beyond this level. Each reconstructed image includes the total number of events it was constructed from in the top right-hand corner.

6.4.1 FBP images

The first set of images presented are those from detector segmentation only, with no additional processing and no applied energy gate. Figure 6.17 displays the images of the three slices from experiment one containing a point source and the two slices from the second experiment.

The images clearly show the location of each point source within the field of view with a FWHM of the point spread function (PSF) ranging from 6 to 8mm. Comparing the results from the two experiments provides visual confirmation of the movement of the sources in the y and z axis noted from the raw sinogram data. The star like artifacts arising from the FBP algorithm when applied to limited angular measurements are evident in all the images. Differences in intensity between artifacts at certain angles arise as a result of the perceived variation in strength of the source at different projection angles due to the solid-angle considerations as depicted in figure 6.16. FBP provides no intrinsic method to account for such effects unlike statistical methods in which it can be incorporated in the system matrix.

Close inspection of the second image from experiment one reveals an area of limited artifacts to the source's top right-hand corner. This feature occurs because of rotation axis displacement noted in the sinogram analysis. The missing projection counts explain why the images of this source appears less spherical than the others.

Photopeak energy gate images

Applying the imaging algorithm to photopeak gated sinogram data yields the images presented in figure 6.18. Little improvement is observed in the images. The most obvious effect is the lower contrast of one source in the first image from experiment two, certainly due to the reduced statistics. Energy gated images would provide greater benefit in higher scatter experiments. The SmartPET system should therefore provide the gated and non-gated images side-by-side allowing the operator to decide on their relative merit for a given study.

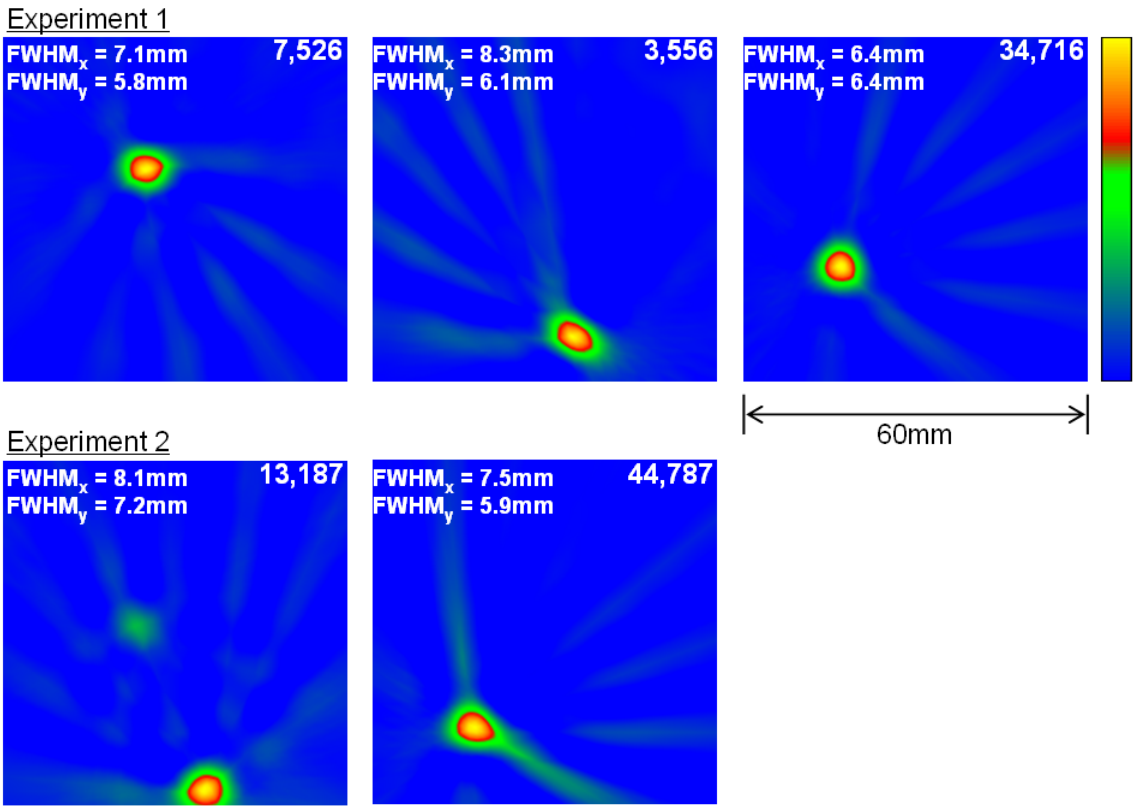

Figure 6.16: Images reconstructed from the sinograms containing activity shown in figure 6.5 and 6.10. Top: Images from sinogram 1,2 and 6 of experiment one. Bottom: Images of sinogram 1 and 6 from experiment two. Images have been reconstructed with a ramp filter and linear interpolation onto a 256x256 uniform pixel grid of size 60mm^2.

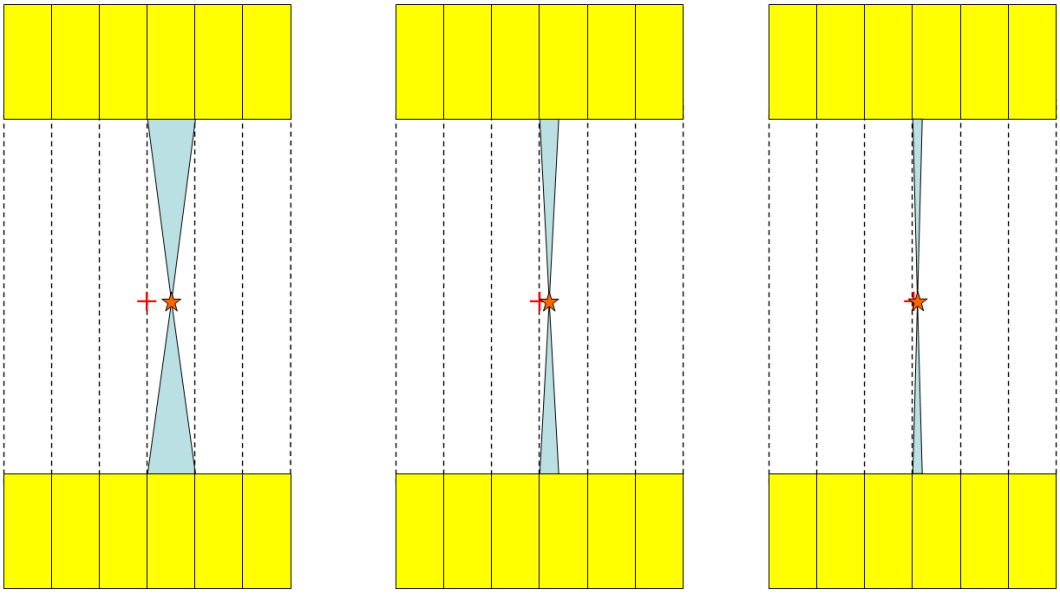

Figure 6.17: Three diagrams showing how the position of a source, shown here as a star icon, can greatly influence the solid angle made with two detector elements forming a parallel LOR. As the source approaches the boundary the solid angle in which an emitted pair of back-to-back photons can be detected by the LOR diminishes.

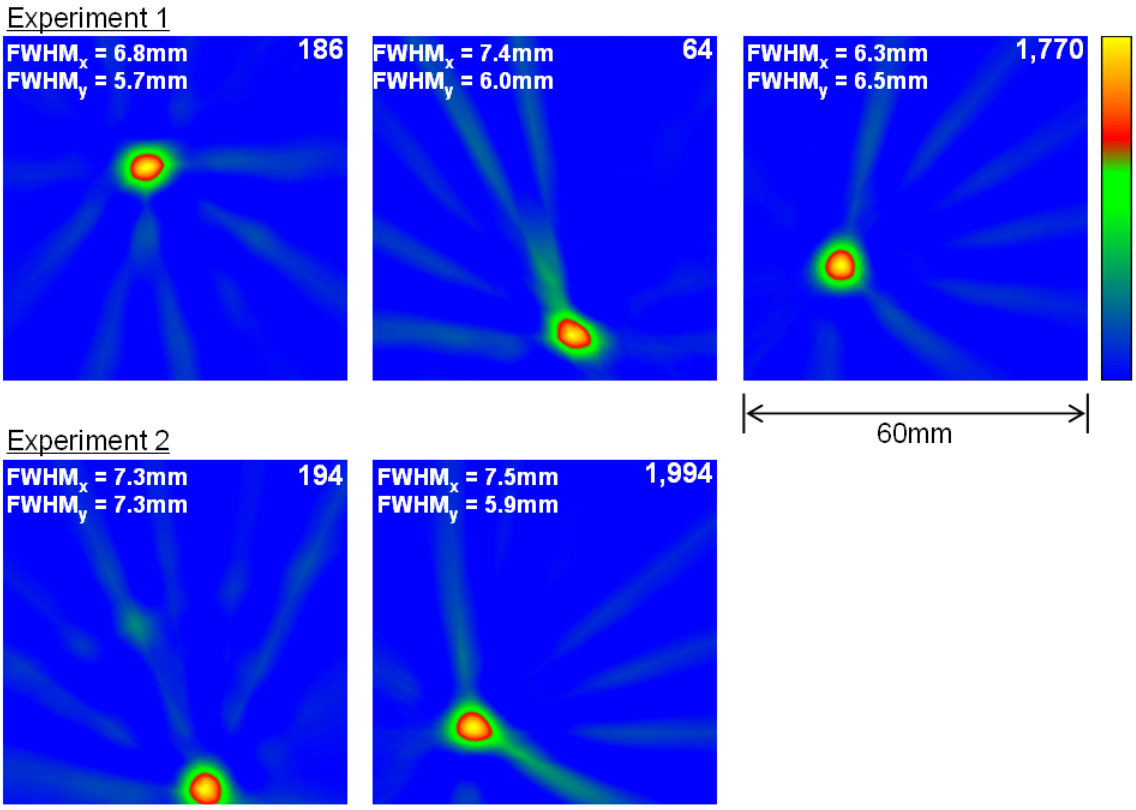

Figure 6.18: Images reconstructed from the photopeak gated sinograms containing activity shown in figure 6.6 and 6.12. Top: Images from sinogram 1,2 and 6 of experiment one. Bottom: Images of sinogram 1 and 6 from experiment two. Images have been reconstructed with a ramp filter and linear interpolation onto a 256x256 uniform pixel grid of size 60mm^2.

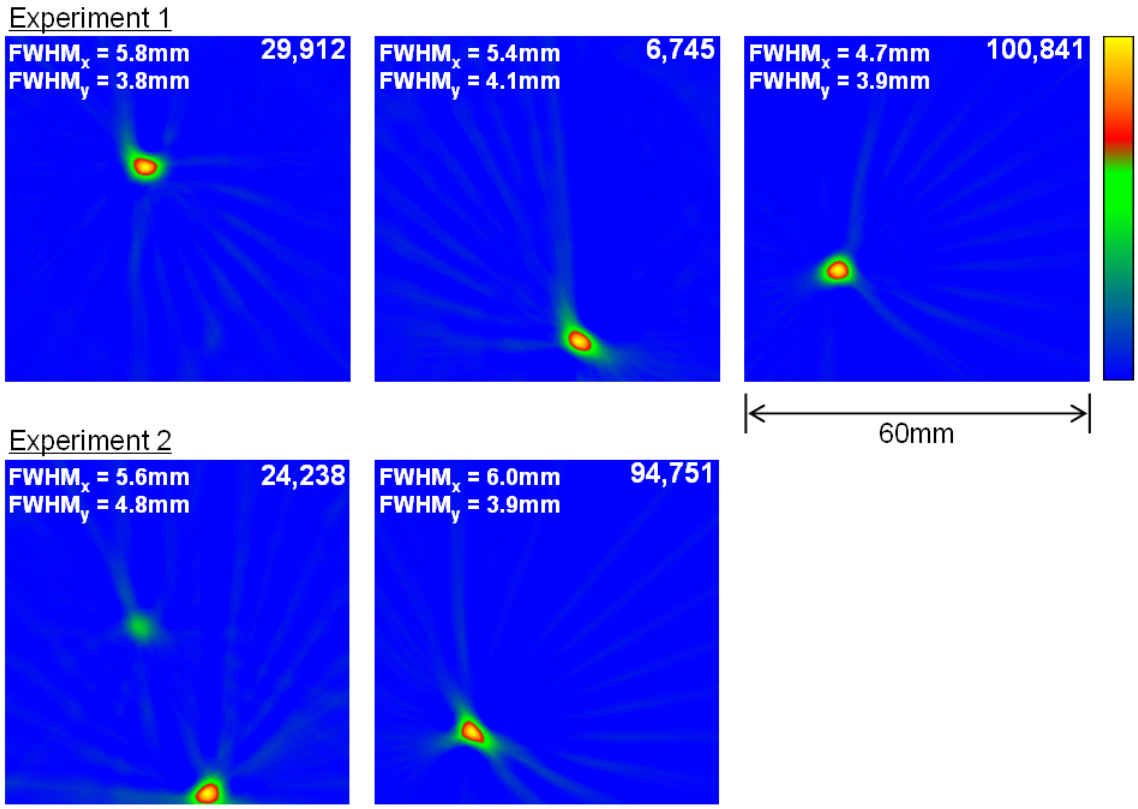

Figure 6.19: Images reconstructed from the sinograms which include the additional samples from the incorporation of almost parallel LOR in the data. Improvement of the FWHM is evident along with the increased level of events used in each image.

Additional almost parallel LOR images

Extending the sinogram sampling with almost parallel LORs results in the images shown in figure 6.19. The improvement in FWHM of each source is visually apparent and confirms this simple method provides a way to increase the LOR usage and improve the spatial resolution of the system. The sources appear to be less spherical in shape which is believed to be related to the error associated with the assumption that additional LORs are parallel, an error of 2.6^o for the detector configuration in this study. The source in image one from the second experiment is now more apparent than was seen in the images from basic sinogram data, due to the additional statistics.

PSA images

To compare the influence improved spatial resolution from PSA has on the quality of FBP reconstructed images a single sinogram of the most intense source (slice 6) is used. This source was selected because of the limited change seen in the slice between the two experiments and the fact the source is never present in the sinograms edge bins. The reconstructed images for both experiments can be viewed in figure 6.20. Three images are shown for both experiments, one is the image without the PSA improvement for reference and the other two are generated from 1.67mm and 1.0mm PSA sinograms presented in figure 6.9 and 6.15. The statistics for the PSA images are reduced because not all of the additional smaller LORs will be parallel, leading to a reduction in statistics in such sinograms.

Reconstructed images are dramatically improved through the use of the PSA spatial technique. FWHM are reduced to 2-5mm and provides further proof of the validity of the method and its exciting potential when applied to PET imaging with segmented germanium detectors. A large fraction of the rejected events do not scatter before detection but rather failed to deposit full energy in the detectors. The removal of these good imaging events together with the events which did scatter before detection is detrimental to the imaging process in this study due to the relative probability of each event type.

6.4.2 FBP filter analysis

Before concluding the FBP analysis it is worth considering the response of different filters when applied to one of the sinograms. Figure 6.21 shows images reconstructed from the experiment one slice six sinogram with no energy gate. The ramp filter is applied to all images previously shown because mathematically it is the ideal filter to deconvolve the 1/r blurring. It can be seen from figure A.2 that applying filters with progressively more severe high frequency suppression reduces background artifacts in the images. However this is at the cost of FWHM for a point source, a conclusion which is experimentally confirmed by the images in figure 6.21. It can therefore be

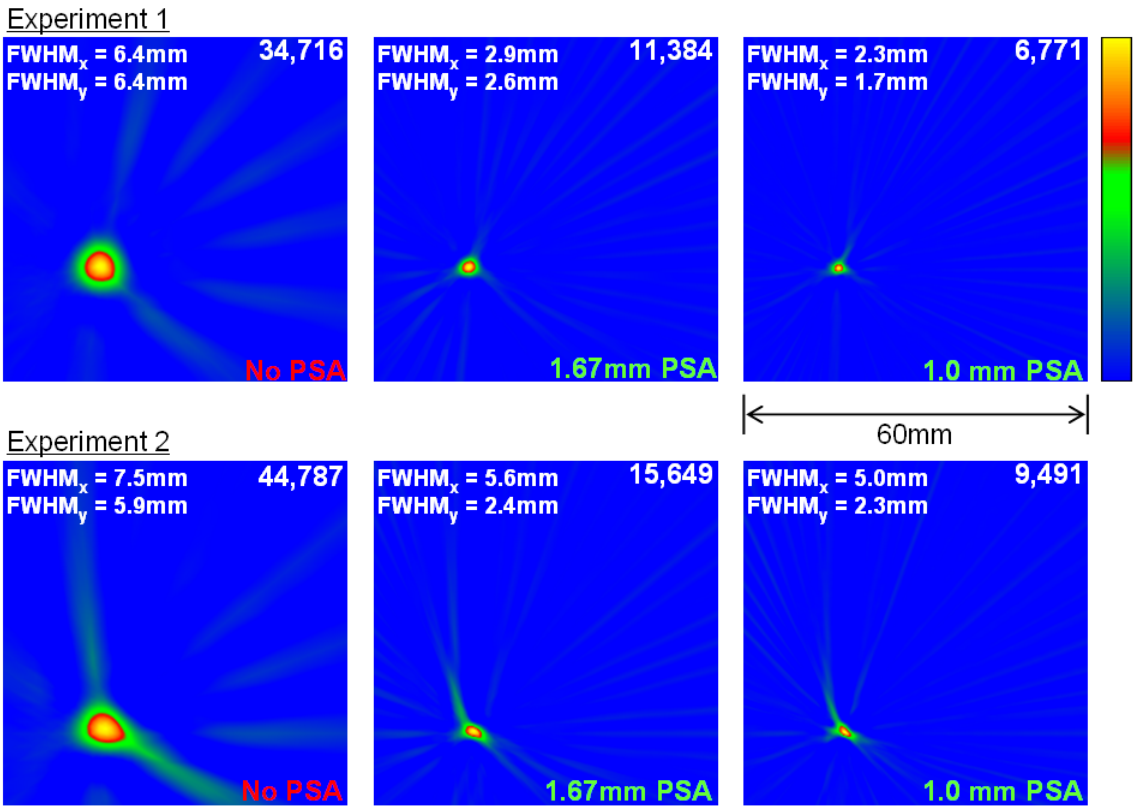

Figure 6.20: Reconstructed images from the slice six sinogram for both experiments. The images shown are (left to right) no PSA (5.0mm resolution) presented earlier, 1.67mm and 1.0mm position resolution using PSA.

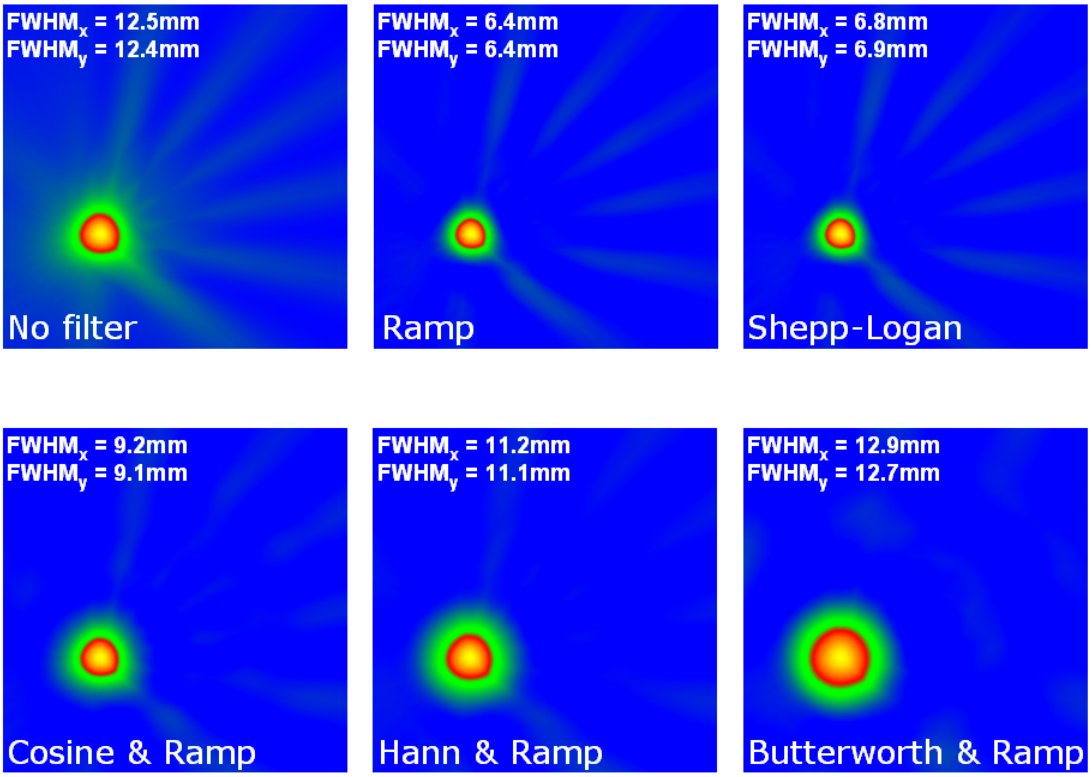

Figure 6.21: The application of different filters to a single sinogram displays the response to the varying degrees of high frequency suppression. Use of higher suppression filters reduces the level of background artifacts at the expenses of edge sharpness and hence FHWM of the source.

concluded for this sinogram enough statistics were collected to form FBP images using a ramp filter without need for additional high frequency suppression.

6.4.3 ML-EM images

The reconstructed image analysis undertaken with the analytic FBP algorithm is now repeated with the statistical ML-EM algorithm. Images are again reconstructed onto a 256x256 pixel grid representing a real area of 60mm^2. Empirically it was found one hundred iterations was enough to ensure suitable convergence and therefore all

images presented in the following discussion are the resultant images after completion of the hundredth iteration. The images from the basic sinogram data are presented in figure 6.22 and the photopeak gated in figure 6.23.

The ML-EM images are far superior to their analytic counterparts with virtually no background artifacts as expected from the earlier algorithm test results presented in section 4.5. ML-EM images display a much improved FWHM across all sources with an impressive value approaching 1mm at varying locations within the field of view. It will be very interesting to compare the performance of the system when a more complex geometry source is imaged in the next SmartPET experiments. Background removal and improved FWHM is further demonstrated by considering a one dimensional projection of the slice six images shown in figure 6.24.

The energy gated images behave in a similar manner to those observed with the FBP algorithm with little difference between the two sets. The limited number of statistics proves more problematic than the inclusion of incorrect LOR assigned events in the sinograms for these data sets. For the sources in experiment two slice one the limited counts did not allow the calculation of a meaningful FWHM for either source.

Additional almost parallel LOR images

When sinograms with additional LOR from nearest neighbours were reconstructed with ML-EM the resultant images (figure 6.25) did not show a single localised region of activity, as has been the case in all previous images. The main reason for the poor performance is believed to be due to the disparity between the system matrix probability calculations and the actual system. The additional LORs are being modelled as parallel, equally positioned between parallel LORs with no overlapping, constituting an incorrect modelling of the actual system. While a more accurate system matrix model of the additional data would improve the quality of reconstructed images it is a recommendation of this study that time would be better spent developing algorithms such as SSRB (Single-slice Rebinning Algorithm) or FORE (Fourier Rebinning Algorithm) [Def97] for use with SmartPET instead. FORE would allow many more

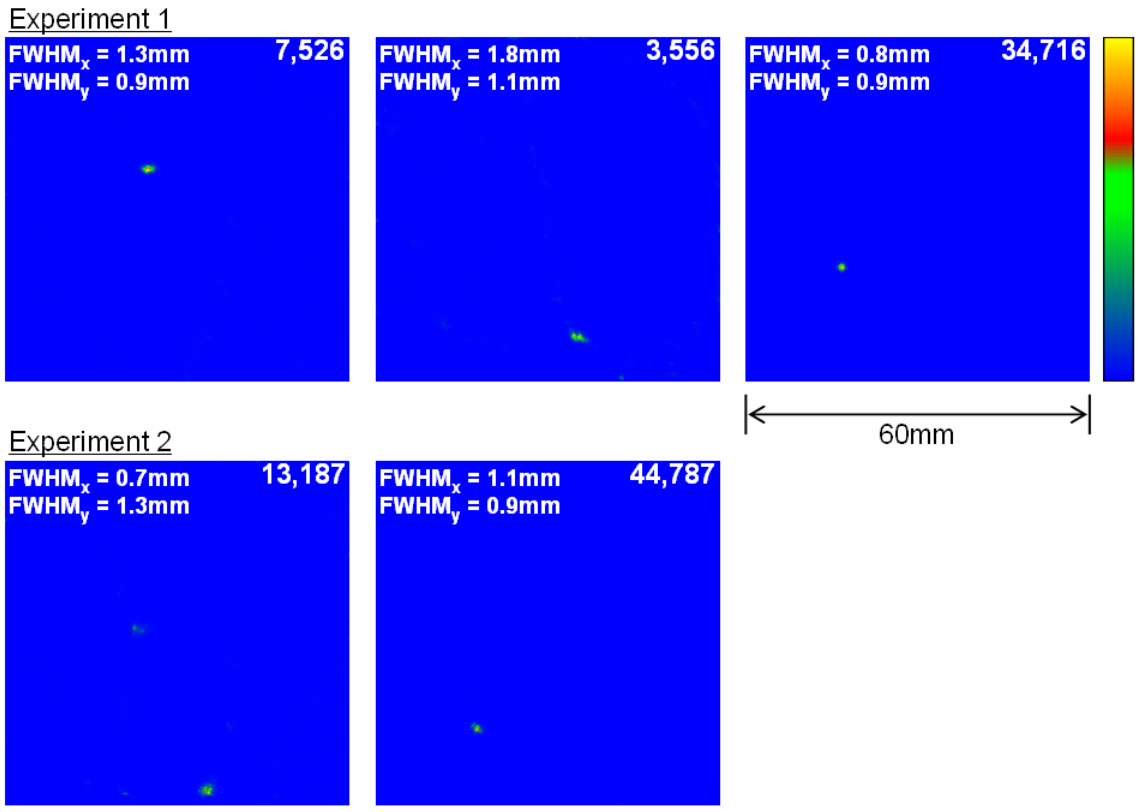

Figure 6.22: Reconstructed images of the three sources from both experiments using 100 iterations of the ML-EM algorithm. The sinograms are derived from the basic detector segmentation and no photopeak gate is applied.

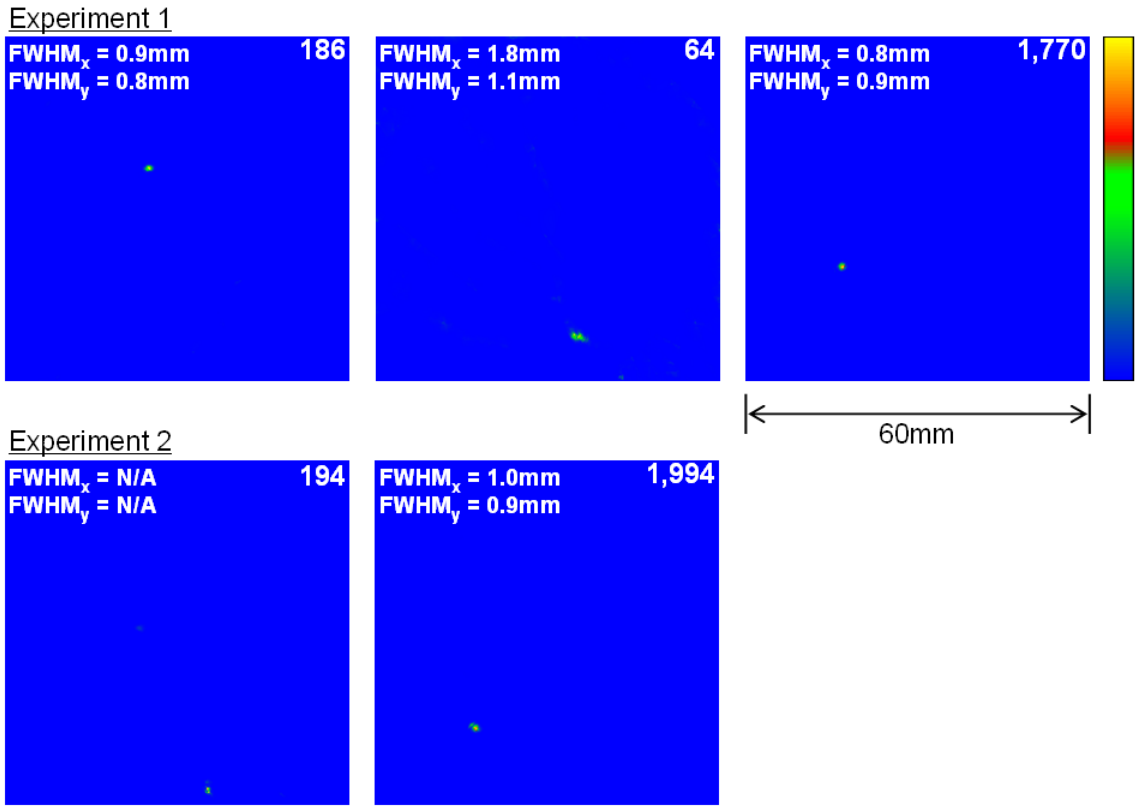

Figure 6.23: Reconstructed images of the three sources from both experiments using the ML-EM algorithm. The sinograms are derived from the basic detector segmentation and include a photopeak gate at 511 keV.

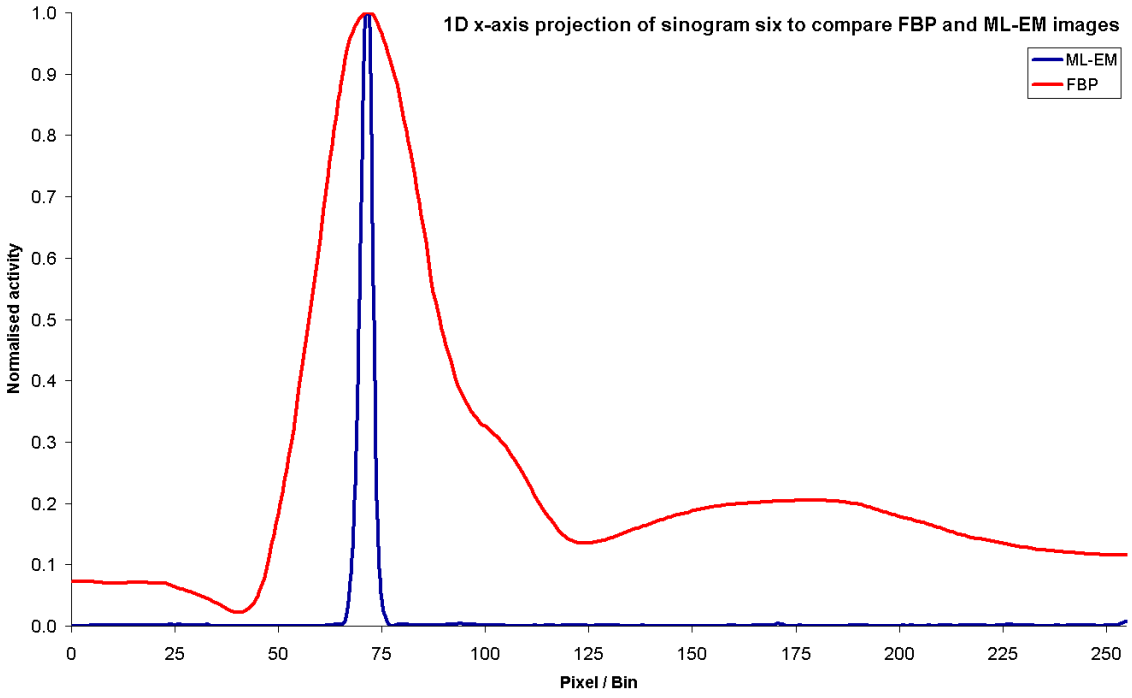

Figure 6.24: A 1D projection onto the x-axis of the normalised reconstructed images from slice six using FBP and ML-EM with no photopeak gate or PSA. The difference in width of the peak (PSF) and the level of background counts between the two is clearly apparent.

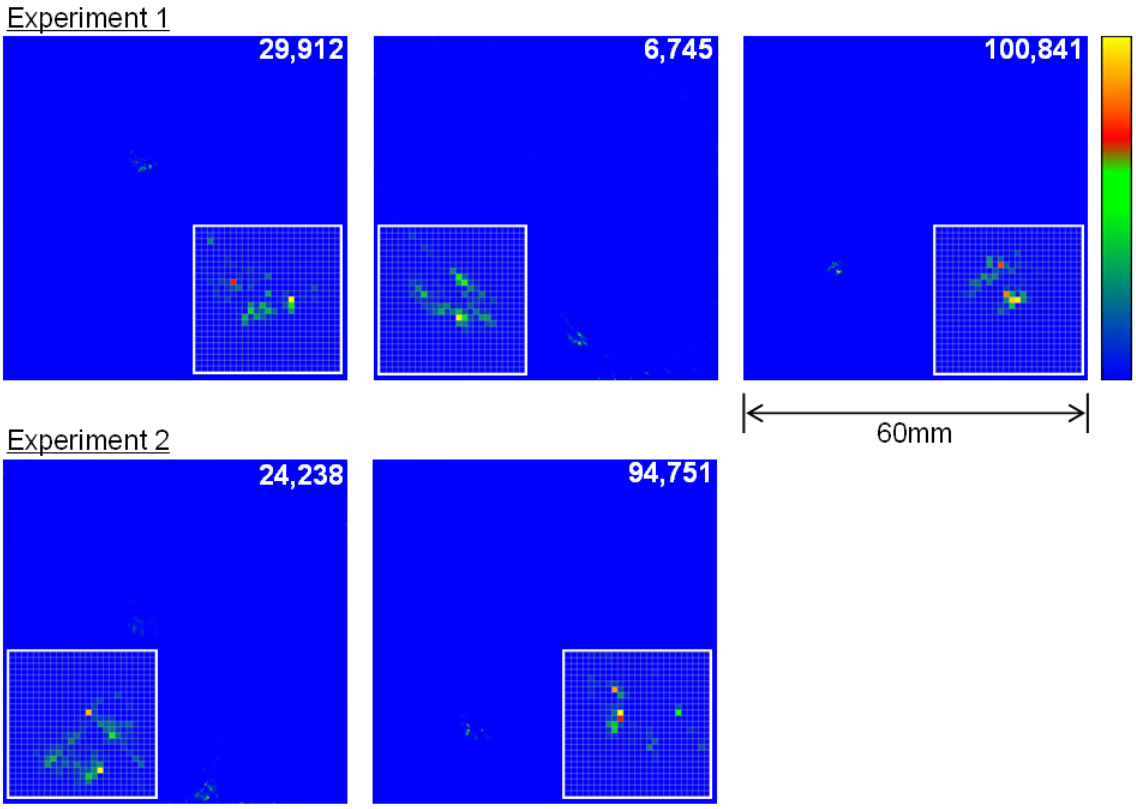

Figure 6.25: Reconstructed images when the ML-EM algorithm is applied to the sinogram data including almost parallel LOR. The poor match between the system matrix model and reality due to geometric considerations leads to sub-standard results.

oblique sinograms to be used in the imaging process and hence when combined with PSA makes almost parallel LOR imaging redundant.

PSA images

Reconstructing PSA sinograms with the ML-EM algorithm produced images which also did not show a characteristic PSF but rather a spluttering of pixels in the region of the source activity. The images for PSA data from slice six of experiment one are shown in figure 6.26 next to the image generated without the application of PSA. It is again predicted that the performance is being degraded due to factors relating

to the accuracy of the system matrix modelling. In the case of PSA the system model could be improved by incorporating the potential for incorrect binning with the results obtained from the collimated beam experiments initially presented earlier. Other factors which can potentially degrade the imaging performance should also be considered for future experimental work these include the accuracy of the centre of rotation correction and the positional stability of the entire system for the duration of the data collection process.

6.4.4 OS-EM / ML-EM comparative study

The OS-EM algorithm provides a means for increasing the convergence rate of iterative reconstruction techniques. The number of projections collected in this data set imposes a maximum number of subsets to six with each subset containing six equally space projections. The limitation in number of subsets arises due to the need for a minimum of four projections within each subset as discussed in section 4.4.4. The first six iterations for varying numbers of subsets are presented in figure 6.27.

As expected the convergence rate is proportional to the number of subsets, with one iteration of six subset OS-EM equivalent to six iterations of one subset or ML-EM. It is therefore possible to apply the OS-EM algorithm to SmartPET data sets in order to decrease the required image reconstruction processing time.

6.4.5 Computational performance of the imaging algorithms

The imaging section is concluded with a discussion concerning the computational performance of the different imaging algorithms. The algorithms developed as part of this study are optimised where possible within the bounds of the Java framework. The relatively limited number of elements (LORs) within sinograms means all FBP reconstruction are completed in under 400ms on a 32bit 2.0GHz CPU. A simulated sinogram of dimensions 256x256 reconstructed onto a 256x256 pixel grid requires 2000ms and a memory footprint of no more than 20Mb.

The ML-EM algorithm stores the complete system matrix in memory, to decrease

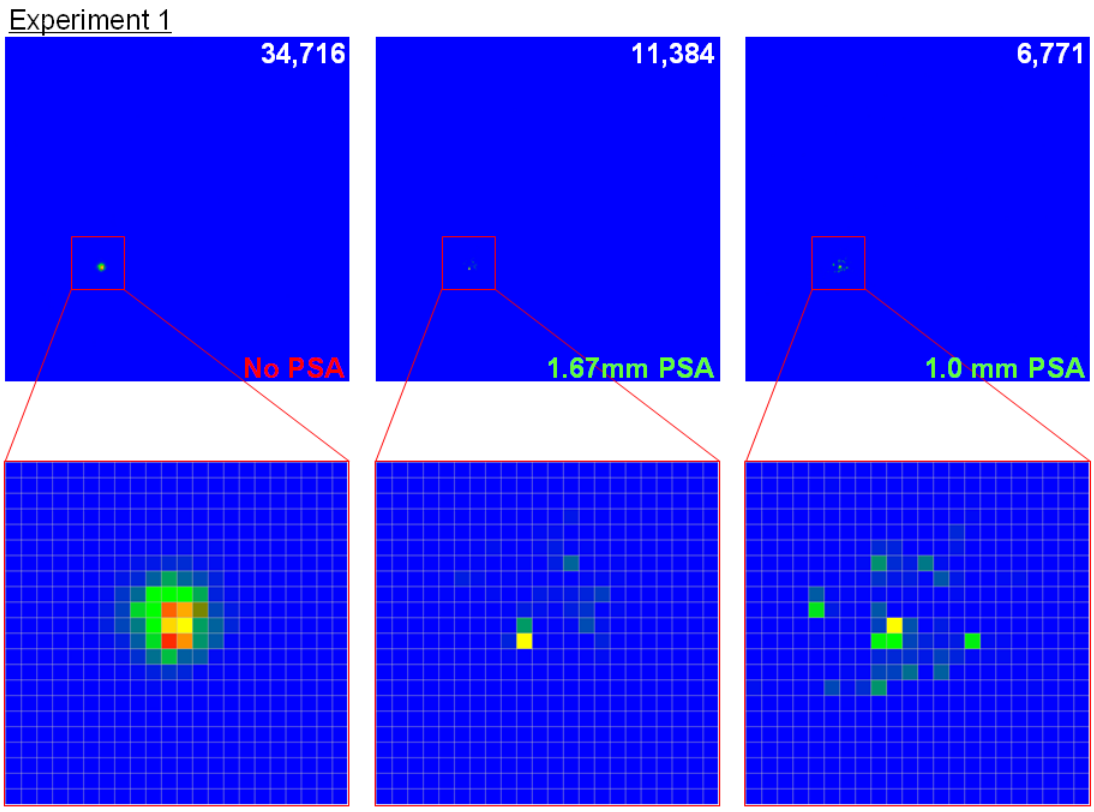

Figure 6.26: ML-EM reconstruction of slice six from experiment one with no PSA, 1.67mm and 1.0mm PSA spatial resolution. Problems arise again due to the system matrix not truly reflecting the reality of the measurements. Unlike the almost parallel LOR case this time it is the probability of the PSA method incorrectly labelling events which needs to be incorporated into the model rather than a geometry issue.

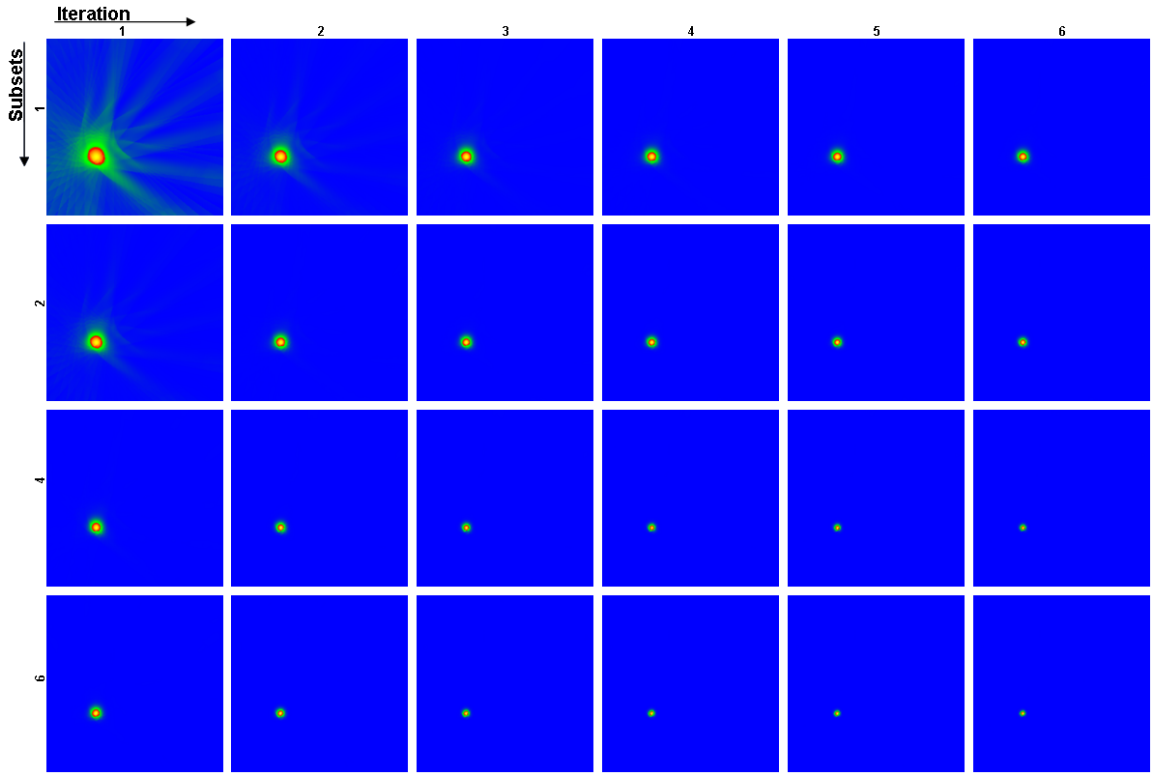

Figure 6.27: The first six iterations of the OS-EM algorithm (left to right) for 1, 2, 4 and 6 subsets (top to bottom). The same input sinogram data from slice six, experiment one is used in each case. As one iteration of the OS-EM code requires the equivalent processing time as one iteration of ML-EM it can be seen why use of subsets can decrease total reconstruction time by a factor equal to the number of subsets.

reconstruction time at the expense of memory usage. The sinograms presented in this work require ∼500ms of processing per iteration on the same 2.0GHz CPU but require in the region of 128Mb of memory for the PSA extended data set. A processing time of around ∼4000ms per iteration was achievable for a 256x256 simulated sinogram on a slightly faster CPU, but required a massive 1.5Gb of system memory to store the speed optimised system matrix.

Chapter 7

Conclusion

The experimental measurements undertaken as part of this study provide conclusive evidence of the feasibility of planar germanium detectors for use within positron emission imaging systems. It has been shown simple pulse shape analysis techniques can by employed to improve spatial resolution and hence imaging performance.

7.1 Sensitivity

The SmartPET coincidence system is triggered by one in every hundred positron emissions. Around one in every thousand of these detected events was utilised by the image reconstruction algorithms. Of these remaining events 2-3 in every hundred deposits full photopeak energy in both SmartPET detectors.

7.2 Imaging performance

The first images from the SmartPET system have been presented using both the conventional filtered backprojection algorithm and statistical maximum likelihood based algorithms, ML-EM and OS-EM. SmartPET detectors are shown to be capable of imaging point sources located at varying positions within the field of view with FWHM of ~6mm (FBP) and approaching 1mm (ML-EM) from the detector

segmentation alone.

7.2.1 Pulse Shape Analysis

The use of pulse shape analysis applied to the image charge pulses has been investigated for improving the achievable spatial resolution within a segmented planar detector system. Both the validation experiment and imaging results have demonstrated the success of the image charge analysis technique for PET imaging. It has been shown to provide reliable spatial resolution determination to 1mm within the SmartPET detectors. Results from this technique display promise in terms of both the generated sinograms and FBP reconstructed images. Further development is needed to exploit the spatial improvement when applying the iterative algorithms as the current system matrix is not an ideal model of the PSA extended process. The technique itself, although not as sophisticated as the suggested methods to felicitate gamma-ray tracking in the AGATA and GRETINA nuclear physics detector arrays, [AGA05] is adequate for emission imaging. These arrays propose to use adaptive grid search (AGS) based algorithms sorting through a simulated database of pulse shapes, looking for the most likely candidates and hence interaction positions [Baz04].

7.2.2 Photopeak gating

The excellent energy resolution provided by the germanium detectors can be seen to provide superb scatter event filtering when considering the resultant sinogram plots. However little improvement is observed when the energy gated data is processed by the reconstruction algorithms. Partly this is due to the fact energy gating can not discriminate between an event scattering before the detectors, which degrades image performance, and one which only interacts within the detector but does not deposit all of its energy. The second type of event for PET imaging forms a valid LOR and their removal is not conducive to improving image quality. For the two experiments performed the ratio of these two types of event is clearly dominated by the former, limiting the impact of scatter event removal by use of photopeak energy

gating. Indeed statistical limitations were reached for the weaker source after the application of photopeak gating. Energy gated images may provide more benefit for extended source measurements and of course become much more effective as the percentage of scattering events increases, provided statistics do not become a limiting factor. If events only scattering within the detector but not depositing full energy were confirmed as such, by use of larger or additional detectors then a germanium based system could provide the best solution for scatter rejection PET imaging.

Positron emission imaging algorithm development continues to be a very active research topic around the world. Particular interest is shown with regard to the modelling of a more sophisticated system matrix which attempts to incorporate scatter and random event correction. The implementation of the algorithms currently applied to the SmartPET system leaves ample room for further improvement to be comparable with those in operation on more mature scanners. Further development of the imaging algorithms will be an important requirement to allow SmartPET to compete on an equal footing with these scanners, especially when more complex distributed source arrangements are to be imaged.

7.3 Future developments

The experimental results demonstrated in this study represent the first stage in the development of the SmartPET planar germanium imaging project. As such not all aspects of the final system were in place at the time of the experiments. This had varying effects on the resultant images including reduction in the potential number of event and stability issues regarding the source locations during a scan. Furthermore, collection of the two data sets and subsequent analysis has provided a number of areas in which future experiments and research can be updated to enhance the systems performance. In concluding this study an overview of the improvements which should be explored in future work is presented.

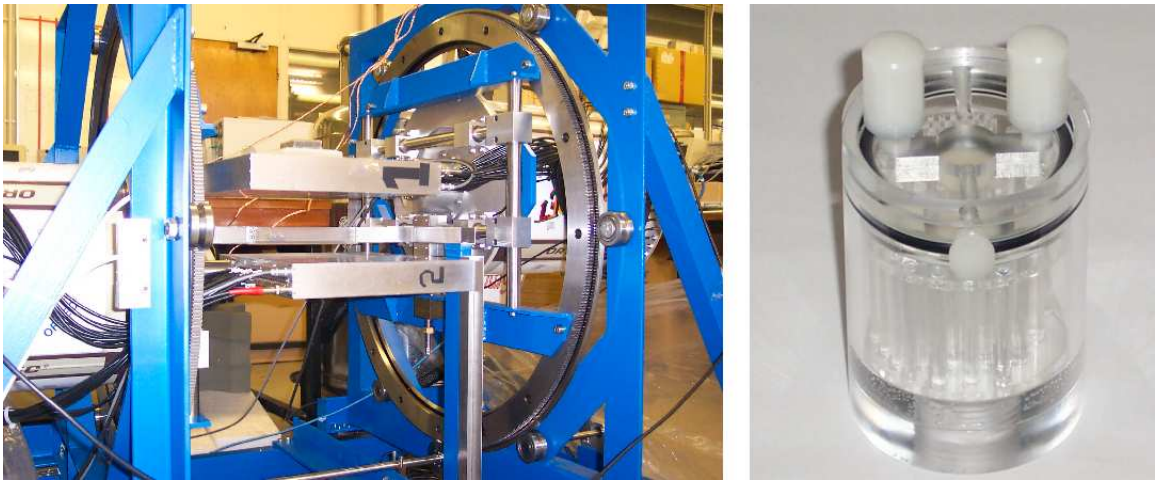

Figure 7.1: Left: SmartPET detectors housed within the supporting frame structure designed for the project. Right: Jaszczak cold rod micro deluxe phantom.

7.3.1 Supporting frame

Once the supporting frame [Figure 7.1] and motors are operational the systems physical stability will be greatly enhanced especially if long experiments are required. The automated system removes the requirement for human intervention during an imaging scan. This allows more projections to be measured, minimises the error associated with the known angle and diminishes the likelihood of accidental source disturbance. The amount of non imaging support material within the FOV will potentially decrease although some structure will still be needed to suspend the source between the detector.

7.3.2 Acquisition electronics

The GRT4 cards in conjunction with the available FPGA implemented algorithms gave rise to several limiting factors in this study. An overview of the new electronics commissioned, which are based on a two-tier compact PCI commercial solution provided by Lyrtech is given in [Bos05]. The level one cards will provide processing for each detector face's signals with algorithms for digitising, time stamping, energy

calculation and zero suppression programmed into the cards FPGA. The level two cards receive the output from all channels of each detector and hence will provide the event building and PSA analysis within their FPGA and DSP components.

The most notable limitation of the GRT based solution was due to the requirement of streaming all forty-eight pulses to the computer along a 4Mb/sec bandwidth limited architecture. The maximum count rate was limited to just 100-120 counts per second as a direct result. The development of processing algorithms such as zero suppression onto the cards themselves will reduce the required data transfer size per event, hence allowing more events to be processed per second. Coupled with an increased bandwidth limit, much higher count rates and hence potentially shorter scan times for the same level of statistics are required. Ultimately the aim is for all PSA algorithms to be performed on the cards. Output will then consist of just the interaction position and time stamping parameters allowing the system to run up to count rates limited only by the detectors.

A two-tier approach will mean changes to the systems triggering, where now the detectors can be effectively run in singles mode, i.e. data is recorded when either detector measures an energy deposit. Time stamping of events allows later processing to rebuild coincidence events based on a user controllable coincidence window. The system is then capable of using techniques such as delayed coincidence gating to provide estimates of the random event count rate.

7.3.3 Extended source imaging

To fully investigate the imaging ability of the SmartPET system a more complex source distribution is required. Ultimately this will involve the imaging of a small rodent but initially the next stage of development will see the imaging of both hot and cold rod phantoms. Three flanged Jaszczak micro deluxe phantoms [Figure 7.1] have been purchased for this purpose and will provide an excellent challenge for the SmartPET system, allowing imaging performance characteristics comparisons to be made with other small animal scanners.

7.3.4 Imaging algorithms

The algorithms developed and deployed as part of this study are adequate for the production of first generation images of point sources. There remains a huge scope for expansion in this area from increasing the number of LORs/events used in imaging to improvements already suggested for the enhancement of system matrix models. Investigations into the feasibility and implementation of fully three dimensional imaging is also a conceivable next step.

As more LORs are used in the imaging, depth of interaction will play a key role. SmartPET has the ability to measure depth of interaction to within 1mm by consideration of the real charge leading edge characteristics [Tur06]. The increase in potential pixels and hence LORs from use of depth of interaction will certainly require iterative algorithms based on list-mode data reconstruction.

Other considerations include the use of random event estimations which will be obtainable with the new electronics and potentially detector efficiency corrections from utilisation of collimated scan data experiments.

7.3.5 Analysis algorithms

Imaging with SmartPET will always be reliant on the ability of interaction position determination from analysis of pulse shapes. Therefore further improvements to the technique should be explored. In the short-term a solution to the single image charge strip issue needs to be finalised and tested with PET data sets. The long term goal would be to move to a full gamma-ray tracking algorithm which includes the ability to distinguish multiple interaction within a single pixel.

A study into the use of projected position determination success rates from either collimated beam experiments or Monte Carlo simulations within the system matrix of iterative algorithms should be considered. Potentially this approach may negate the need to correctly identify all events and facilitate the use of simpler, faster PSA methods.

Appendix A

Filtered Backprojection GUI

A.1 Introduction

The following document aims to provides a beginners user guide to the filtered back-projection graphical user interface (FBP GUI) developed using the Java programming language from Sun Microsystems [WebSun]. The FBP GUI application provides a simple graphical interface for loading single or multiple slice sinogram input files, executing the FBP algorithm with a choice of related options and then outputting the resultant reconstructed images to a number of different file formats.

FBP GUI is a cross-platform application, any operating system providing an implementation of the Java Runtime Environment should be able to run this software.

A.2 Installation and setup

A.2.1 Java installation requirements

To run the FBP GUI program, firstly a Java Runtime Environment (JRE) or Java Software Development Kit Standard Edition (J2SE SDK) version 1.4.x or later must be installed on the local computer or network. The JRE is sufficient to simply run the software while the J2SE SDK is required to recompile the software from the base

source code. JRE and SDK packages and installation instructions for most popular operating systems can be downloaded freely from the Java homepage [WebSun] if it has not been installed as standard.

An additional add-on package, Java Advanced Imaging API (JAI) may also be required if problems are experienced in saving output to imaging formats such as png. In most cases this package will be included with the basic Java installation and no further action is needed. Full JAI download and installation instructions can be found at: http://java.sun.com/products/java-media/jai/

A.2.2 Running FBP GUI

To start the FBP GUI program simply type the command `java runFBP_GUI` at a command prompt or xterm window from the directory containing the `runFBP_GUI.class` file. Alternatively type `java -jar runFBP_GUI.jar` from the directory containing the `runFBP_GUI.jar` file[1]. Some operating systems may also execute the program by simply double clicking the jar file icon.

A.3 General program layout

Figure A.1 shows the general user-interface, the exact appearance may vary slightly from that shown depending on the computer display settings and operating system. The interface is separated into four distinct sections:

1. **Load Sinogram Data:** The input data selection panel.
2. **Run FBP Algorithm:** The FBP algorithm settings and execution panel.
3. **Output Options:** Output data selection panel.
4. **Reconstructed Image:** Display panel for the reconstructed image(s).

[1] A jar file is simply a single file containing a collection of files packaged together and compressed to simplify transferring java programs, especially over the Internet.

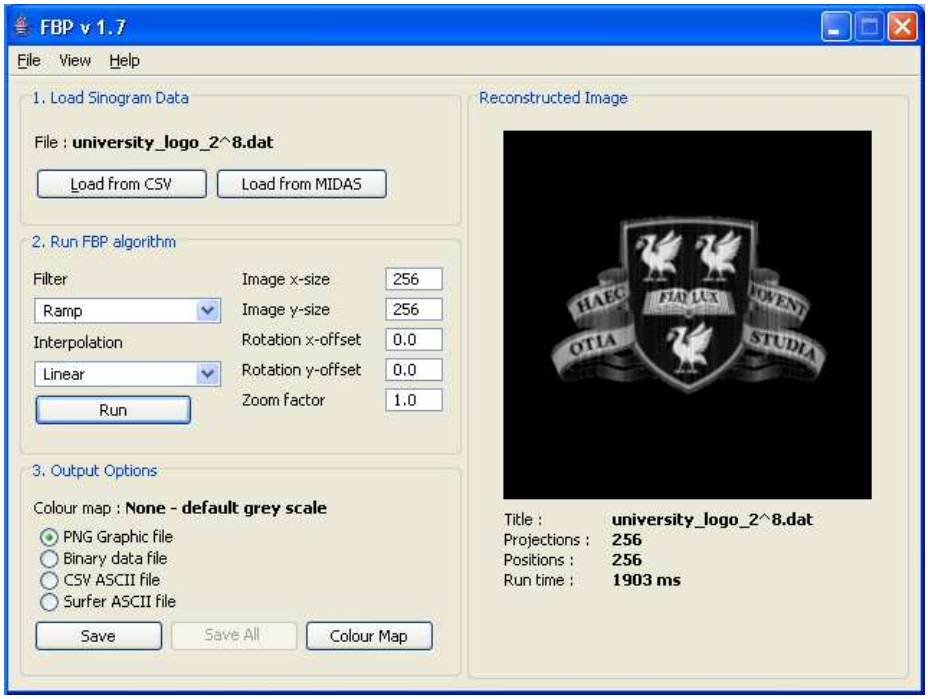

Figure A.1: Screenshot of the FBP GUI applications user-interface

The following sections will explain in more detail the purpose and functionality of each of these panels.

A.4 Loading sinogram data

The input data, the sinogram can be loaded into the application as either an ASCII file or a 2D spectra binary file generated in Eurogram format by the Multi Instance Data Acquisition System [MIDAS] software program.

Projections are expected to be equally spaced and span the region $0^o \leq \theta < 180^o$, the first projection is assigned as the 0^o angle. The positions within each projection should also be equally spaced. It is recommended that the number of these be equal to 2^n where n is an integer value, due to the Fast Fourier Transform (FFT) used by the reconstruction algorithm. The FBP algorithm will automatically zero-pad each projection up to the nearest 2^n value where required.

ASCII files should contain one projection per line and each element within a projection should be separated by either a tab, space or comma character.

MIDAS spectra are assumed to be the same size in both dimension as the sinogram itself i.e. they should not have blank elements. The sinogram should be orientated with the x-axis containing the positions and the y-axis being the projections.

Multiple files can be selected but it should be noted that the FBP options mentioned in the next section are applied to all files. All selected files should therefore contain the same number of data elements. Multiple file selection is ideal for sets of sinograms forming slices along the axial direction of the image space i.e. 2.5D image reconstruction.

A.5 Selecting FBP options

The FBP options selected highly influence the final reconstructed image, this section will explain the role of the different options found in the middle panel of the FBP GUI application and how they relate to the reconstructed image.

A.5.1 Filter selection

Ths is possibly the most important option, the filter refers to the 1D filter applied to each projection in the frequency domain before the filtered sinogram is backprojected. Although an in-depth discussion is beyond the scope of this document mathematically the ramp filter is the ideal filter to deconvolve the 1/r blurring inherent from back projecting sinograms. Real data however will contain varying degrees of high frequency noise and a ramp filter will strongly amplify this noise. Hence filters with different levels of suppression for high frequency components can often provide optimal performance for real data. Figure A.2 graphically displays the frequency response of the different inbuilt filters up to the Nyquist frequency.

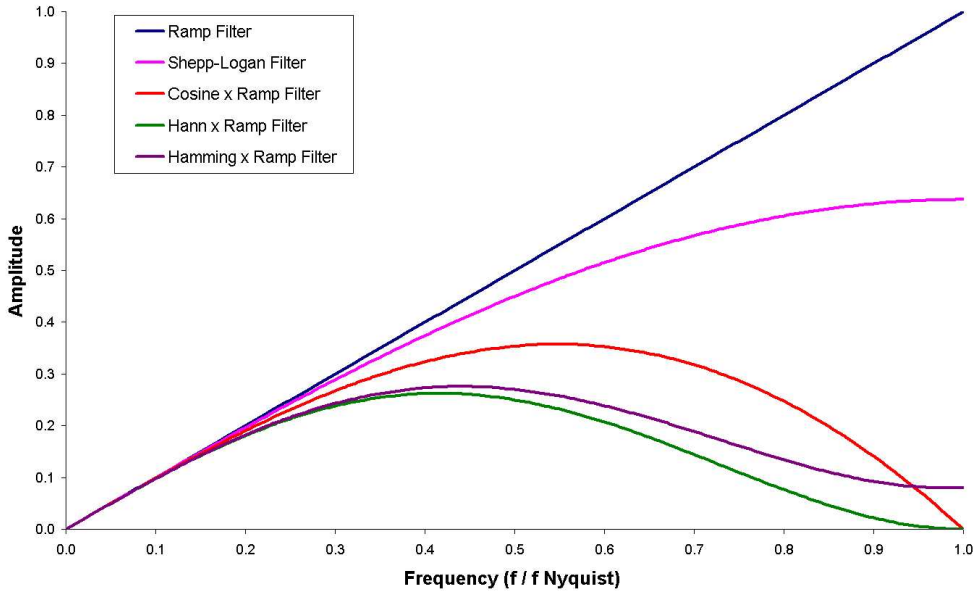

Figure A.2: Filter response as a function of frequency

A.5.2 Interpolation method

During the backprojection stage the sinogram data measured in a polar co-ordinate system is mapped to the Cartesian based pixel grid, requiring the use of a 1D interpolation method. Several interpolation methods are provided from simple nearest neighbour to the more complex cubic spline although in most cases linear interpolation is more than adequate.

A.5.3 Image size

The size of the reconstructed image in pixels. The x and y values can be set separately but it is recommended to use the same value for both and therefore produce square dimensioned images.

A.5.4 Rotation offset

The two rotation offset values are used for the centre-of-rotation (COR) correction of the system from the centre of the detector system in the x and y axis. The units for these values are scaled to the distance between detector bin elements in the projection and are independent of zoom value settings.

A.5.5 Zoom

The zoom value is self explanatory from the name but understanding of how the value relates to the image size is important to ensure correct interpretation of image scale. If the input data contains for example 64 equally spaced elements per projection and the size of the reconstructed image is 256 pixels then only the central quarter of the image will represent areas measured by the data. To ensure the data spans the entire image space then a zoom factor of 256 / 64 or 4.0 would be required.

A.6 Running the FBP algorithm

Once the input file(s) have been loaded and all relevant FBP settings selected the algorithm is run by simply clicking the button marked 'Run' in the central panel. The algorithm may take from under a second to several minutes depending on the number of lines of response, number of input files, FBP options selected and computer performance. During this time the application may seem unresponsive. Once complete the resultant images will be displayed in the image reconstruction panel on the right. If multiple input files exist then back and forward buttons will be displayed under the image area to move between the different images.

A.7 Output results

The output data panel contains controls for saving reconstructed images to file. Four different file formats are currently supported:

Tag	Replaced With
<index>	One based index value of each image
<index-1>	Zero based index value of each image
<title>	Name of the original input file from which the image was produced.

Table A.1: Available tags for use in multiple image output filenames.

1. **Graphic:** Output as a Portable Network Graphics (PNG) file.
2. **Binary:** Simple binary file format containing just the raw data values as double precision numbers.
3. **CSV ASCII:** Text file with values being separated by comma characters.
4. **Surfer ASCII:** Text file format readable by the analysis application Surfer

If multiple input files have been reconstructed then the second button titled 'Save All' will be enabled. Use of the 'Save' button with multiple images will result in the image currently displayed in the image reconstruction panel being saved to disk only. For multiple file output special tags can be used within the output filename path. Table A.1 lists the available tags and the content they are replaced by before output.

A.7.1 Colour Maps

By default reconstructed images are displayed using a linear greyscale normalised to the range of the data values. Other colour maps can be selected to provide different colour schemes when outputting to graphical format (and displaying within the image reconstruction panel). A number of different colour maps have been provided with the FBP GUI application. The user is encouraged to view these files in a text based editor to understand the simple format used and create new colour maps if they are required.

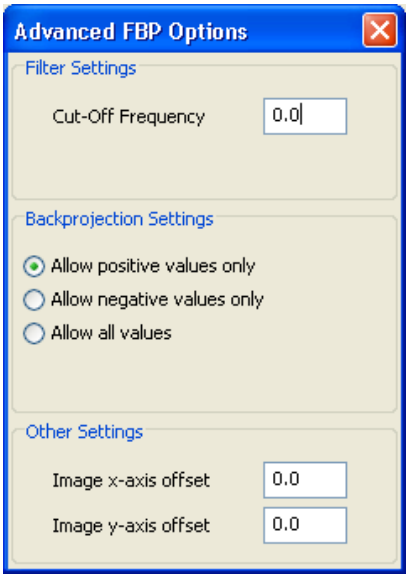

Figure A.3: Screenshot of the advanced options dialog

A.8 Additional features

A.8.1 Advanced options

The advanced options dialog can be activated from the file menu and is shown in figure A.3. The menu provides additional options relating to the FBP algorithm that are not displayed in the main application window.

Filter cutoff is used to limit the maximum frequency produced by the FFT, by default the value of zero is assigned as being the Nyquist frequency.

Backprojection settings provides control of the type of values allowed in the final image after the FBP. In PET data the option should be set to require positive only values while in transmission data sets the negative only option may be more appropriate. The application in general assumes higher values relate to higher concentrations while in transmission data higher values would represent lower concentrations along that line-of-response.

The x and y axis offset values simply act as a translation of the imaging area relative to the centre-of-rotation of the system.

A.8.2 Relative colour scaling

When multiple input files are selected by default the display colouring is scaled individually for each reconstructed image. The view menu contains an option which can toggle whether the set of images are scaled individually or relative to the whole set. This can be useful when comparing the relative intensity of different slices in a multiple slice data set.

Appendix B

Sinogram Generation Software

B.1 Introduction

During the development of the FBP algorithm (Appendix A) input sinogram data was required in order to test the algorithm was responding correctly. A set of secondary software programs were developed to generate simulated sinograms to provide test input. The following document outlines the basic functions of these programs and their usage.

The programs were again developed in the Java programming language and use a simple command-line driven interface. Two different methods were developed, the first generates a sinogram from an input text file containing a list of ellipse properties and relative intensity. The second calculates a sinogram from any greyscale image file (portable network graphic) with black pixels assumed to be zero intensity and white maximum intensity.

B.2 Ellipse based method

`GenerateSinogram1` and its accompanying command-line interface program `runGenerateSinogram1` can calculate the expected sinogram for a given input file of ellipses, which specify the source geometry and relative strength. To run the pro-

gram from an xterm or command prompt window in the directory containing the `runGenerateSinogram1_CommandLine.class` file enter the following command:

```
java runGenerateSinogram1_CommandLine [Arguments]
```

Where the arguments should be:
`inputPath outputDataPath No_of_Projections No_of_Positions Sigma_of_Noise [outputImagePath outputSourceDistribution]`

Input and output paths are required and are relative to the current location. The input path is the location of the ellipse list data file, the output is where the program output will be saved (ASCII CSV format). The number of projections and number of positions per projection are also required along with a value for the noise level applied to the image. If no noise is required use a sigma value of zero. Noise is generated using a Gaussian spread function. An image of the sinogram in png format is an optional output, if required add a path for this to the arguments list (outputImagePath). An estimated greyscale image of the source distribution obtained from the ellipse data file can also be optionally produced in the same way (outputSourceDistribution). Input ellipse data should be stored in an ASCII file with a single ellipse per line. Each line should list the required properties for the ellipse separated by a space character. The format of this file is as follows:

x-offset y-offset major_axis minor_axis rotation_angle(degrees) relative_strength
.
.

The output sinogram ranges from -1 to +1 in both axes so the ellipse data major and minor axis should not exceed these values. The Shepp-Logan phantom is provided as an example ellipse data file and users are suggested to study this for further clarification of the required structure.

B.2.1 Example usage

```
java runGenerateSinogram1_CommandLine mydata.dat result.dat 256 512 0.0
sinogram.png
```

B.3 Image based method

Sinogram generation from an image file works in much the same way as outlined in the ellipse method and users should refer to the information provided there. To run the program from an xterm or command prompt window in the directory containing the `runGenerateSinogram2_CommandLine.class` file enter the following command:

```
java runGenerateSinogram2_CommandLine [Arguments]
```

Where the arguments should be:
`inputPath outputDataPath No_of_Projections No_of_Positions Sigma_of_Noise [outputImagePath]`

The greyscale image is used as an intensity map, with white being the highest intensity and black being the lowest or zero. It is recommended to use a png file with a full 16 million colour palette even though only greyscale is allowed in the image. Input images must be a square, i.e. pixel width = height. Due to the implementation method `GenerateSinogram2` does not support more positions than the pixel-size of the input image, no limit exists on number of projections.

B.3.1 Example usage

```
java runGenerateSinogram2_CommandLine myimage.png result.dat 256 512 0.0
sinogram.png
```

References

[AGA05] Agata workshop PSA session, http://ns.ph.liv.ac.uk/AGATA/PSA.html, Liverpool, (2006)

[Bai03] D.L. Bailey *et al.*, Positron Emission Tomography Basic Science and Clinical Practice (Springer, 2003), **ch3**, 72.

[Bar04] H.H. Barrett and K.J. Myers, Foundations of Image Science (Wiley, 2004), **ch4**, 205.

[Baz04] D. Bazzacco and R. Venturelli, LNL Annual Report, (2004)

[Bos05] A.J. Boston, Oral contribution, SmartPET meeting, Melbourne, (2005).

[Che03] S.R. Cherry *et al.*, Phys. Med. Biol. **48**, (2003), 1519.

[Coo06] R.J. Cooper, Private communication (2006).

[Dea83] S.R. Deans, The Radon Transform and Some of Its Applications (Wiley, 1983).

[Dav65] C.M. Davisson, Interaction of γ-Radiation with Matter *Alpha-, Beta- and Gamma Ray Spectroscopy*, (1965), 37-78.

[Dav52] C.M. Davisson and R.D. Events, Gamma-Ray Absorbtion Coefficients Reviews Modern Physics, (1952), **Vol. 24**, 86.

[DeB50] S. DeBenedetti *et al.*, Physical Review vol.77, **2**, (1950), 205.

[Def97] M. Defrise *et al.*, IEEE Trans. Med. Imaging. **MI-16**, (1997), 145.

[Def03a] M. Defrise *et al.*, Positron Emission Tomography Basic Science and Clinical Practice (Springer, 2003), **ch4**.

[Def03b] M. Defrise *et al.*, Positron Emission Tomography Basic Science and Clinical Practice (Springer, 2003), **ch4**, 105.

[Des02] M. Descovich, Improving the position resolution of Highly Segemented HPGe Detectors using Pulse Shape Analysis Methods, Ph.D. thesis, University of Liverpool, (2002).

[Dir58] P.A.M. Dirac, The Principles of Quantum Mechanics 4th Edition (Oxford Press, 1958), **XI**, 273.

[Fan47] U. Fano, Phys. Rev. **72**, (1947), 26.

[Geo93] A. Georgiev and W. Gast, IEEE Trans. Nucl. Sci. **40**, (1993), 770.

[Hud94] H.M. Hudson and R.S. Larkin, IEEE Trans. Med. Imaging. **13**, (1994), 609.

[Jea99] A.P. Jeavons *et al.*, IEEE Trans. Nucl. Sci. **46**, (1999), 468.

[Kac01] K. Kacperski *et al.*, IEEE Trans. Med. Imaging **23**, (2004), 525.

[Kno00a] G.F. Knoll, Radiation Detection and Measurement 3rd Edition (Wiley 2000), **ch11**, 357.

[Kno00b] G.F. Knoll, Radiation Detection and Measurement 3rd Edition (Wiley 2000), **ch12**, 410.

[Kno00c] G.F. Knoll, Radiation Detection and Measurement 3rd Edition (Wiley 2000), **ch17**, 610.

[Lan84] K. Lange and R. Carson, J Comp. Ass. Tomo. **8**, (1984), 306.

[Laz03] I.H. Lazarus, IEEE Trans. Nucl. Sci. **51**, (2004), 1353.

[Lee90] I.Y. Lee, Nucl. Phys **A520**, (1990), 641c.

[Lee99] I.Y. Lee, Nucl. Phys **A422**, (1999), 5199.

[Leo93] W.R Leo, Techniques for Nuclear and Particle Physics Experiments (Springer-Verlag 1993), **ch2**, 37.

[MIDAS] Website, http://nnsa.dl.ac.uk/MIDAS/

[Mos03a] W.W. Moses, IEEE Trans. Nuc. Sci. **50-5**, (2003), 1325.

[Mos03b] W.W. Moses, Oral contribution IEEE Nuclear Science Symposium Conference, Portland Oregon, (2003)

[Oll97] J.M. Ollinger and J.A. Fessler, IEEE Singal Processing Magazine, (Jan 1997), 43.

[Ore49] A. Ore and J.L. Powell, Physical Review vol.75, **11**, (1949), 1696.

[Pan99] X. Pan, American Association of Physicists in Medicine, 41st Annual meeting, (1999)

[Rad17] J. Radon, Math. Phys. K1. **69**, (1917), 262.

[Ram39] Ramo, P.I.R.E. **27**, (1939), 584.

[Rad88a] V. Radeka, Ann. Rev. Nucl. Part. Sci, **38**, (1988), 217.

[Rad88b] V. Radeka, Ann. Rev. Nucl. Part. Sci, **38**, (1988), 224.

[Rea98] A.J. Reader *et al.*, Phys. Med. Biol. **43**, (1998), 835.

[She82] L.A. Shepp and Y. Vardi, IEEE Trans. Med. Imaging **MI-1**, (1982), 113.

[Sim97] J. Simpson *et al.*, Z. Phys **A358**, (1997), 139.

[Sta81] H. Stark *et al.*, IEEE. Trans. Acoust. **ASSP-29**, (1981), 237.

[WebSun] Website, http://java.sun.com/

[Sze02a] S.M. Sze, Semiconductor Devices Physics and Technology 2nd Edition (Wiley 2002), **ch4**, 93.

[Tai01] Y.C. Tai *et al.*, Phys. Med. Biol. **46**, (2001), 1845.

[Tar03] G. Tarantola *et al.*, Journal of Nuclear Medicine. **44**, (2003), 756.

[Tow03] D.W. Townsend and T. Beyer, Positron Emission Tomography Basic Science and Clinical Practice (Springer, 2003), **ch8**.

[Tur06] G.H.B. Turk, The characterisation of the first SmartPET HPGe planar detector, Ph.D. thesis, University of Liverpool, (2002).

[Yan06] Y. Yang and S.R. Cherry, IEEE Trans. Nucl. Sci. **53**, (2006), 127.